AN ABSTRACT OF THE DISSERTATION OF

Zhongwei Gao for the degree of Doctor of Philosophy in Chemical Engineering presented on December 19, 2019.

Title: Growth, Characterizations, and Applications of Patterned Nanostructured Thin Film

Abstract approved: ____
Chih-Hung Chang

A unique microreactor-assisted nanomaterial synthesis and printing process was studied for the fabrication of patterned metal oxide nanostructured thin films. The process uses a continuous flow microreactor to control and generate a reactive chemical flux that was transported to a patterned microfluidic channel. The microreactor-assisted nanomaterial synthesis process can generate reactive building blocks, ranging from ions, molecules, and clusters to nanoparticles with consistent composition and constant concentration. The reactive solution was then delivered to the substrate surface, guided by a patterned microchannel. The growth kinetics of the nanostructured ZnO on silicon wafers were studied by measuring the thickness of the film using the stylus profiler and scanning electron microscope under various growth conditions using the microreactor and the microchannel made of polydimethylsiloxane (PDMS). The process contains three zones: a mixing zone, a reactant generation zone, and a deposition zone. This process allows a separation of the homogeneous reaction in the solution and the heterogeneous reaction on the substrate surface, resulting in a well-controlled growth

of the ZnO nanostructures on the substrate surface so that the growth mechanisms and kinetics can be studied. Different growth parameters, including flow rate, residence time, the temperature of both the chemical solution and the substrate, are varied to study the growth kinetics.

The flow rate is one of the key parameters. A higher flow rate can result in faster growth of ZnO nanostructures, while a lower flow rate will result in a longer residence time of the chemical solution within zone 2 which can lead to the homogenous formation of solid nanoparticles and reduce the concentration of reactive $Zn(OH)_2$ (aq). This finding is further supported by growth experiments using reactors with different reaction channel lengths at zone 2. Besides, the thickness of rectangular patterned ZnO nanostructured films show a saddle-shaped profile, which is thinner near the center. This thickness profile is a result of combined heat and mass transfer of the reactive solution within the patterned channel, as qualitatively supported by COMSOL simulations. By measuring the growth rates as a function of substrate temperatures, the activation energy of the rate constant is obtained at 22.65 kJ/mol. This process not only provides better control to fabricate patterned metal oxide nanostructures but also offers the unique capability to study the growth mechanisms.

The improved understandings were applied to demonstrate a novel, scalable process to fabricate ZnO nanostructures with multiscale 3D geometric shapes. In particular, the precursors were firstly mixed and heated in a microreactor to control solution temperature and to generate reactive species. The reactive solution was then delivered to the substrate surface guided by a patterned PDMS channel with different designs, including spiral, parallel lines, and the split-and-recombine pattern. ZnO nanostructures with multiscale 3D geometric shapes were formed along the patterned channel. It is found that the geometry of ZnO nanostructure is controlled by the channel geometry, flow rate, and substrate temperature. The stylus profiler measures film thickness, and the result shows the unique characteristics of each pattern type. With the aid of the COMSOL Multiphysics finite element analysis, the parameters that control the growth are studied: in the spiral pattern, the consumption of the reactant can result in a thinner film as the solution flows through the channel. In the parallel-design pattern, the film thickness is determined by the flow rate of the solution in each channel in parallel. With the channel narrowed and the flow rate reduced, a thinner ZnO nanostructured film is obtained. In the split-and-recombine design pattern, the film growth rate is halved as the channel split and doubled back as the channels re-combined. The temperature profile within the channel is another critical parameter of controlling the growth of ZnO nanostructures in all dimensions. This scalable process, aided with new understandings, will provide a unique capability to fabricate metal oxide nanostructures of controlled multiscale 3D geometric shapes.

Besides ZnO, the microreactor-assisted nanomaterial synthesis and printing process was used to deposit patterned CuO and $Cu_2(OH)_3NO_3$ nanostructures on surface, including dense nanocrystalline CuO film, CuO nanorods, $Cu_2(OH)_3NO_3$ nanorods, and $Cu_2(OH)_3NO_3$ nanoplates using the same reactants, $Cu(NO_3)_2$ and hexamethylenetetramine (HMTA). The critical process parameter that controls the formation of different products is the concentration of the OH^- in the solution, which can be controlled by the ratio of the reactants and the temperature of the microreactor. The high concentration of OH^- leads to the formation of $Cu(OH)_2$, which is then converted to CuO on the heated substrate surface. In contrast, the low concentration of OH^- leads to the formation of $Cu_2(OH)_3NO_3$. These results show the applicability of the microreactor-assisted nanomaterial synthesis and printing process to deposit metal oxide nanostructures with controlled structure and composition.

The utility of microreactor-assisted nanomaterial synthesis and printing process was demonstrated via the fabrication of heterojunction ZnO/CuO bi-layer film. The bilayer film was built by depositing a patterned nanocrystalline CuO film on a gold-coated glass surface using the microreactor-assisted nanomaterial synthesis and printing process, followed by the deposition of ZnO nanostructured film with a smaller-size pattern using the same process. The heterojunction ZnO/CuO bi-layer film shows rectifying behavior; it allows currents to flow when forward biased and passes only low leakage currents with reverse bias; the p-n diode has a rectification ratio around 10^4, which is comparable to the values among the best solution-processed p-n junction diodes. The results of this study demonstrate the capability of our microreactor-assisted nanomaterial synthesis and printing process to fabricate structured thin films for functional devices.

Growth, Characterizations, and Applications of Patterned Nanostructured Thin Film

by
Zhongwei Gao

A DISSERTATION

submitted to

Oregon State University

in partial fulfillment of
the requirements for the
degree of

Doctor of Philosophy

Presented December 19, 2019
Commencement June 2020

Doctor of Philosophy dissertation of Zhongwei Gao presented on December 19, 2019

APPROVED:

Major Professor, representing Chemical Engineering

Head of the School of Chemical, Biological, and Environmental Engineering

Dean of the Graduate School

I understand that my dissertation will become part of the permanent collection of Oregon State University libraries. My signature below authorizes release of my dissertation to any reader upon request.

Zhongwei Gao, Author

ACKNOWLEDGEMENTS

Firstly, I would like to express my sincere gratitude and heartfelt appreciation to my long-term advisor Dr. Chih-Hung Chang for his enormous support and invaluable guidance for the past years. I would also like to extend my appreciation to my Ph.D. research committee members: Dr. Gregory S. Herman, Dr. Chong Fang, Dr. Li-Jing (Larry) Cheng, and Dr. Xue Jin, for their time and commitment to my Ph.D. program.

I would also like to thank Teresa Sawyer and Dr. Peter Eschbach for their valuable assistance in SEM and EDS measurement, Dr. Rajiv Malhotra for his advice and support during my Ph.D. program.

Thanks to every group member in Chang's group : Dr. Seung-Yeol Han, Dr. Wei Wang, Dr. Yu-Wei Su, Dr. Katherine Han, Dr. Chang-Ho Choi, Dr. Paravee Vas-Umnuary, Dr. Dick Chiu, Dr. Ki-Joong Kim, Dr. Yujuan He, Guoheng Ma, Zhen Fang, Michele David, Qun Jing, Yujing Zhang, Han Mei, Ziyan Liu, Cheng Zeng, Shujie Li, Yu Cao, Jiayi Du, Hao Sun, Venkata Vinay Krishna, and Han Xu. Especially thanks to Dr. Changqing Pan for his advice and help in my research and dissertation, Dr. Yujuan He and Shujie Li for their advice and help in characterizaiton of the samples.

Last, but not least, I would like to thank my parents, Qunying and Yuanfeng for their longtime supporting. Without their support and enconragement, I won’t have the chance to study abroad.

TABLE OF CONTENTS

Page

Chapter 1: Introduction 1

  1.1 Thin film deposited by solution method 1

  1.2 Thin film deposited by batch reactor 2

    1.2.1 Mechanisms of chemical batch deposition (CBD) 2

    1.2.2 Reaction kinetics of the batch reactor 4

    1.2.3 Examples of the thin films deposited by CBD 6

  1.3 Thin film fabricated by continuous flow 7

    1.3.1 Reaction kinetics of the continuous flow reactor 7

    1.3.2 Example of thin film deposited by continuous flow 10

Chapter 2: Fabrication of Patterned ZnO Nanostructures by Using Microreactor-assisted Nanomaterial Synthesis and Printing Process 13

  2.1 Abstract 13

  2.2 Introduction 13

  2.3 Experimental and Simulation Methods 17

    2.3.1 ZnO deposited by continuous flow and PDMS channel 17

    2.3.2 Characterization methods for the film 18

    2.3.3 Process to make the PDMS 19

TABLE OF CONTENTS （CONTINUED）

Page

2.3.4 Growth mechanisms 21

2.4 Characterization 22

2.4.1 XRD and UV-Vis result 22

2.4.2 Film growth under different flow rate 24

2.4.3 Film growth under different temperature 27

2.5 Conclusion 40

Chapter 3 Patterned ZnO thin film part I. Novel, scalable approach to fabricate ZnO nanostructures with multiscale 3D geometric shapes 42

3.1 Abstract 42

3.2 Introduction 42

3.3 Experimental 45

3.3.1 Setup for the microreactor-assisted nanomaterial synthesis and the printing process and its characterization method 45

3.3.2 Procedures to make the PDMS channel 47

3.4 Results and Discussions for different Types of Patterns 48

3.4.1 The Spiral Patterns 48

3.4.2 Parallel lines 51

TABLE OF CONTENTS （CONTINUED）

Page

3.4.3 Patterns with symmetry structure 55

3.5 SEM result 60

3.6 Conclusion of the deposition of patterned ZnO film 60

Chapter 3 Patterned ZnO thin film part II. Application of the patterned ZnO nanostructure thin film 62

3.7 Introduction of the photocatalyst 62

3.7.1 Photocatalysis mechanisms 62

3.7.2 Improvement of the ZnO photocatalytic performance 64

3.7.3 Parameters that can influence the ZnO photocatalyst 66

3.7.4 Immobilized ZnO 68

3.8 Experimental 69

3.9 Characterization of the ZnO film on the quartz glass 72

3.10 Characterization of the photocatalytic performance of the device 73

3.10.1 The photocatalytic degradation of the MB with the time 73

3.10.2 Kinetics study 74

3. 11 Summary of the patterned ZnO photocatalytic performance 79

TABLE OF CONTENTS （CONTINUED）

Page

Chapter 4 Part I. CuO thin film fabricated by microreactor-assisted nanomaterial synthesis and the printing process 80

4.1 Introduction 80

4.2 Experimental 84

4.3 Result and discussion 86

4.3.1 CuO thin film fabricated with Cu/HMTA ratio at 1:2 86

4.3.2 CuO thin film fabricated at different bath temperature 87

4.3.3 CuO thin film fabricated at Cu/HMTA ratio at 1.5: 1 and 1: 6 88

4.3.4 Conversion of the $Cu_2(OH)_3NO_3$ to CuO 92

4.3.5 Conversion of the hydrophilic surface of CuO to hydrophobic 94

4.4 Conclusion 95

Chapter 4 Part II. ZnO/CuO diode fabricated by using the microreactor-assisted nanomaterial synthesis and the printing process 95

4.5 Introduction 95

4.6 Experimental details to fabricate ZnO/CuO 96

4.7 Characterizations of the ZnO/CuO heterojunction 98

4.7.1 UV VIS 98

TABLE OF CONTENTS （CONTINUED）

Page

4.7.2 SEM 99

4.7.3 Stylus profiler 100

4.7.4 Current-voltage characteristic of the ZnO/CuO diode 101

4.8 Summary 103

Chapter 5: Conclusion and future work 104

Bibliography 107

LIST OF FIGURES

Figure Page

Figure 1: Schematic illustration of the three different types of the reactors............... 10

Figure 2: Setup of the microreactor-assisted nanomaterial synthesis and the printing process... 17

Figure 3: Schematic diagrams showing the fabrication process of PDMS microchannel 20

Figure 4: a) XRD pattern for the ZnO nanorod coated on glass; b) optical image for the ZnO nanorod with different flow rate; c) UV-Vis absorption of ZnO film for different growth time; d) corresponding band gap at different growth time 23

Figure 5: Fixed flow rate at 3.85 mL/min after mixing, with changing resident time from (a) to (e) at 0.1 min, 0.21 min, 0.32 min, 0.42 min, and 0.5 min 25

Figure 6: Fixed residence time at 0.64 min, different flow rate from (a) to (e) at 1.28 mL/min, 2.57 mL/min, 3.85 mL/min, 5.14 mL/min, and 6.42 mL/min 26

Figure 7: Growth of the ZnO nanorod at increased flow rate from (a) to (f) at 2.57 mL/min, 3.85 mL/min, 5.14 mL/min, 6.42 mL/min, 7.70mL/min, and 8.99mL/min... 27

Figure 8: Schematic illustration of the stylus profiler measurement 28

Figure 9: Simulated temperature distribution in the tubing with different length: a) 45 cm; b) 100 cm... 29

LIST OF FIGURES （CONTINUED）

Figure Page

Figure 10: The thickness of the ZnO thin film at the center of the pattern: (a) scanning data by stylus profiler, (b) the average data from the scanning 31

Figure 11: ZnO grown at different flow rate, bath temperature and tubing length a) 45 cm tubing length, b) 100 cm tubing length and c) the comparison of the thickness at different tubing length. 33

Figure 12: Kinetics of the ZnO growth: a) thickness of the ZnO grown under different substrate temperature, b) growth rate at different substrate temperature, c) the Arrhenius form the growth rate constant, d) the surface temperature simulated by COMSOL under different T3. 35

Figure 13: SEM images of the ZnO nanorod film grown on silicon wafer (a) tilted cross-section of the ZnO film; (b) the top view of the film; (c) the EDS of the selected film; (d) the Profiler scan data... 37

Figure 14: (a) schematic diagram of the COMSOL simulation geometry; (b) the flow velocity profile close to the substrate; (c) the temperature distribution of the surface close to the substrate; (d) the temperatures of the solution from the cutline along the radical direction at the different spots along the flow direction; (e) the profiler scan at the similar spots as the cutline temperature. 39

Figure 15: Setup for the microreactor-assisted nanomaterial synthesis and the printing process for the patterned film.. 47

LIST OF FIGURES （CONTINUED）

Figure Page

Figure 16: Optical images of the spiral patterns: a) circles pattern, b) triangles pattern, and c) squares pattern 48

Figure 17: Thickness scanned by stylus profiler of the spiral circles, and the scan path 50

Figure 18: COMSOL simulation result: a) the surface velocity, b) the surface temperature, c) the velocity profile at the cutline 51

Figure 19: Optical images of the parallel patterns 52

Figure 20: Thickness measured by the stylus profiler and the scan path........ 53

Figure 21: Velocity of the solution flow in each channel: a) the parallel channels with the same width, (b) parallel channels with different width........ 54

Figure 23: Optical image of the symmetry sample........ 56

Figure 24: (a) Thickness of the film measured by profiler, (b) the scanning order and direction........ 57

Figure 25: a) COMSOL simulation for the velocity of the fluid in the channels, b) the temperature distribution of the pattern........ 59

Figure 26: SEM result for the ZnO symmetry pattern with different channel width, where Figure a) to e) reparents each channel with decreased width........ 60

Figure 27 Schematic illustration of the setup for the photocatalysis device for photodegrade the MB........ 71

LIST OF FIGURES (CONTINUED)

Figure Page

Figure 28 The thickness of the film measured by using profiler: a) the thickness of the film, b) the profiler measurement order and the flow direction for deposition of the ZnO film.. 72

Figure 29 UV-VIS absorption spectra of the MB solution from the reservoir measured in an interval of 30min: a) the change of the absorption spectra, b) the change of the MB concentration in the solution.. 73

Figure 30 a) the absorption intensity of the MB after photodegradation; b) relation between k'_{obs} and the flow rate 76

Figure 31 a) Photocatalytic efficiency under different total amount of the MB; b) under different flow rate.. 78

Figure 32 Schematic illustration of the deposition process of $CuO/Cu_2(OH)_3NO_3$ ... 84

Figure 33 SEM image of the CuO film grown by MAND&PDMS channel and the EDS result for the films 86

Figure 34 CuO deposited with bath temperature at: (a) 80˚C and (b) 90˚C 88

Figure 35 SEM image of the CuO film deposited with Cu/HMTA ratio at: a) 1:6 and b)1.5:1, and the corresponding EDS result:c),d)...................................... 90

Figure 36 Schematic illustration of the growth of different film morphologies under different deposition condition 91

Figure 37 a) Optical image of the $Cu_2(OH)_3NO_3$ before and after annealing; b) SEM image and c) EDS result of the annealed $Cu_2(OH)_3NO_3$ 93

LIST OF FIGURES （CONTINUED）

Figure Page

Figure 38 XRD patterns of the CuO and $Cu_2(OH)_3NO_3$ 93

Figure 39 Contact angle for the (a) as-deposited CuO film by CBD method, (b) the uncoated substrate contacted with PDMS during deposition, (c) the CuO after 2 weeks in air. 94

Figure 40 Process to fabricate ZnO/CuO/Au diode 97

Figure 41 UV-VIS spectrum of a) as-deposit CuO film and b) ZnO film on glass. Inserted images are the calculated bandgap 98

Figure 42 (a) Cross-sectional SEM image of ZnO/CuO/Au, and (b)elemental mapping of Cu and Zn 100

Figure 43 Thickness of CuO and ZnO/CuO measured by stylus profiler................. 101

Figure 44 a) Forward and reverse bias I-V characteristics of ZnO/CuO heterojunction on each line, b) the rectifying behavior.. 102

Growth, Characterizations, and Applications of Patterned Nanostructured Thin Film

CHAPTER 1: INTRODUCTION

1.1 Thin film deposited by solution method

Solution method is one of the chemical methods that using the dissolved chemical reactants to form a thin film on the surface of a substrate, through chemical reactions either occurring directly on the interface between the solution and the solid substrate, or in the solution phase and precipitate onto the substrate. The solution method has been widely used to fabricate the metal oxide and chalcogenide functional thin films, such as ZnO, TiO_2, CuS, SiO_2, and CdS. Those oxide or sulfide thin films have been intensely researched in many fields and have shown important applications such as the light-absorbing layers or electron transporting layers in solar cells, channel layers for the thin film transistors, antireflective coatings and sensors.

Unlike the physical methods, such as the sputtering or thermal evaporating methods that require high vacuum ($\leq 10^{-6}$ mPa)[1], high temperature, and high purities of materials ($\geq$99.999%)[2], the solution method can take place under relatively low temperature (usually lower than the boiling temperature of the solvent) and ambient pressure, which makes it an attractive method to deposit thin film at a low cost. Also, due to the different reaction path, various of the nanostructures of the thin film can be fabricated, including the rod-shaped, spherical, or cubic nanostructures.

A solution method to deposit thin film always involves chemicals and chemical reactions, and a chemical reactor is where the chemical reaction takes place. There are three basic types of the chemical reactors: batch, continuous-stirred-tank, and plug flow reactors.[3] Many complex chemical reactors can be simplified and decomposed to these simple reactors. Usually chemical batch deposition method and plug flow reactors are used to deposit thin films.

1.2 Thin film deposited by batch reactor

1.2.1 Mechanisms of chemical batch deposition (CBD)

In a typical CBD process for the metal chalcogenide thin film deposition, the metal salt and the chalcogen source are dissolved into the solution along with the immersed substrate. The metal ions can form the metal complex with a complexing ligand in the solution to a lesser or greater extent. The ligand could be the solvent itself, such as the polarized water molecule or the other added complexing agent, for example, NH_3. Those metal complexes undergo reversible reaction to release the metal ions and complexing ligands, and eventually reach the equilibrium state where both the metal ions and metal complexes are existed in the solution at a certain concentration. The complexes formed in the solution play an important role in CBD process, for example, the amount of the metal ions in the solution is reduced to prevent rapid precipitation of the final product. The metal ions are released into the solution in a slowed rate so that the overall reaction can be smooth and stable. Sometimes, the complexing agent added into the solution can also control the growth of the nanostructures, for example, during the formation of the ZnO nanorods grown by CBD process, the hexamethylenetetramine (HMTA) shows a strong hindrance effect and can guide the growth of the ZnO nanorod in some certain direction.[4]

However, the solution cannot maintain stable forever due to the existence of the chalcogen ions or hydroxide ions. The metal ions and the chalcogen or hydroxide ions can form the nanoparticles in a certain reaction rate, depending on the temperature and concentration of the reactants. During the initial stage of the formation of the nanoparticles, the nuclei are formed due to the collision between individual ions or molecules, which is called as a nucleation process. The nucleation process can either occur in the solution phase, which is called homogeneous nucleation, or occur on the surface of the substrate, which is called heterogeneous nucleation. The heterogeneous nucleation occurs on the surface to reduce the surface energy. Usually, both types of nucleation processes co-exist in solution and compete to form the nuclei in solution and on the substrate.

After the formation of nuclei in the solution, the nuclei undergo a crystal growth process to increase the size and further form a nanocrystal. There are several paths to form the nanocrystals, either by adsorption of ionic species from the solution, or by aggregation of the nuclei and further form larger nanocrystals. Again, the growth of the crystals can either occur in the solution phase or at the interface between solution and substrate, to eventually form a precipitation of the nanoparticles or the thin film.

There are four basic mechanisms to consider in a CBD process: 1) the simple ion-by-ion mechanism, where the final product is formed by ionic reaction and the major reactants are molecules or ions; 2) the simple cluster mechanism, where a solid phase is formed first and followed by substitute reaction to form final product; 3) the complex decomposition ion-by-ion mechanism, where the complexes are formed firstly, followed by decomposition of the complex to form the final product; 4) the complex decomposition cluster mechanism, where the conversion of the product is from the solid intermediate.[5]

Notably, it is very rare to isolate only one mechanism in a CBD process, in most case all the mechanisms occur during the formation of the thin film, but to a different degree.

1.2.2 Reaction kinetics of the batch reactor

A batch reactor is the simplest reactor, where all the reactants are put into a container, with a stir bar to promote the mixing of the solution. The container can be optionally heated to maintain the solution in some certain temperatures for the reaction to carry on. The CBD process mentioned above often takes place in the batch reactor, as the indicated by the name. Therefore, the material balance for the CBD process can be modeled by using the batch reactor.

To gain some insights into the kinetics of the bath reactor, the batch reactor is assumed to be well-mixed and the volume of the reactor is also a constant. The reaction is assumed to be the first order, irreversible reaction as shown below:

$$\mathrm{A} \xrightarrow{k} \mathrm{B} \tag{1.1}$$

The concentration of the reactant A with the time can be calculated based on the mass balance:

$$\frac{dC_A}{dt} = -kC_A \tag{1.2}$$

where k is the reaction rate constant, and can be represented by using the Arrhenius rate expression:

$$k = A\exp\left(-\frac{E_a}{RT}\right) \tag{1.3}$$

where the A is a pre-exponential factor depending on the frequency of the collision among atoms and molecules, E_a is the activation energy, which is the minimum energy for a reaction to occur. R is gas constant, and T is the temperature. From the Arrhenius expression, the reaction rate constant is temperature dependent.

The concentration of the reactant changing with time (t) can be solved as:

$$C_A = C_{A,0}\exp\left(-kt\right) \tag{1.4}$$

where the $C_{A,0}$ is the concentration of the reactant A in the initial stage. From the equation, it can be found that the concentration of the reactant A is decreasing exponentially with the increasing of time. As a result, if there is only one reactant in the solution, the growth rate of the film cannot reach to a steady state. However, in the CBD process, several reactants are added to the reactor, multiple reactions will take place in series or parallel with different reaction rates. In addition, reversible reactions can occur, and their equilibrium state can be reached in a different time scale. Thus, the overall reaction rate for the final product can be potentially estimated. For example, Zhou & Deng studied the ZnO nanorod formation in solution by assuming a quasi-steady state reaction and achieve three first-order reactions to describe overall reaction.[6] In this way the growth rate of ZnO nanorod can be estimated by knowing the reaction temperature and starting concentration of the species.

1.2.3 Examples of the thin films deposited by CBD

Efforts have been made to study the CBD process for the thin film. For example, Vas-Umnuay & Chang used the quartz crystal microbalance (QCM) to study the growth kinetics of the copper sulfide thin film by CBD process.[7] In the experiment, the copper sulfate ($CuSO_4$) was used as the metal ion source, and thiourea as the chalcogen ion source, which will undergo a hydrolysis in the water solution. The ammonium hydroxide (NH_4OH), sodium acetate (CH_3COONa) were added as the complexing ligands. The study focused on the kinetics of the formation of the copper sulfide film, by using the QCM to monitor the growth rate of the film.

Another material deposited by the CBD process is the CdS thin film, which is a window layer for the CdTe or CuInSe solar cells.[8] There are different mechanism and pathways to form the CdS, including the ion-by-ion reaction between free Cd^{2+} and S^{2-} ions to form the CdS, or the clusters reaction where the $Cd(OH)_2$ formed from hydrolysis reacts with the S^{2-} to produce the CdS. It can also form an intermediate compound, $CdSC(NH_2)_2^{2+}$ and then breaking the bond to form CdS.[9]

Silver thin film can also be formed through CBD process by using the glucose to reduce the Ag^+ ion to Ag. This reaction is called Tollens reaction.[10] In this process, the silver nanoparticles can also undergo both homogeneous and heterogeneous reaction, to form the silver thin film on the substrate surface. However, the heterogeneous deposition can be limited, and the homogeneous reaction can be well controlled by introducing the metal seeds and ligands into the solution. The metal seeds mainly work as the nucleation sites for the homogeneous reaction to occur. It also can determine the structure of the silver nanocrystals, so that the different shapes such as silver nanowires or silver nanocubes can be formed.[11] The ligand, usually the polyvinylpyrrolidone (PVP) mainly works as the capping agent for the crystal growth. The PVP will interact strongly on some certain face to limit the contact between the reactants from the solution and the crystal surface, and the silver crystal will only grow on one direction to eventually form the silver nanowire.[12]

1.3 Thin film fabricated by continuous flow

One disadvantage of the batch reactor is that it cannot generate the final product in a constant rate, as it can be found from equation (1.4), where the concentration is changing with time, and eventually the reaction will be terminated as the reactants depleted. Also, with the concentration of the reactants changing with time, multiple reactions can occur in the batch reactor, which makes it difficult to control the final product.

To overcome these disadvantages, the continuous-stirred-tank reactor (CSTR) is used. A typical CSTR has at least one feed flow and one out flow connected to a container. In this way, the reactants are entering to the reactor continuously, while products and unreacted species are leaving the reactor at the same time.

1.3.1 Reaction kinetics of the continuous flow reactor

For a same first-order, irreversible reaction as equation (1.1) in a CSTR with a constant volume and well mixed solution, the mass balance for the reactant A is:

$$\frac{dC_A}{dt} = F_0 C_{A,0} - FC_A + R_A V_R \qquad (1.5)$$

F_0 and F is feed in flow rate and out flow rate and have a same value if the reactor volume V_R is kept constant. $C_{A,0}$ is the concentration of reactant A before entering the reactor, and C_A is the concentration of reactant A in the reactor, assuming a well-mixed solution in the reactor. R_A is the reaction rate of reactant A. The reactor can reach the steady state, and the concentration of reactant A can be obtained by setting equation (1.5) to 0, which yields:

$$C_A = C_{A,0} + \frac{R_A V_R}{F} \tag{1.6}$$

From equation (1.6), the concentration of the reactant is a constant independent of time. It is possible to achieve a growth of thin film in a steady rate by using a continuous flow, since the concentration of the reactant is not changing with time.

Similar to the CSTR, a plug-flow reactor (PFR) has both inlet flow and outlet flow, but the reactor itself is a tubing. Also, an ideal-flow assumption is applied to the PFR, so that the solution in the tubing is assumed to be well mixed in the radial and angular directions.[5]

Again, for a first-order, irreversible reaction (1.1), the mass balance for the reactant A can be written as:

$$\frac{\Delta C_A}{\Delta t} = -\frac{\Delta C_A v}{\Delta z} + R_A \tag{1.7}$$

where z is the direction of the flow, v is the velocity.

For a PFR in a steady state, by setting $\frac{\Delta C_A}{\Delta t} = 0$, yields:

$$\frac{dC_A}{d\tau} = R_A \tag{1.8}$$

where $\tau = L/v$ is the residence time.

Solving equation (1.8) gives:

$$C_A = C_{A,0} \exp\left(-k\tau\right) \tag{1.9}$$

For the equation (1.8) and (1.9), it can be found that at steady state, the concentration of reactant is different along the flow direction, but remains constant with time. Similar as deposition process in a bath reactor, the deposition process by continuous flow also involves the nucleation and growth of the nanoparticles. There are two major advantages of the deposition process by continuous flow:

1) The concentration and the composition of the solution leaving the reactor is constant. In a bath reactor, the reactants concentration is changing with time, as shown in equation 1.5. While in a continuous flow reactor, the convection and the reaction can reach a balance state, so that the concentration and the composition of the solution is fixed, which enables a continuous growth of the film.

2) The composition of the precursor solution can be easily controlled by the residence time. The residence time ($\tau = L/v$) mainly determines the total time that a fluid flows through a reactor. By controlling the residence time, different stages of the growth of the crystal can be isolated, resulting in a formation of the building blocks ranging from the ionic reactants, nuclei, or nanocrystals. Those building blocks can be further supplied to the substrate for the growth of the film. Since the formation of these

building blocks can be controlled and fixed at a constant concentration, it is possible to identify which building block leads to the growth of the deposition of the film, which can provide some insights on growth mechanism of the film. A schematic illustration has summarized the three different types of the reactors in Figure 1.

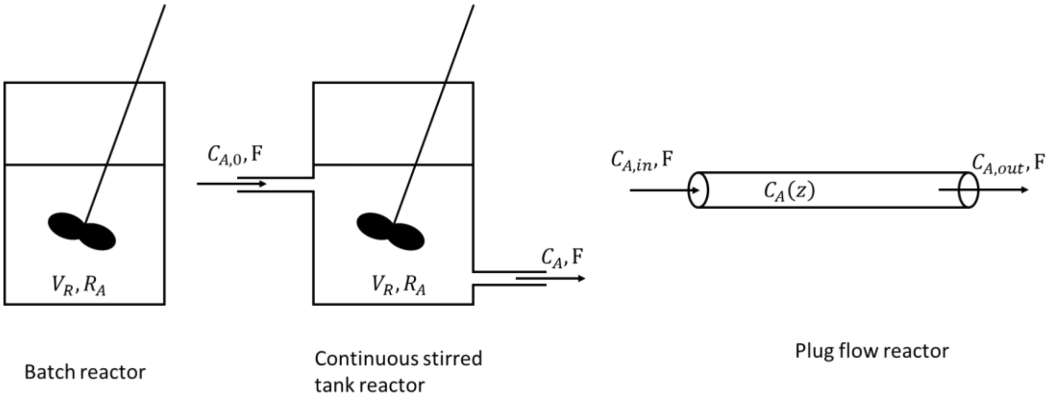

Figure 1: Schematic illustration of the three different types of the reactors

1.3.2 Example of thin film deposited by continuous flow

Different thin film materials have been deposited by continuous flow reactor. For example, silver nanowires can be synthesized by a polyol reduction method through a continuous flow reactor.[13] The result shows a higher conversion and yield by using a continuous reactor than a regular bath reactor. McPeak & Baxter reported the deposition of the ZnO nanorod on a heated silicon wafer by using a continuous flow microreactor to flow the precursor solution through a channel and showed that the growth mechanisms and material properties varied along the length of the substrate.[14] Choi *et al.* demonstrated that highly conductive silver can be fabricated by using a microreactor-assisted printing process where the mixed solution by continuous flow was directly delivered onto glass or polymeric substrates to deposit dense and uniform silver.[15] Other thin films deposited by continuous flow, such as CdS and CuS have also been reported.[16,17]

The residence time plays an important role in microreactor system. For example, Su *et al* produced CdS nanoparticles in a continuous flow microreactor and found that the particle size increased with the residence time.[18] And they also proposed the growth mechanism for the formation of the CdS nanoparticles is the barrier-controlled coalescence. He *et al* synthesized hollow silica nanoparticles using a microreactor-assisted system and by controlling the mixing process, different pathway of hollow silica nanoparticle formation can be achieved.[19] The continuous flow in a channel can also be applied for the assemble the one-dimensional structures, for example, nanowires can be assembled into parallel arrays by the fluidic flow.[20]

In this study, the microreactor-assisted nanomaterial synthesis process is combined with a polydimethylsiloxane (PDMS) channel to print patterned thin film on a substrate. In the process, the precursor solution with the controlled composition and concentration is firstly generated by microreactor process, and then supplied to the channel made by PDMS and the substrate surface. As the solution flows through the channel, a surface reaction occurs on the substrate surface, which enables the thin film deposition on the substrate. What’s more, as different channel shapes can be designed, different patterns of the thin film can be left on the substrate surface after the solution flow through the channel. By applying this process, different nanostructured thin film including ZnO and CuO are successfully deposited onto various substrates. The growth kinetics and mechanisms are studied by controlling the film deposited under different conditions, including the different flow rates, different growth temperatures, and the different initial concentrations of the reactants. Different functions of the patterned nanostructured thin film are also investigated in this study.

CHAPTER 2: FABRICATION OF PATTERNED ZnO NANOSTRUCTURES BY USING MICROREACTOR-ASSISTED NANOMATERIAL SYNTHESIS AND PRINTING PROCESS

2.1 Abstract

In this study, we developed a method to fabricate a patterned ZnO thin film by using a combination of microreactor-assisted deposition process and microfluidic channels. This method allows a separation of the homogeneous reaction in the solution and the heterogeneous reaction on the substrate surface, resulting in a well-controlled growth of the ZnO on the substrate surface so that the growth mechanisms and kinetics can be studied. The microreactor assisted nanomaterial synthesis process can generate nanoscale building blocks with controlled sizes, ranging from molecule clusters to nanoparticles with constant concentration and compositions. Those nanomaterials serve as building blocks and can be delivered to the substrate surface through the microfluidic channels for the thin film growth. The microfluidic channels were made of cured polydimethylsiloxane (PDMS) by using a replication from a patterned SU-8 photoresist-coated glass. The growth kinetics of the ZnO on silicon wafers were studied by measuring the thickness of the film using the stylus profiler and scanning electron microscope under various growth conditions controlled by using the microreactor and the PDMS channel.

2.2 Introduction

ZnO has attracted enormous attentions as an important multifunctional material due to its unique chemical, electrical and optical properties that have found applications in the areas such as cosmetics, photocatalysis, sensors, solar cells, transistors, and piezoelectric transducers. Also, ZnO is earth abundant, low cost, and facileness to make. ZnO is an n-type material with a band gap of 3.37eV and a large exciton binding energy of 60 meV.[21] ZnO can exist in three different crystal structures, including the hexagonal wurtzite, cubic zincblende and rocksalt. The hexagonal wurtzite is the most thermodynamically stable structure at the room temperature, where a number of alternating planes composed of tetrahedrally coordinated O^{2-} and Zn^{2+} ions stack alternately along the *c*-axis.[22] ZnO can be synthesized into different nanostructures, including the one dimensional structure such as ZnO nanorods or nanowires[23], two dimensional structures such as ZnO nanosheet or nanoplates[24], and three dimensional structures such as nanoflowers[25] or spheres.[26] ZnO nanostructures with different morphologies, sizes, surface areas and activities demonstrate different chemical and physical properties. Owing to its diverse morphologies and properties, ZnO has found applications in many areas: for example, ZnO nanorod can work as a photoelectrode for dye sensitized, quantum dot, organics or perovskite solar cells, where the one dimensional ZnO nanorod offers a fast electron transport pathway.[27,28] In addition, ZnO nanostructures have also been widely studied as a photocatalyst material due its ability to generate the OH· radicals on the surface, which can be used to decompose the organic pollutants. The morphologies of ZnO nanostructures play an important role in the photocatalytic performance and have been intensely studied to enhance its performance by increase its surface to volume area with active catalytic sites.[29,30] Also, the ZnO nanostructures can be used in gas sensors, where the absorbed gas molecules on the ZnO surface can alter its electrical conductivity. The amount of the absorbed gas molecules depends on the morphology of the ZnO nanostructure, thus influence the sensing performance.[31,32] ZnO nanostructures have also been fabricated in light emitting diodes[33] and piezoelectric nanogenerators.[34]

The many promising applications of ZnO nanostructures have driven the development of various processes to fabricate ZnO nanostructures with a plethora of morphologies, including hydrothermal synthesis[25,35], chemical vapor deposition[36], physical vapor deposition, and atomic layer deposition.[37] In the hydrothermal method, the ZnO nanostructure growth process is carried out in the solution phase, where the Zn source is dissolved in the solution. While in chemical vapor deposition process or atomic layer deposition process, the reaction is carried out in the gas phase in a closed chamber. Comparing to reaction in the gas phase, solution-based processes have been extensively studied, due to its ease to operate, low cost and capability to generate different nanostructures by controlling the reaction conditions.[31,38–40] For example, Amin *et al.* has shown that in a hydrothermal deposition process, ZnO with nanotetropod-like, flower-like, and urchin-like structures can be obtained by controlling the pH, the concentration, the reaction time and the growth temperature.[41] In addition, efforts have been made to grow patterned ZnO thin film with different nanostructures by using ink-jet printing[42], microcontact printing, and lithography.[43] The ability to fabricate patterned ZnO nanostructured thin films is one of the key enablers of making functional ZnO-based devices, such as the ZnO stretchable energy harvesting device[44], solar cells, light emitting diodes, sensors or field emission devices.[45]

In order to have a better understanding and better control of the ZnO growth process, a few studies have focused on the growth mechanism and kinetics. For example, Zhou *et* *al.* developed a kinetics model by assuming a first-order reaction mechanism to fit the experimental result and estimated the growth kinetics of the ZnO nanorods.[6] Boercker *et al.* discovered the growth of the ZnO in the solution was limited by mass transport of the Zn^{2+}.[46] Viswanatha *et al.* investigated the growth of ZnO nanocrystals from solution and estimated the activation energy by using the Lifshitz-Slyozov-Wagner theory.[47] Those studies have given some insights of the kinetics and mechanisms of the ZnO growth.

Recently, we have demonstrated the fabrication of patterned nanostructured thin films by using a Microreactor-Assisted Nanomaterials Synthesis and Printing process. The process utilizes a microreactor system to generate a solution containing reactive nanobuilding blocks which is then delivered to a substrate surface guided by a microchannel. This process has been demonstrated to be an efficient approach to fabricate the thin films[14,48,49] that enables the precise control of the reaction parameters while reduces the byproduct formation.[50] It also provides a unique opportunity to study the reaction mechanisms, including the reaction kinetics. In particular, the continuous flow microreactor is capable of generating and transporting a chemical reactive solution with a well-controlled concentration, and temperature. Furthermore, the separation of reactant generation and heterogeneous surface reaction allow the possibility to decouple the homogeneous reactions for the reactant production in the solution from the heterogeneous surface reactions associated with the film formation. In contrast, the concentration of the reactants in a batch reactor is constantly changing as a function of reaction time. In this work, the growth kinetics of patterned ZnO nanowire arrays were studied by characterizing the nanostructured ZnO films from various processing conditions and supported by process simulations using COMSOL Multiphysics program.

2.3 Experimental and Simulation Methods

2.3.1 ZnO deposited by continuous flow and PDMS channel

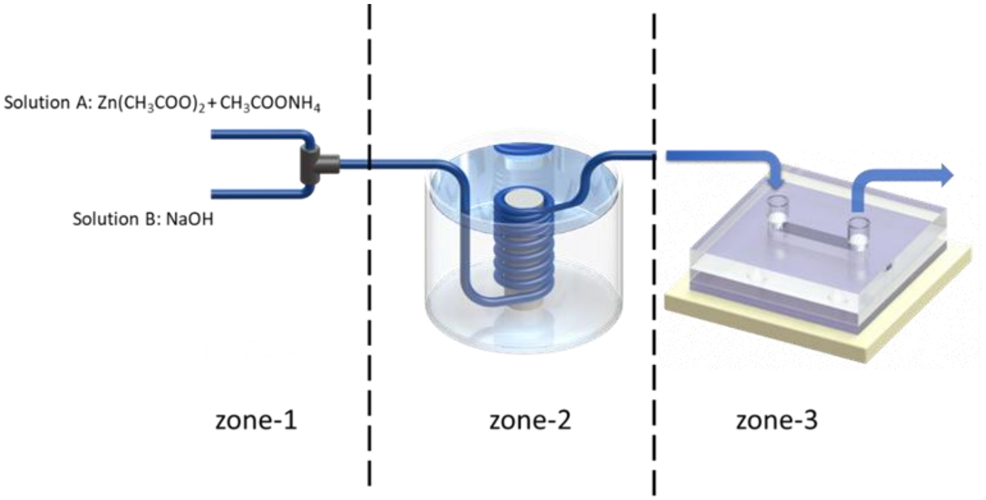

Figure 2: Setup of the microreactor-assisted nanomaterial synthesis and the printing process

The overall ZnO thin film growth setup was illustrated on Figure 2. The setup contains three zones, a mixing zone (zone-1), a reactant generation zone (zone-2), and a deposition zone (zone-3). The recipe is similar to the one reported in the literature[51]: 0.2195 g of zinc acetate ($Zn(CH_3COO)_2 \cdot 2H_2O$, Sigma) and 0.1925 g of ammonium acetate (CH_3COONH_4, Mallinckrodt Chemicals) dissolved in 200 ml of deionized water to form solution A and 0.8 g of sodium hydroxide (NaOH, Macrom Fine Chemicals) dissolved in 200 ml of deionized water to form solution B. The two solutions, solution A and B, were pumped into two PVC tunings separately and then mixed through a micro-T-mixer. The chemical mixture was then passed through a helical structured reactor made by wrapping a PVC tubing with 1/16 inch in inner diameter around a cylinder. The length of the PVC tubing was varied during the process in order to control the residence time and the solution temperature. The temperature of the reactor was controlled by immersing the PVC tubing in a water bath, sitting on a temperature-controlled hot plate.

The precursors for the growth of ZnO nanorods, formed in the zone-2 microreactor, were then supplied to the zone-3 microchannel for the growth of patterned ZnO nanorods on the substrate. The microchannel was sandwiched between the substrate and a polycarbonate holder to act as both a fluidic channel and a patterning tool. The growth of patterned ZnO nanorods were carried out on the substrate by varying the substrate temperatures, the deposition time, the tubing length and the solution flow rate to study the kinetics of the patterned ZnO nanorod film formation process.

Before the growth of the ZnO thin film, a ZnO seed layer was firstly formed on the substrate surface by spin coating a 0.025 M of zinc acetate ($Zn(CH_3COO)_2{\cdot}2H_2O$, Sigma Aldrich) in ethanol solution followed by annealing the substrate at 250 °C in the air for 1h. The main purpose for this seed layer is to provide a nucleation sites for the growth of ZnO nanorods.

2.3.2 Characterization methods for the film

The morphology of the film was characterized using a scanning electron microscope (SEM, FEI QUANTA 600 FEG environmental SEM) with an accelerating voltage of 10 kV. The substrates were cut through the center of the film and were placed into the SEM chamber with a tilted angle of 45 degree. In this way, the actual distance is always 1.41 times the observed distance. In this paper, all the presented thickness of the film was after correction. X-ray diffraction analysis (XRD, Bruker-AXS D8 Discover) was used to characterize the crystal structures of the ZnO film. The absorption properties of the ZnO film were measured by a UV-Vis spectrophotometer (Jasco, V-670). The thickness of the film was measured by a programmable stylus profiler measuring system (Dektak 8).

COMSOL simulation was applied to study the heat transfer and solution transport phenomenon in zone-2 and zone-3. In the simulation, a laminar flow with different flow rate was passing through a tubing with controlled wall temperature. In this way, the solution temperature leaving the zone-2 can be estimated according to the COMSOL simulation result. Also, the temperature distribution in the channel in zone-3 was also estimated.

2.3.3 Process to make the PDMS

Schematic diagrams showing the fabrication process of PDMS microchannel are given in Figure 3. The method to make the microchannel is similar to the method described in the literature to make the PDMS stamp in soft lithography.[52] An SU-8 master was firstly created on a silicon wafer. The target thickness of the PDMS microchannel is about 1000 µm. In order to achieve a thickness of 1000 µm of SU-8 on the silicon wafer, a 1.5 × 1.5 × 0.4 inch of PLA plastic framework was firstly glued on the wafer surface as shown in Figure 3. This framework mainly worked as a block to prevent the movement of the uncured SU-8 since 1.68 g of SU-8 in an area of 15 cm^2 is needed to achieve 1 mm thick of SU-8 film. The SU-8 2010 (Micro Chem) was poured onto silicon wafer in the area surrounded by the framework. The SU-8 was under soft bake at 60 °C for 12h, and then the SU-8 was exposed UV light with a patterned mask covered on the top. The SU-8 under exposure of UV light was cured and hardened. After curing, the SU-8 was moved to oven under 60 °C for hard bake for 1h. The SU-8 developer (Micro Chem) was used to remove uncured SU-8 and an SU-8 line with thickness and width of 1mm, and length of 19 mm was coated on the wafer. To fabricate the PDMS channels, PDMS (Sylgard 184, Dow Corning) and PDMS curing agent (Dow Corning) were mixed in a ratio of 10 to 1. After degasification for 1 hour, the mixture was poured onto the SU-8 master and annealed at 80℃ for 15 min, where liquid PDMS turned into elastic solid. The channel was left on the PDMS after removed from the wafer.

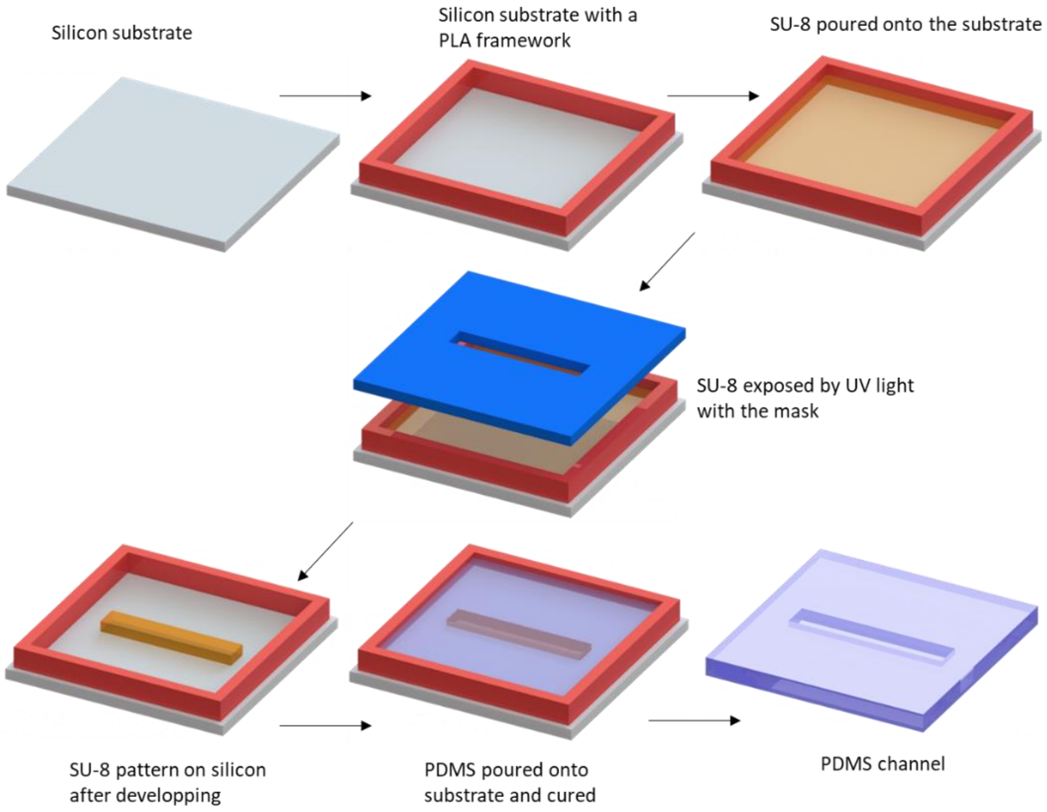

Figure 3: Schematic diagrams showing the fabrication process of PDMS microchannel

2.3.4 Growth mechanisms

In our process, the reactor contains three zones, a mixing zone, a reactant generation zone, and a deposition zone. Two solutions containing Zn^{2+} ions and OH^- were brought into contact via a T-mixer, a series of reactions occur in the mixed solutions, in zone-2, to form a variety of reacting species including $Zn(OH)_2$, which is considered as the major precursor for the formation of ZnO.[35-38] Formation of ZnO nanoclusters and nanoparticles can also occur in zone-2 if the processing condition allows. The formation of these species, such as ZnO nanoclusters and nanoparticles, will lead to the reduction of $Zn(OH)_2$ concentration.

When delivered to the PDMS channel in zone-3, the $Zn(OH)_2$ precursor in the solution can react on the substrate surface, due to the existence of the seed lays formed previously by spin coating. The seed layer serves as the nucleation sites for the formation of the nanorods and is essential for the oriented growth the film.[53–55] In this study, the formation of ZnO on the substrate surface is considered as the first-order reaction kinetics, where the reaction rate is only a product between the concentration of the $Zn(OH)_2$ on the substrate surface and the reaction rate constant *k*. The reaction rate constant *k* is only function of temperature and the concentration is controlled by the mass transport of the precursor species[46] at the interface and the surface reaction at the interface between the precursor solution and the solid substrate. A steady state can be reached among the convection, diffusion and reaction of the $Zn(OH)_2$, resulting in a constant concentration of the precursor at the interface between liquid and solid substrate. The similar problem has been widely studied in the mass and heat transport phenomenon, known as the Graetz problem.[56,57]

We controlled various processing parameters, to carry out growth experiments to better understand the process, including the flow rate in zone-1, the temperature T-2 in zone-2, the residence time in zone-2 (changing the tube length and flow rate), the substrate setting temperature T-3 in zone-3, and growth time in zone-3. For example, we studied the growth rates of ZnO nanorods as a function of substrate temperature by varying the T-2 in zone-2, while keeping the reactive chemical flux delivering from zone-2 as a constant. In this way, the growth rate as a function of the substrate temperature can be obtained, and the activation energy can be determined.

2.4 Characterization

2.4.1 XRD and UV-Vis result

The XRD pattern of the ZnO nanorod deposited on glass slide was presented on Figure 4(a). The amorphous glass slide was chosen instead of the silicon wafer to avoid the XRD peaks from the substrate. From the XRD pattern, it can be clearly found that the peak at $2\theta = 34°$, corresponding to the (002) direction, has the strongest intensity and sharp peak, which indicates that the ZnO nanorod has a wurtzite structure with highly crystallinity, and is preferably grown in *c*-axis direction.[58]

Figure 4(b) is the optical image for the ZnO line coated on the silicon. Those lines were fabricated in an increased flow time from left to right (5 min, 10 min, 15 min, and 20 min), resulting in an increased film thickness from left to right. Both the bath temperature T-2 in zone-2 and the deposition temperature T-3 in zone-3 were kept at 60 °C. The colors of the film also change with the growth time and the thickness due to the interference between the substrate and the film.

Figure 4(c) and (d) are the UV-Vis absorption peak of the ZnO grown at different time (5 min, 10 min, 15 min, and 20 min) on the glass substrate and the corresponding band gap energy calculated from the Tauc plot. The spectrum has shown an absorption peak at 349 nm, and a corresponding band gap of 3.37 eV, for the ZnO thin film with different thickness.

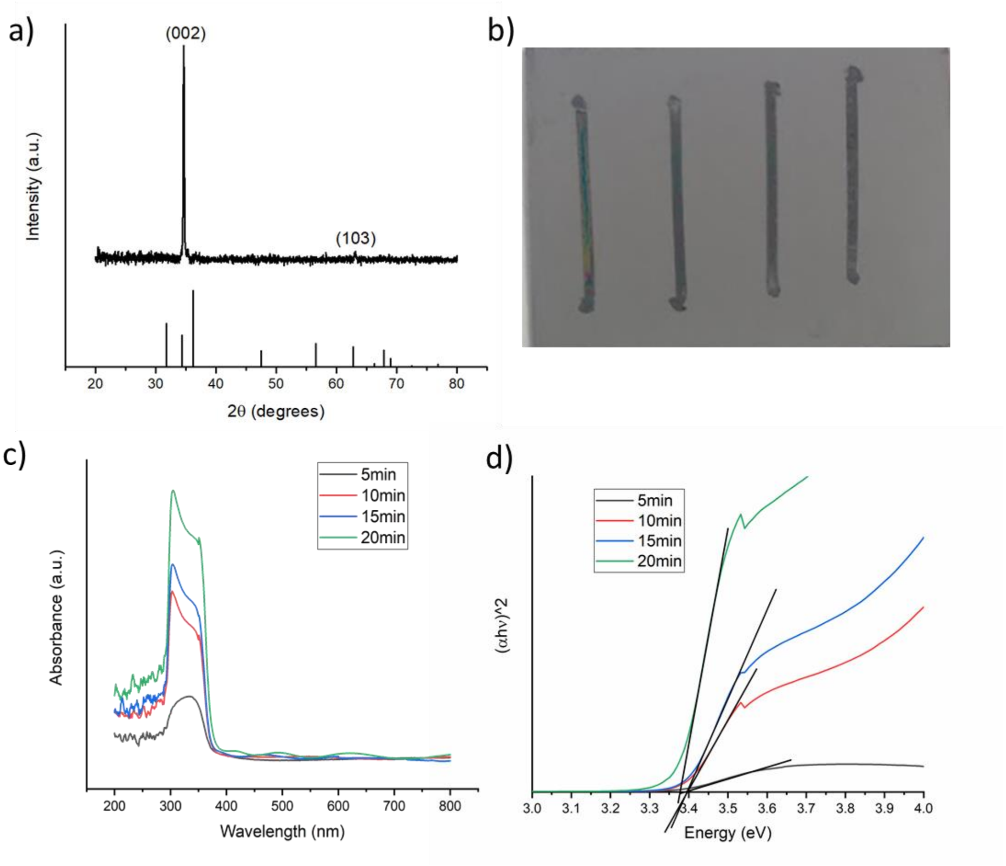

Figure 4: a) XRD pattern for the ZnO nanorod coated on glass; b) optical image for the ZnO nanorod with different flow rate; c) UV-Vis absorption of ZnO film for different growth time; d) corresponding band gap at different growth time

2.4.2 Film growth under different flow rate

Film growth under fixed flow rate and different residence time

To better understand and control the growth behavior of the microreactor-assisted nanomaterial synthesis and the printing process, different flow rate of the precursor solution and residence time in the tubing in zone-2 was applied. The fluorine doped tin oxide (FTO) substrates were used for the ZnO growth. The bath temperature (T-2) in zone-2 was fixed at 70 °C, and the substrate temperature (T-3) was fixed at 100 °C.

To investigate how the precursor formation process will influence the ZnO nanorods growth, the ZnO thin film were deposited for 20 min under fixed flow rate at 3.85 ml/min after mixing but the length of the tubing were changed so that film growth under various residence time at 0.1 min, 0.21 min, 0.32 min, 0.42 min, and 0.5 min can be studied. In this way, the compositions of the precursor solutions were different due to the different residence time but the flow rate in the PDMS channel in zone-2 was fixed. The SEM images from the Figure 5 have shown that the thickness of the ZnO nanorod is decreasing with the increasing of the residence time, which is most likely due to the homogeneous reaction in the zone-2 consumed reactants in the solution to form the ZnO nanoparticles in the liquid phase. As a result, a lower concentration of the $Zn(OH)_2$ in the precursor solution is delivered to the substrate surface as the residence time increased, resulting in a thinner ZnO film.

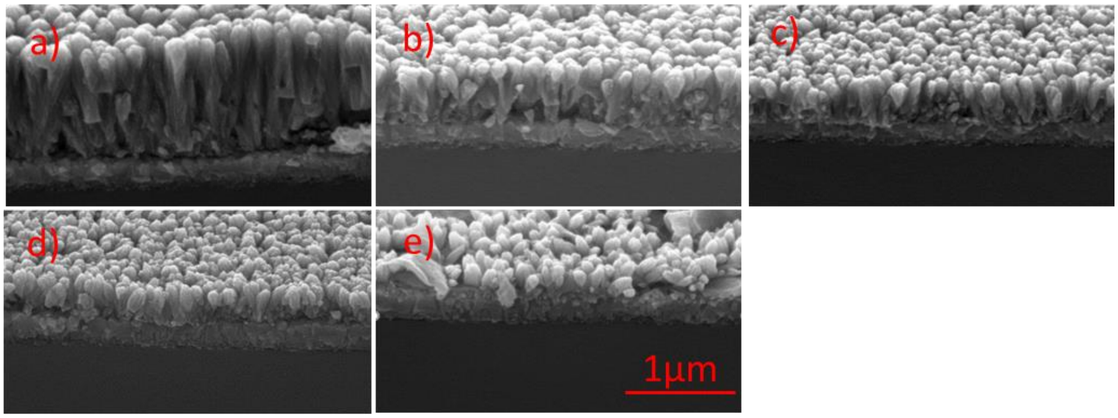

Figure 5: Fixed flow rate at 3.85 mL/min after mixing, with changing resident time from (a) to (e) at 0.1 min, 0.21 min, 0.32 min, 0.42 min, and 0.5 min

Film growth under different flow rate but fixed residence time

The growth of the ZnO nanorod was performed under same residence time but different flow rate. Different flow rate was chosen at 1.28 ml/min, 2.57 ml/min, 3.85 ml/min, 5.14 ml/min, and 6.42 ml/min, to investigate how the flow rate can impact the ZnO formation. Also, to avoid the influence of the homogeneous reaction from zone-2, the residence time was kept same at 0.32 min for all those five reactions by using different length of the tubing. In this way, the solution composition leaving zone-2 was identical, despite the difference in flow rate and only flow rate in zone-3 is different. From the SEM images in Figure 6, it clearly shows the increase of the thickness of the ZnO nanorods with the flow rate. Since the concentration of $Zn(OH)_2$ leaving zone-2 are same, the increased thickness of the ZnO film on the substrate is due to the increased flow rate in zone-3, where more $Zn(OH)_2$ is transported to the substrate surface to compensate the consumption of the reactants caused by the surface reaction.

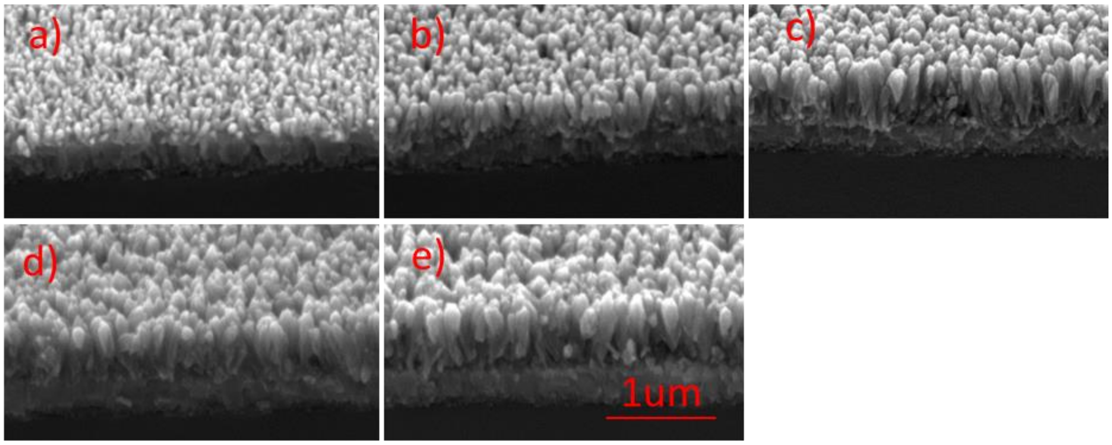

Figure 6: Fixed residence time at 0.64 min, different flow rate from (a) to (e) at 1.28 mL/min, 2.57 mL/min, 3.85 mL/min, 5.14 mL/min, and 6.42 mL/min

Film growth under different flow rate and different residence time

Figure 7 has shown the combined effect of the flow rate and the residence time. The experiment was conducted under different flow rate and residence time achieved by varying the flow rate but keeping the same tubing length throughout the experiment. Different flow rate at 2.57 mL/min, 3.85 mL/min, 5.14 mL/min, 6.42 mL/min, 7.70mL/min, and 8.99mL/min was chosen with corresponding residence time at 0.6 min, 0.4 min, 0.3 min, 0.24 min, 0.2 min, and 0.17 min. Both increase of the flow rate and reduce of the residence time can lead to an enhancement of the growth rate, which can also be observed from the measured thickness of the film from Figure 7.

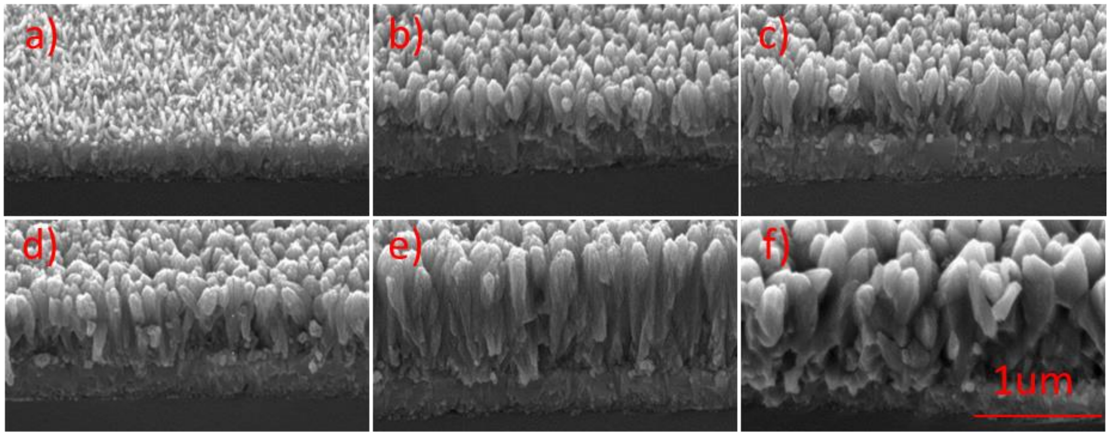

Figure 7: Growth of the ZnO nanorod at increased flow rate from (a) to (f) at 2.57 mL/min, 3.85 mL/min, 5.14 mL/min, 6.42 mL/min, 7.70mL/min, and 8.99mL/min

2.4.3 Film growth under different temperature

According to the SEM result shown above, it can be concluded that increasing the flow rate will increase the growth rate. The main reason is that a faster flow rate will enhance the mass transport in the reactors, and the side reaction is also inhibited due to the reduced residence time. On the other hand, the fluid flow in the tubing and PDMS channel will also influence the heat transfer. Herein, the growth of the film under different heating condition is also studied together with the flow rate. The silicon wafer is used as the substrate to study the growth kinetics. Stylus profiler is used for measuring the thickness by moving the stylus across the middle of the patterned ZnO thin film as shown in Figure 8. The average thickness of the profiler is used for comparison among different experimental parameters.

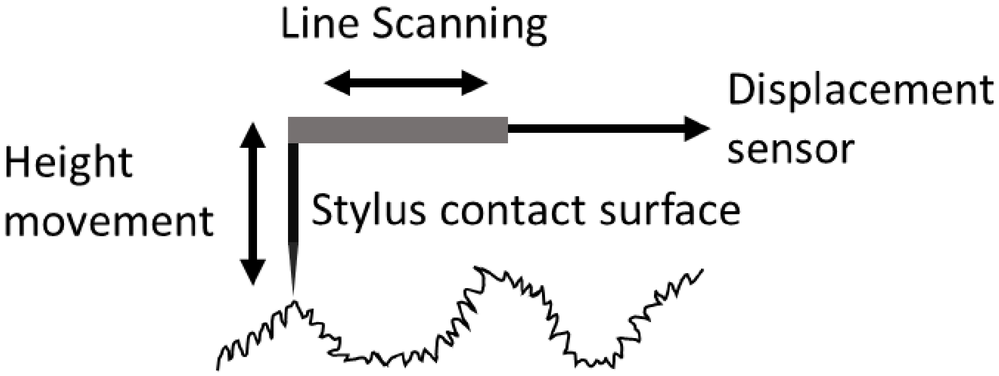

Figure 8: Schematic illustration of the stylus profiler measurement

Simulation result for the temperature (T-2) in zone-2

Our target is to estimate the growth rate at different growth temperatures while keep the same concentration supplied to the substrate surface. The microreactor was used to preheat the solution and premix the precursor solution to form the $Zn(OH)_2$ before entering channel. However, some homogeneous reaction can also occur in the microreactor, reducing the amount of the reactants in the solution. To address this problem, our strategy is to increase the flow rate so that the residence time in the microreactor is decreased and the homogeneous reaction can be inhibited, as discussed above. However, simply increasing the flow rate can cause the reduce of the solution temperature. To maintain a similar temperature leaving the microreactor, a COMSOL simulation was applied to adjust the microreactor bath temperature. In addition, two different length of the tubing at 45 cm and 100 cm were selected to control the residence time in the microreactor. Figure 9 has shown the simulated results of the temperatures required in the bath to achieve same temperatures of the solution leaving zone-2 at the different flow rate. With increased flow rate, a higher bath temperature is required to heat up the precursor solution. And an increased tubing length can reduce the bath temperature required to heat up the solution.

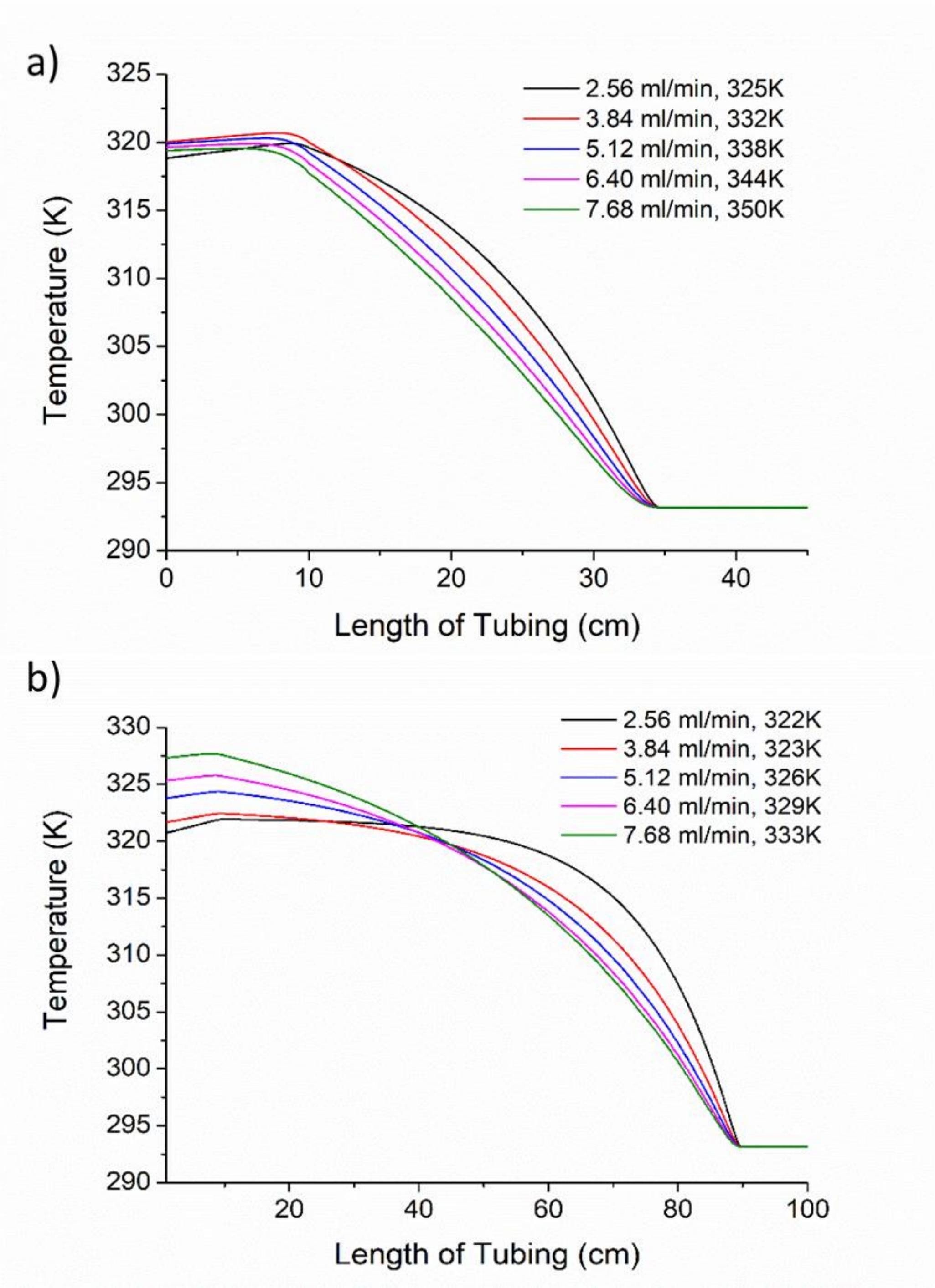

Figure 9: Simulated temperature distribution in the tubing with different length: a) 45 cm; b) 100 cm

The film growth with different time

To estimate the growth rate, we performed the experiments to grow the ZnO thin film under different running time at 5 min, 10 min, 15 min, and 20 min. The length of the tubing in the bath is 45 cm, the flow rate of the mixed solution was fixed at 3.84 mL/min. Both the heating pad and the bath temperature were kept at 333 K. Figure 10 (a) has shown the scanning data for the ZnO thin film at different running time, and Figure 10 (b) is the averaged data from the profiler measurement. From the Figure 10, it is clear the growth of ZnO nanorod has a linear relation with the deposition time, resulting in a growth rate of 37.2 nm /min. The reaction to form the ZnO nanorod was under steady state due to the continuous flow in the PDMS channel, resulting in a constant concentration of the $Zn(OH)_2$. In addition, it has been proposed from the literature that the reaction to form the ZnO nanorod from $Zn(OH)_2$ is first-order reaction.[6,59] Because of the first-order reaction kinetic behavior of the ZnO nanorod and the constant amount of the reactants, a linear growth of the ZnO thin film with time is expected. Therefore, for the ease of the calculation, all the growth rate of the ZnO was estimated by dividing the measured thickness by the running time, which was fixed at 5 min in the rest part of the paper.

In addition, the profiler result indicates that the growth rate of the film fabricated by this process has a higher rate comparing to other solution based process, where the ZnO nanorod reached a similar thickness in hours.[42,60] As in most of the bath reactor, the reactants were consumed during the deposition process and the reaction rate was reduced. But in our process, the reactants were constantly supplied to the substrate surface, which enables a fast growth of the film.

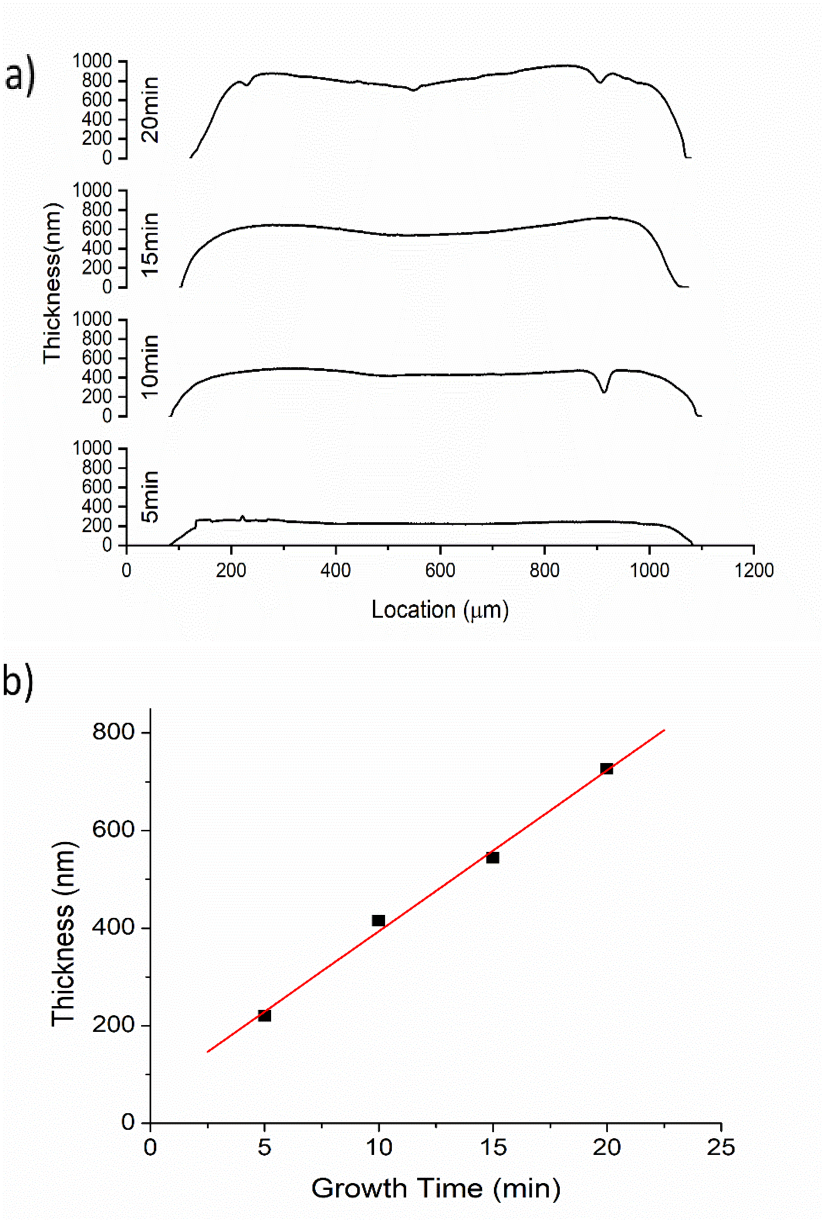

Figure 10: The thickness of the ZnO thin film at the center of the pattern: (a) scanning data by stylus profiler, (b) the average data from the scanning

Film thickness vs tubing length in Zone-2

The experiment was then conducted at different flow rate and bath temperature but the same outlet temperature when deposited on the substrate surface. Figure 11 has shown the film deposited with an increased flow rate and the bath temperature with different tubing lengths: (a) 45 cm of the tubing length and (b) 100 cm tubing length. One significant trend from the result is that the thickness is increasing as the flow rate increased. The increase the of the thickness is mainly caused by two factors: the first factor is that the increase of the flow rate can enhance the transport of the reactants to the substrate surface, resulting in a higher concentration of the reactants on the surface and a faster reaction rate; the second factor is the faster flow rate can reduce the residence time in the microreactor so that less reactants can be consumed in the microreactor. The other trend is that the ZnO film deposited from 45 cm length of the tubing is thicker than from 100 cm length of tubing, which is also an evidence for the homogeneous reaction occurred in the microreactor. But with the flow rate further increased, no significant difference of the thickness can be observed, and the thickness of the film tends to reach a steady state where the growth rate is not influenced much by the flow rate, indicating that the homogeneous reaction in the microreactor is strongly controlled, and the reactants concentrations are similar among the high flow rate, namely at 6.4 ml/min and 7.68 ml/min.

According to the discussion above, the flow rate for the growth of the ZnO film is controlled at 6.4 ml/min, the length of the tubing is 45 cm, and bath temperature at 344

K, which will result in a same temperature at 320 K and a same concentration of the $Zn(OH)_2$ precursor of 2.5 mM entering the PDMS channel.

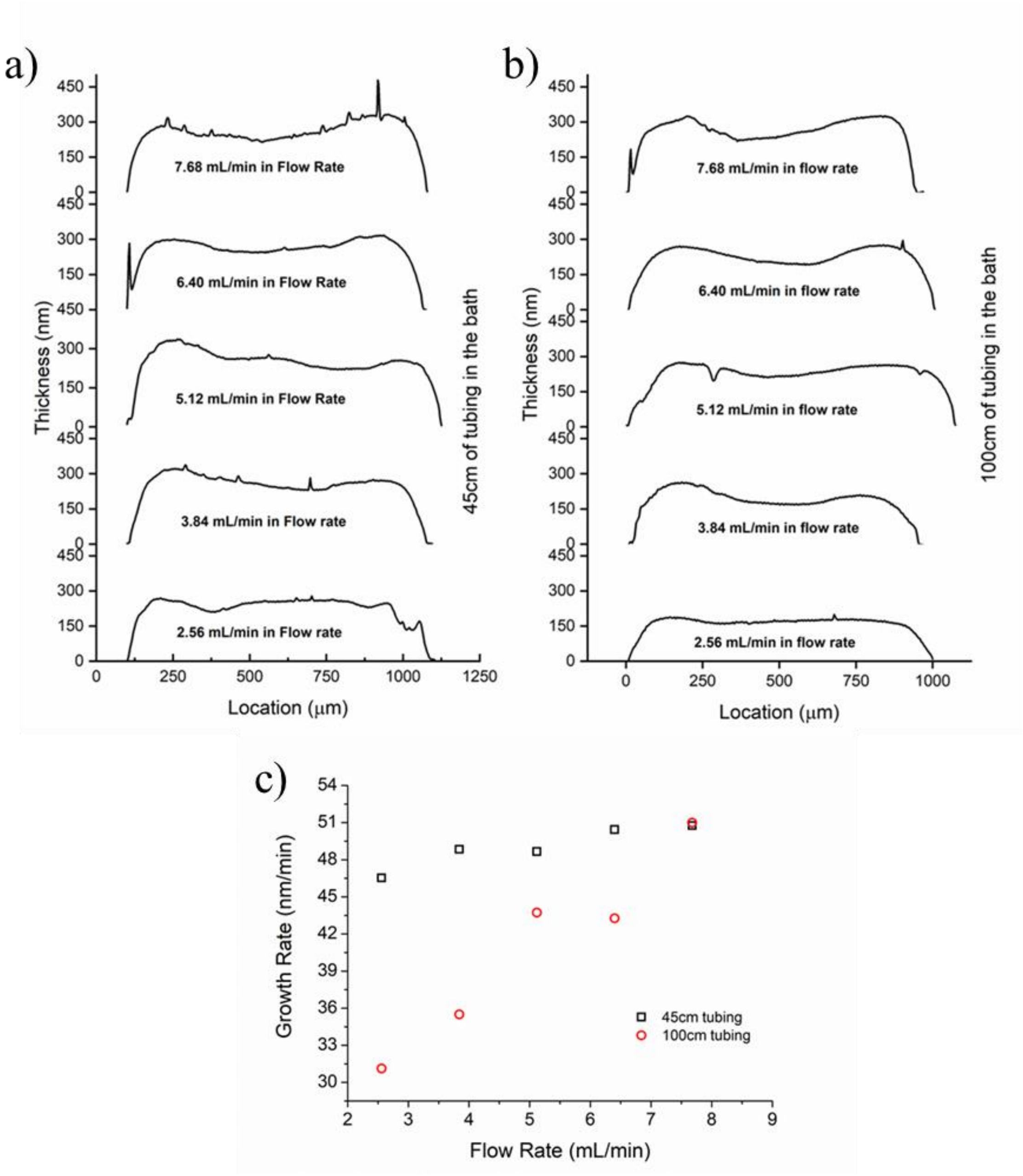

Figure 11: ZnO grown at different flow rate, bath temperature and tubing length a) 45 cm tubing length, b) 100 cm tubing length and c) the comparison of the thickness at different tubing length.

Film growth vs different growth temperature in Zone-3

As the composition of the solution entering the channel is fixed, the only parameter we controlled is the temperature under the silicon substrate. Figure 12 has shown the measured thickness of the thin film deposited at various temperatures (T3), including 333 K, 353 K, 373 K, and 393 K. A lower temperature than the heating pad is expected as the precursor solution flows through the channel. In this way, COMSOL simulation is used to simulate the surface temperature. The surface temperature at the center is presented on Figure 12(d). The growth rate of the ZnO thin film is increasing with the temperature, as the reaction rate constant is increased. The growth rate of the ZnO thin film is a first-order reaction kinetics, the thickness of the film is correlated with the $Zn(OH)_2$ concentration:

$$r = \frac{dL}{dt} = kC_{\mathrm{Zn(OH)_2}} \Rightarrow k = \frac{r}{C_{\mathrm{Zn(OH)_2}}} \tag{2.1}$$

The reaction rate can be obtained from the experimental data by measuring the film thickness and the growth time, and since the homogeneous reaction in the microreactor is neglected due to the short residence time, the reaction rate constant can also be determined. Figure 12 (c) presents the variation of the film thickness as a function of the average surface temperature. The apparent activation energy (E_a) corresponding to the film growth can also be obtained by plotting the ln(k) as a function of 1/T from the Arrhenius equation. The apparent activation energy was estimated around 22.65 kJ/mol.

$$k = A\exp\left(-\frac{E_a}{RT}\right) \tag{2.2}$$

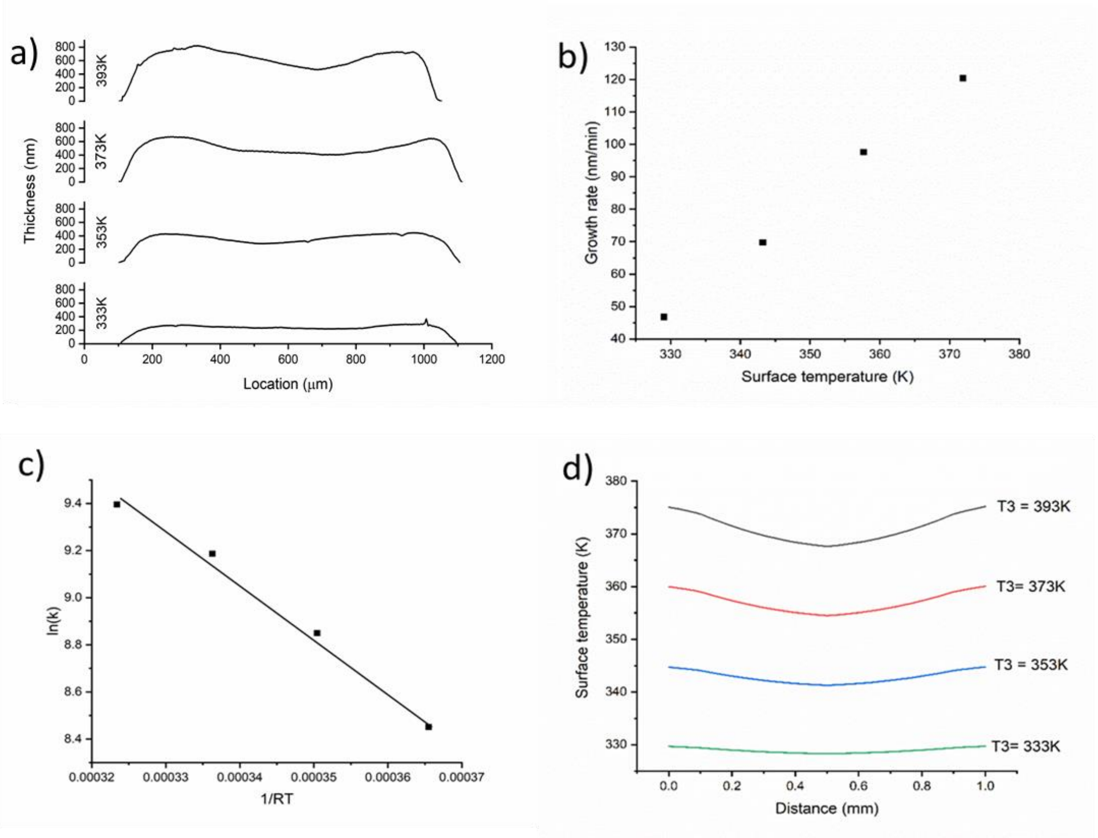

Figure 12: Kinetics of the ZnO growth: a) thickness of the ZnO grown under different substrate temperature, b) growth rate at different substrate temperature, c) the Arrhenius form the growth rate constant, d) the surface temperature simulated by COMSOL under different T3.

ZnO film measured by SEM

Figure 13 (a)~(e) have shown the SEM cross-section of the patterned ZnO nanostructured thin films fabricated by using a substrate temperature at 353 K in zone-3 (T3), at flow rate of 6.4ml/min, and 45cm length of the tubing in zone-2 with a bath temperature of 343 K (T2). The SEM images from (a) to (e) are taken from the spot from left to right, as marked in Figure 13 (f). Figure 13 (g) shows the top view of the deposited film and Figure 13 (h) is the EDS result of the film. The ZnO nanostructures fabricated by this process shows a more dense and larger size of the nanorods, comparing to the literature.[25,48,61] The ratio between zinc atoms and the oxygen atoms is about 1.3 to 1, indicating an oxygen vacancy of the film which has been reported by other researchers.[62,63]

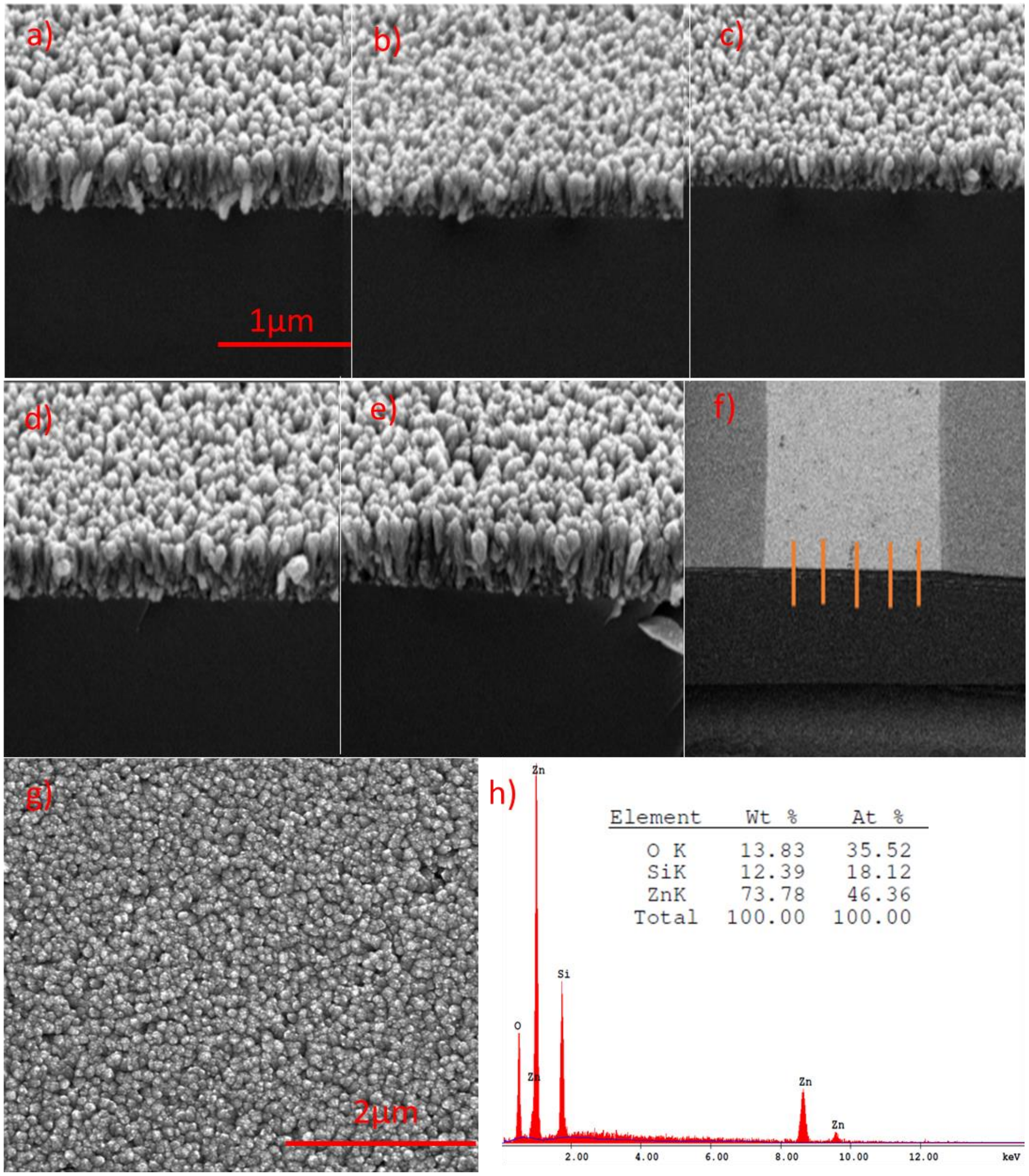

Element	Wt %	At %
O K	13.83	35.52
SiK	12.39	18.12
ZnK	73.78	46.36
Total	100.00	100.00

Figure 13: SEM images of the ZnO nanorod film grown on silicon wafer (a) tilted cross-section of the ZnO film; (b) the top view of the film; (c) the EDS of the selected film; (d) the Profiler scan data

Study of the peaks at the edge

It is found that the film close to the wall is thicker than in the center. COMSOL simulations are carried out to provide insights into the cause for this interesting result.

The simulation is studied by flowing a cooler solution along the channel than the heated wall, as illustrated in Figure 14 (a). The heat transfer data and the flow distribution data are taken from a plane 0.1 mm above the substrate surface. It has shown in Figure 14 (c) and (d) that the temperature in the center of the channel is lower than the temperature near the wall. In addition, as the solution flow along the channel, the solution is heated up and the difference of the temperatures between edge and the center is reduced.

When the precursor solution from zone-2 entered the channels, the temperature of the solution, T2, is lower than the substrate surface, T3. In this way, the surface was cooled down by the flow of the solution. However, the substrate area is much larger than the channel, the heat will be transferred to the patterned channels from the side, resulting in a higher temperature on the edges. This can also be evidenced by the film growth from the Figure 14 (e). At the film growth close to the entrance (line 1 and line 2), as the difference of the film thickness is larger when the gap between the substrate temperature and the inflow solution temperature is larger. While the solution is leaving the channel (line 5 and line 6), the temperature difference between the solution and the substrate is reduced and the thickness along the radical direction is also more even.

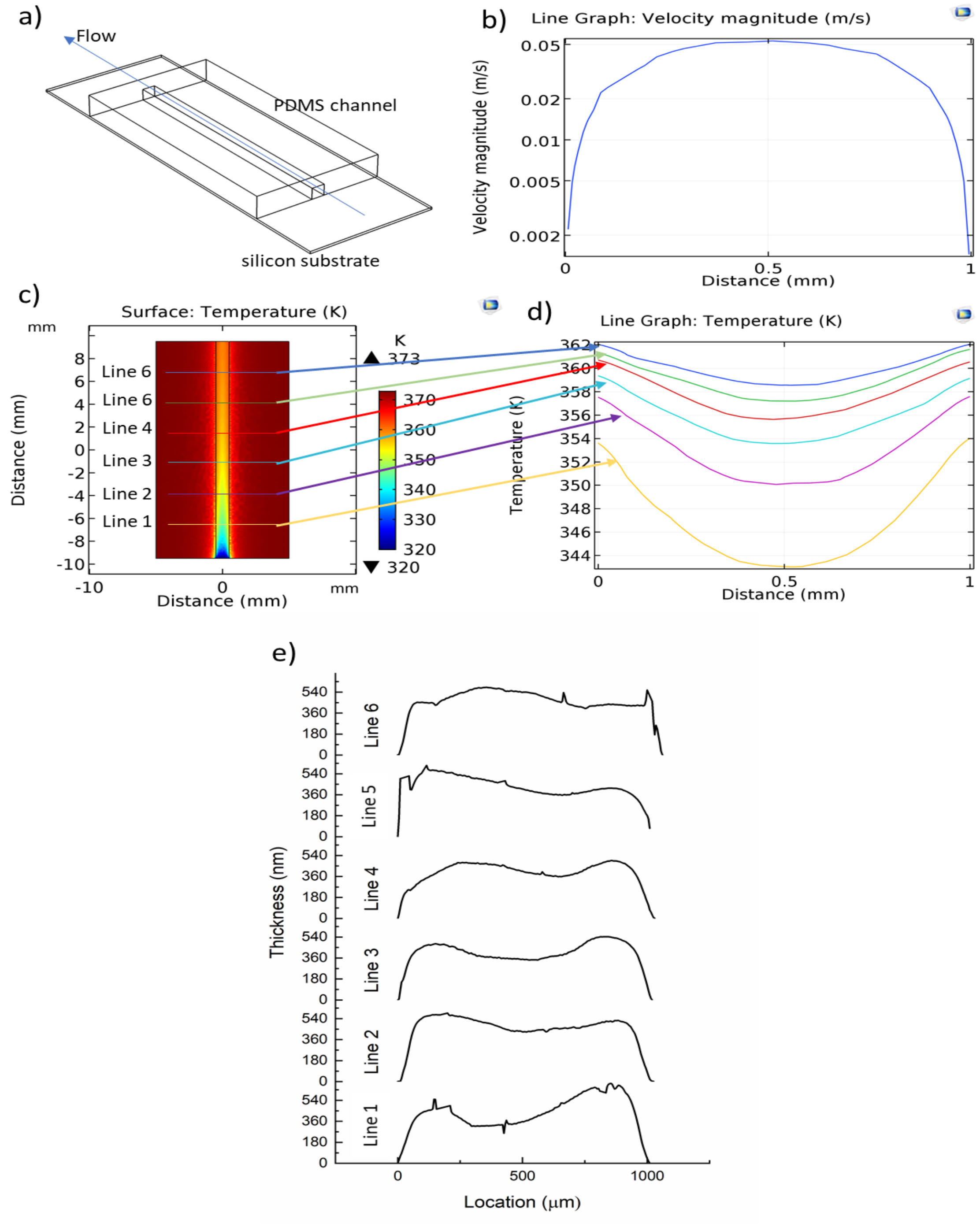

Figure 14: (a) schematic diagram of the COMSOL simulation geometry; (b) the flow velocity profile close to the substrate; (c) the temperature distribution of the surface close to the substrate; (d) the temperatures of the solution from the cutline along the radical direction at the different spots along the flow direction; (e) the profiler scan at the similar spots as the cutline temperature.

2.5 Conclusion

In this work, patterned ZnO nanostructures are deposited onto a substrate surface by a Microreactor-Assisted Nanomaterial Synthesis and printing process. The process uses a continuous flow microreactor to control and generate a reactive chemical flux that was transporting to a patterned microfluidic channel. The process contains three zones, a mixing zone, a reactant generation zone, and a deposition zone. This process allows a separation of the homogeneous reaction in the solution and the heterogeneous reaction on the substrate surface, resulting in a well-controlled growth of the ZnO nanostructures on the substrate surface so that the growth mechanisms and kinetics can be studied. Different growth parameters, including flow rate, residence time, the temperature of the chemical solution and temperature of the substrate, are varied to study the growth kinetics. A key process parameter is the flow rate. In general, a higher flow rate can result in faster growth of ZnO nanostructures. A lower flow rate will result in a longer residence time of the chemical solution within zone 2, which can lead to the homogenous formation of solid nanoparticles, thus reduce the concentration of reactive $Zn(OH)_2$ (aq). This finding is further supported by growth experiments carried out using reactors with two different reaction channel lengths within zone 2. Besides, the thickness of rectangular patterned ZnO nanostructured films show a saddle-shaped profile, which is thinner near the center. This thickness profile is a result of combined heat and mass transfer of the reactive solution within the patterned channel, as qualitatively supported by COMSOL simulations. By measuring the growth rates as a function of substrate temperatures, the activation energy of the rate constant is obtained at 22.65kJ/mol. This process not only provides better control to fabricate patterned metal oxide nanostructures but also offers the unique capability to study the growth mechanisms.

CHAPTER 3 PATTERNED ZNO THIN FILM PART I. NOVEL, SCALABLE APPROACH TO FABRICATE ZNO NANOSTRUCTURES WITH MULTISCALE 3D GEOMETRIC SHAPES

3.1 Abstract

In this study, we demonstrated a novel, scalable process to fabricate ZnO nanostructures with multiscale 3D geometric shapes. The process uses a continuous flow microreactor to control and generate a chemical reactive flux that was transporting to a patterned microfluidic channel. In particular, the precursor solutions were firstly mixed and heated in a microreactor to control solution temperature and to generate reactive species. The reacting solution was then delivered to the substrate surface guided by a patterned PDMS channels. ZnO nanostructures with multiscale 3D geometric shapes were formed guided by the patterned channel. It was found that geometry is controlled by the channel geometry, flow rate, and substrate temperature. This process enables fabrication of complicated nanostructures by using low-cost and facile solution-based method on the desired regions of the substrate surface. In addition, due to the continuous formation of the precursor solution with constant concentrations, the growth thin film can be well controlled and accelerated, comparing to the traditional chemical bath deposition process. This process is also capable of producing nanostructured thin film in large scale by well-designed PDMS channels.

3.2 Introduction

The fabrication of functional materials with designed multiscale structures plays an important role in many technology researches and applications, such as electronic devices, sensors, power generators, displays and functional surfaces. Duraisamy *et al.*

fabricate TiO_2 thin film memristors using electrohydrodynamic inkjet printing.[64] Kim *et al.* reported horizontally aligned ZnO nanowire transistors using chemical vapor deposition (CVD) on patterned graphene thin films.[65] Chen *et al.* reported honeycomb-patterned film porous film for glucose sensing using breath figure method.[66] Patterned organic semiconductors were commonly used for chemical and biological sensing applications.[67] Patterned silver-nanowires networks on a substrate can serve as a transparent conductive electrode for thin film heaters, light emitting diodes.[68,69] Stretchable strain sensors for human motion detection using patterned metal nanoparticle, carbon nanotube, and graphene thin films have been reported.[70–72] Mahapatra *et al.* used a hybrid hydrophobic and hydrophilic surface to enhance the heat transfer via a dropwise condensation.[73] Takamatsu *et al.* fabricated a stretchable keyboard based on capacitance sensors made of PEDOT: PSS electrodes patterned on a knitted textile.[74] Seung *et al.* reported a flexible, foldable nanopatterned wearable triboelectric nanogenerator based on a silver-coated textile and polydimethylsiloxane (PDMS) on ZnO nanorod arrays.[75] Significant progress has been made in understanding the biological micro- and nanostructures and many of these complex structures have been successfully mimicked. For example, biomimetic photonic structures have been applied to create brilliant structural colors without the use of pigments were also been reported.[76]

Numerous methods and processes have been developed to fabricate patterned thin film with different materials, including inkjet printing techniques[64], soft lithography[77,78], directly laser patterning[79], and photolithography.[80–82] Fabrication of micro- and nano-structures with lithographic methods such as using focused ion beam to replicate the

Morpho lamellar structure and its blue coloration has been reported.[83] Avoiding the complex manufacturing procedure using electron beam lithography, Zyla *et al.* demonstrated the use of two-photon polymerization as a more flexible lithographic fabrication process to generate arbitrary 3D structures.[84] Despite of these technological breakthroughs, the large-scale manufacturing of complex micro- and nanostructures is still a major challenge. Hong *et al.* reported a digital direct writing method to fabricate micro-patterned on a large scale by selective laser decomposition of Zinc acetate precursors to produce patterned ZnO seed layer, large scale ZnO NWs were synthesized for 5 hours, and 10,000 UV detectors were built on a 4 cm × 4 cm glass substrate.[85]

Among various patterning methods, soft lithography is a relatively simple and low-cost process, where a PDMS stamp with designed patterns is fabricated and is used to print, mold and emboss the nanostructures.[52] In this study, the same method as the soft lithography in chapter 2 was adopted to fabricate a patterned PDMS microchannel, but instead of partially transferring thin film from one surface to another, the patterned microchannel was used as a patterning conduit to supply the reactive chemical flux to the patterned substrate surface.

The overall process to deposit the patterned nanostructure thin film is illustrated in Figure 15 (a), where the whole system contains two major parts: (i) the microreactor system that forms the reactive chemical flux with tailored compositions by adjusting the flow rate and temperature and (ii) the patterned PDMS microchannel where the reactive chemical solution from the part 1 was transported to the activated reaction zone between the PDMS microchannel and the substrate surface. After the reactive chemical flux flow through the channels, a surface reaction occurs on the substrate, forming a patterned 3D multi-scale nanostructure. Several materials, including ZnO,[45] CdS,[16] and CuS[17] and Ag[15] have been fabricated by using continuous flow microreactor. ZnO is an important semiconductor material that have found applications in the areas such as cosmetics, photocatalysis, sensors, solar cells, transistors, and piezoelectric transducers. ZnO can form various different nanostructures using solution-based methods[39,80,86]. Here, we demonstrate a process to fabricate various ZnO nanostructures with multiscale 3D geometric shapes by varying the microchannel geometry and flow conditions. This novel approach offers a scalable, fast, and low-cost method to fabricate multiscale nanostructures with tailored 3D geometric shapes.

3.3 Experimental

3.3.1 Setup for the microreactor-assisted nanomaterial synthesis and the printing process and its characterization method

The overall ZnO thin film growth setup was illustrated on Figure 15. The setup contains three zones, a mixing zone, a reactant generation zone, and a deposition zone. The recipe is similar to the one reported in the literature[51]: 0.2195 g of $Zn(CH_3COO)_2{\cdot}2H_2O$ and 0.1925 g of ammonium acetate (CH_3COONH_4, Mallinckrodt Chemicals) dissolved in 200 ml of deionized water to form solution A and 0.8 g of NaOH dissolved in 200 ml of deionized water to form solution B. The two solutions, solution A and B, were pumped into two PVC tubing separately and then mixed through a mirco-T-mixer. The chemical mixture was then passed through a helical structured reactor made by wrapping a PVC tubing with 1/16 inch in inner diameter around a cylinder. The length of the PVC tubing was varied during the process in order to control the residence time and the solution temperature. The temperature of the reactor was controlled by immersing the PVC tubing in a water bath, sitting on a temperature-controlled hot plate.

The precursors for the growth of ZnO nanorods, formed in the zone-2 microreactor, were then supplied to the zone-3 microchannel for the growth of patterned ZnO nanorods on the substrate. The microchannel was sandwiched between the substrate and a polycarbonate holder to act as both a fluidic channel and a patterning tool. Different patterns will be coated on the substrate, depending on the channel geometry used.

Before the growth of the ZnO thin film, a ZnO seed layer was firstly formed on the silicon substrate surface by spin coating a 0.025 M of zinc acetate ($Zn(CH_3COO)_2 \cdot 2H_2O$, Sigma Aldrich) in ethanol solution followed by annealing at 250 °C in the air for 1 hr. The main purpose for this seed layer is to provide a nucleation sites for the growth of ZnO nanorods.

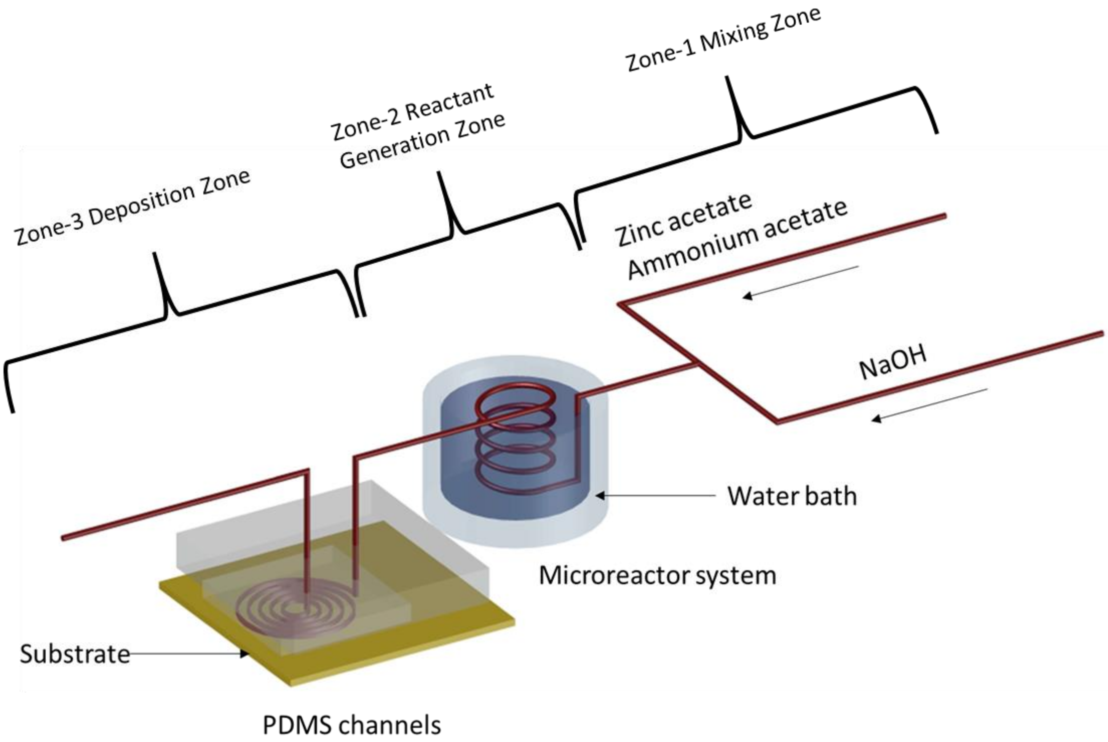

Figure 15: Setup for the microreactor-assisted nanomaterial synthesis and the printing process for the patterned film

3.3.2 Procedures to make the PDMS channel

The procedures to fabricate the PDMS fluidic channel is same as described in Chapter 2, the only difference is the pattern on the mask is different, so that the different channel shapes can be created. To fabricate the PDMS fluidic channel, an SU-8 master was firstly created on a silicon wafer. A PLA plastic framework was firstly glued on the wafer edges. This framework mainly worked as a block to prevent the movement of the uncured SU-8. The SU-8 2010 (Micro Chem) was poured onto silicon wafer in the area surrounded by the framework. The SU-8 was under soft bake at 60 °C for 12 hr, and then the SU-8 was exposed UV light with a patterned mask covered on the top. The SU-8 under exposure of UV light was cured and hardened. After curing, the SU-8 was moved to oven under 60 °C for hard bake for 1 hr. The SU-8 developer (Micro Chem) was used to remove uncured SU-8.

PDMS (Sylgard, 184, Dow Corning) and PDMS curing agent (Dow Corning) were mixed in a ratio of 9 to 1. After degasification for 1 hour, the mixture was poured onto the SU-8 master under 80 °C for 15 min, where liquid PDMS turned into elastic solid. The channel was left on the PDMS after removed from the wafer.

3.4 Results and Discussions for different Types of Patterns

Optical images were taken to show the ZnO thin film with different patterns on the silicon substrate. To further understand the growth kinetic, the stylus profiler (Dektak 8) was used to measure the thickness of the film at different spots. The COMSOL simulation was also employed to understand how the flow rate and growth temperature will influence the growth of the film. Three different types of the patterns, including the spiral patterns, parallel lines patterns, and the pattern with the symmetry lines are studied separately to understand the growth mechanisms of the thin film.

3.4.1 The Spiral Patterns

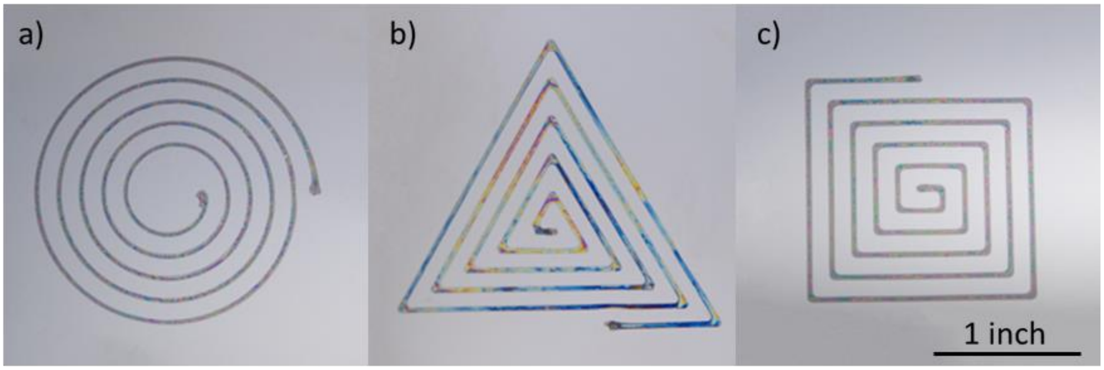

Figure 16: Optical images of the spiral patterns: a) circles pattern, b) triangles pattern, and c) squares pattern

Figure 16 has shown the ZnO film fabricated by the process. Three different patterns, including the spiral patterns of (a) circles, (b) triangles, and (c) squares. The ZnO patterns were fabricated by flowing the precursor solution directly through a continuous PDMS channel from the inlet to the outlet, leaving a film with different curvatures. The width of the line is about 0.0394 inch (1mm). To further characterize the film, a stylus profiler was used to estimate the thickness of the film at different spot, as shown in Figure 17. The spiral circles pattern is used as the example for stylus scan. The inserted figure indicates the scan directions. From the profiler scan, it has shown that the line on the left most has the highest thickness, which is corresponding to the line from the inlet. The possible explain is that the precursor solution entering the channel has the highest concentration. While flowing through the channel, reactants were consumed either on the substrate surface or in the solution phase, resulting in a reduced concentration and growth rate of the ZnO film. Besides, it can also be observed that the film close to the outlet has the lowest thickness.

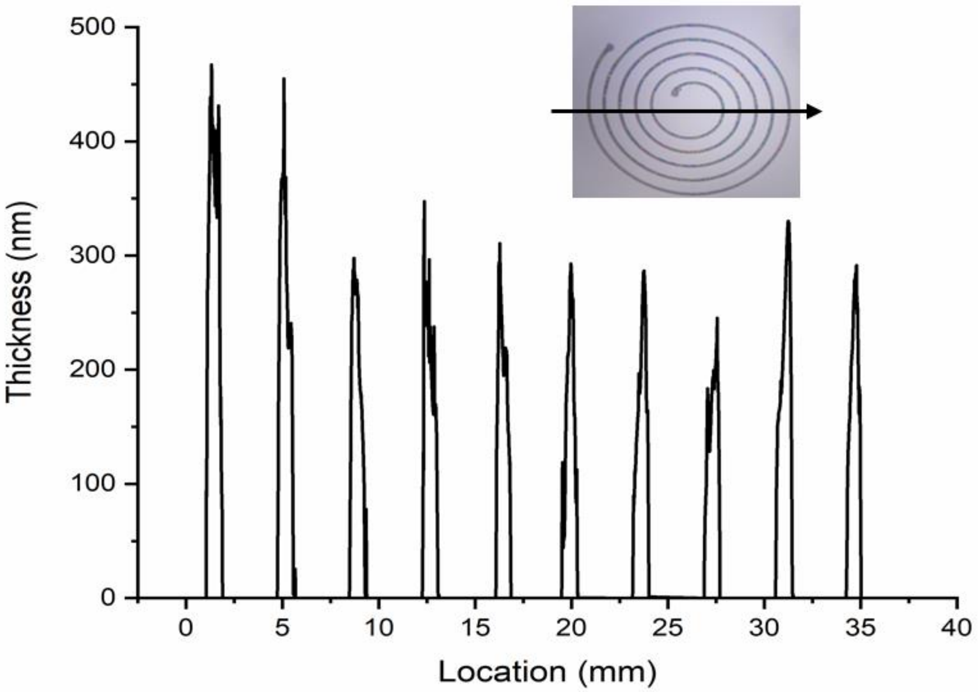

Figure 17: Thickness scanned by stylus profiler of the spiral circles, and the scan path

To further study the kinetics of the flow reactants in the channel, a COMSOL simulation is applied to study the heat transfer and the fluid flow of the process. In the COMSOL simulation, the spiral circles with the same shape as the PDMS channel was used as the model. From the COMSOL simulation in Figure 18 (a), it can be found that the velocity of the film is uniformly distributed along the flow direction. The velocity profile along the cutline through the center of the channel also shows that not much change of the velocity along the flow direction, as shown in Figure 18 (c). However, in Figure 18 (b), it has shown a gradually increased temperature of the fluid along the flow direction. The solution entering the PDMS channel has a lower temperature around 323 K, while the heating temperature for the silicon substrate was fixed at 333 K. The solution will eventually be heated to 333 K as it flowed through the channel.

The variance of the temperature of the solution along the flow direction will cause the different growth rate at different spot. In this way, the growth rate of the film is determined by the temperature of solution and the local concentration of the reactants.

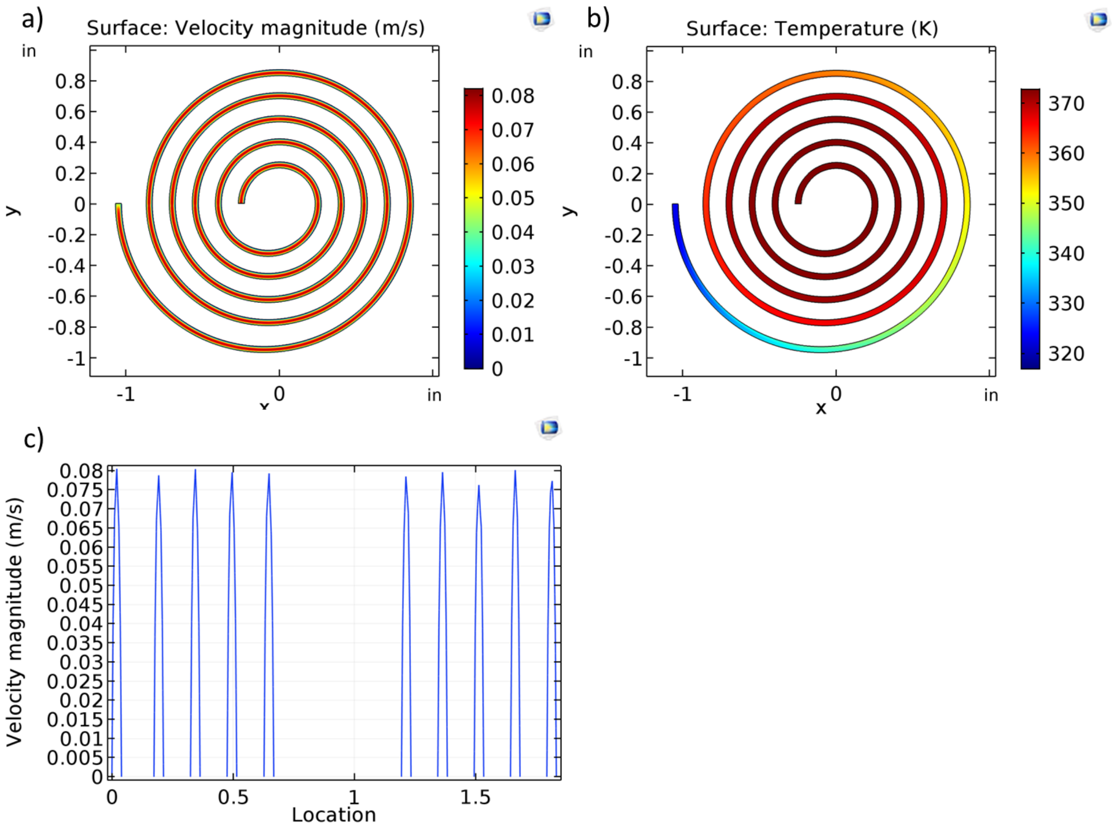

Figure 18: COMSOL simulation result: a) the surface velocity, b) the surface temperature, c) the velocity profile at the cutline

3.4.2 Parallel lines

ZnO patterns with parallel lines have also been fabricated by using the appropriate PDMS channels where the precursor solution firstly entered a triangle area followed by splitting to different individual channels. Those channels can be designed with different widths and different distances between each other. After following through the individual channels, the solution merged together and left the PDMS mold, leaving patterns on the silicon substrate surface, as shown in figure 19: a) the lines have the same width at 0.0394 inch, b) different line width at 0.0157, 0.0276, 0.0394, 0.0512, 0.0634 inch, from left to right. Thus, the thin film with different size can be fabricated simultaneously by simply using a channel with one inlet and one outlet, which enables the scale up of the nanostructured thin film.

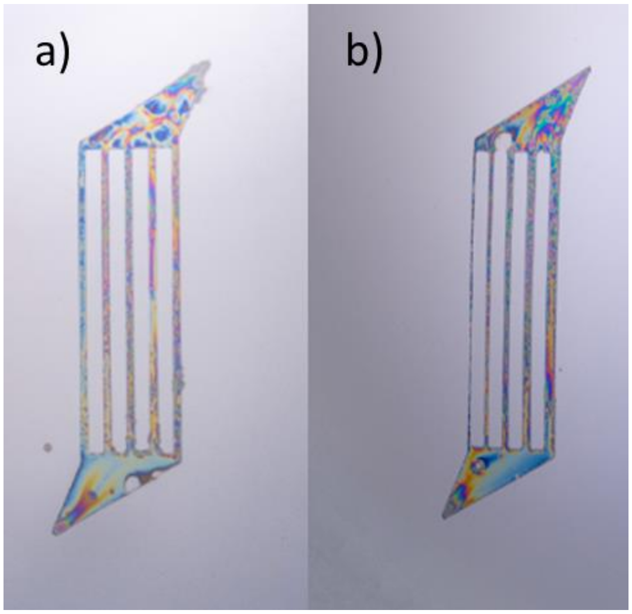

Figure 19: Optical images of the parallel patterns

The thickness of the film was measured again by the profiler, as shown in Figure 20. The scan for the film thickness for both patterns was from left to right, and across the center of the lines, as described in the inserted figures. Figure 20 (a) shows the thickness of the parallel patterns with the same line width, which has shown a similar thickness and width of all the five lines. The only difference is the 3rd line is slightly thicker than the other lines. While for the thickness measurement of the pattern with different width, it is clear the lines in center is thicker than the lines at the edge. Another common result of both patterns is that for each single line the film is thinner in the center than the film at the edge.

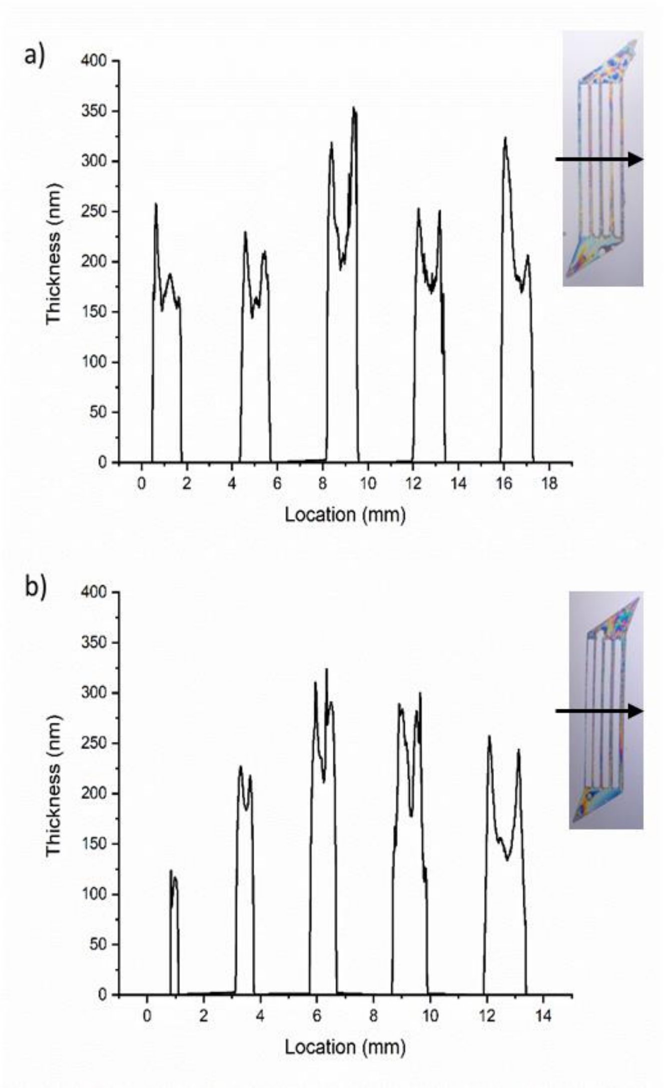

Figure 20: Thickness measured by the stylus profiler and the scan path

The COMSOL simulation was applied to understand the film growth kinetics. Figure 21 has shown the velocities of the flow in each line for both patterns. It can be found in Figure 21 that in the pattern with the same line width, the velocity is very similar in each channel. While for the pattern with different line width, the velocity is increasing as the width of the line. The difference of the velocity is caused by the difference of the pressure drop of each line due to the difference in width. As discussed before, a faster flow rate will result in a faster growth rate as more reactants are transported to the substrate surface.

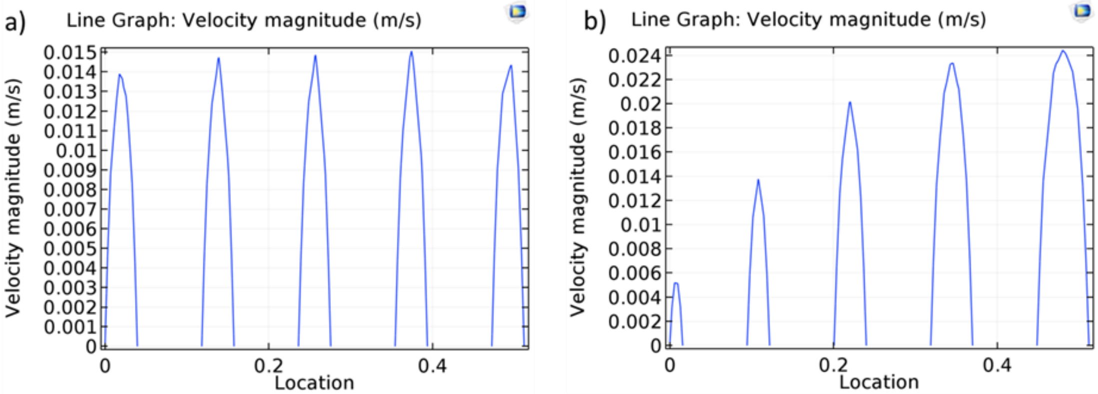

Figure 21: Velocity of the solution flow in each channel: a) the parallel channels with the same width, (b) parallel channels with different width

Another parameter that can influence the growth kinetic is the temperature. In Figure 22, the temperature distributions of both patterns are compared. For the pattern with the same width, the temperature is increasing from left to right. Because of the temperature difference along the radical direction. The right 3 lines are slightly thicker than the left 2 lines due to the temperature difference. While for the pattern with different channel width, the film deposited at the center is thicker than the other film, and the film is getting thinner toward the edge channels.

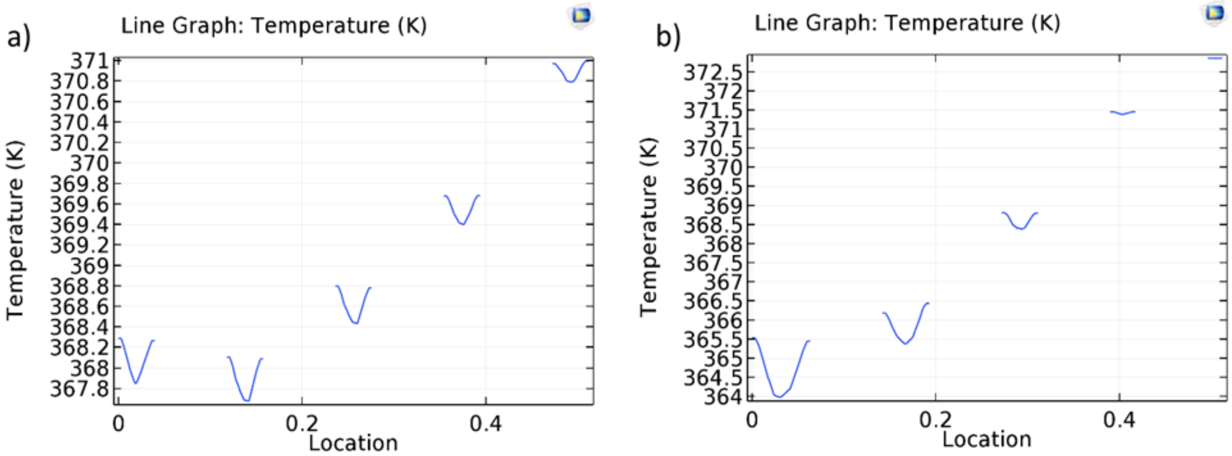

Figure 22: Temperature of the flow through the channels

3.4.3 Patterns with symmetry structure

Figure 23 has shown the pattern with the symmetry structure. The solution will firstly enter a single line channel, and then flow into the bypass channels. In this way, the solution can be distributed into different path for multiple film deposition or complicated pattern fabrication. In Figure 23, the solution was evenly split when entering the bypass channel, so that the flow rate is evenly divided while the concentration of the precursor is same along the radical direction. The solution eventually are merged before leaving the channel.

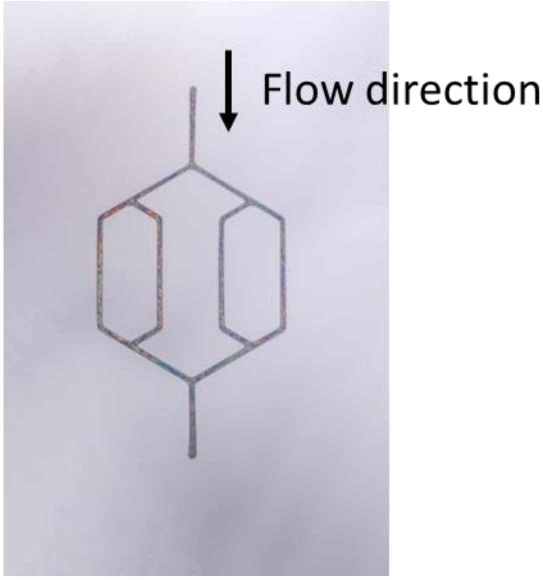

Figure 23: Optical image of the symmetry sample

Figure 24 has shown the film thickness at the different spots scanned by using the profiler. Figure 24 (b) has shown the location where the film was scanned. Each scan has been designated a name according to the scan order. It can find that whenever the fluid is split, the thickness of the film decreased, and when the fluid is merged, the thickness of the film is increased. The velocity of the fluid along the channels is shown on Figure 25 (a), where the flow rate is almost halved when split and doubled when merged. By comparing the fluid velocity profile and the thickness profile, it can be found that the change of the film thickness is caused by the flow rate. Under higher flow rate, the film is growing faster, resulting in a thicker film. The main reason for this phenomenon is that under higher flow rate, there will a faster mass transfer due to the convection by the flow. As the reactants close to the surface are consumed, more will be supplied to the surface by the fluid flow under higher flow rate. In this way, the ZnO film under higher flow rate will grow faster than the film under lower flow rate.

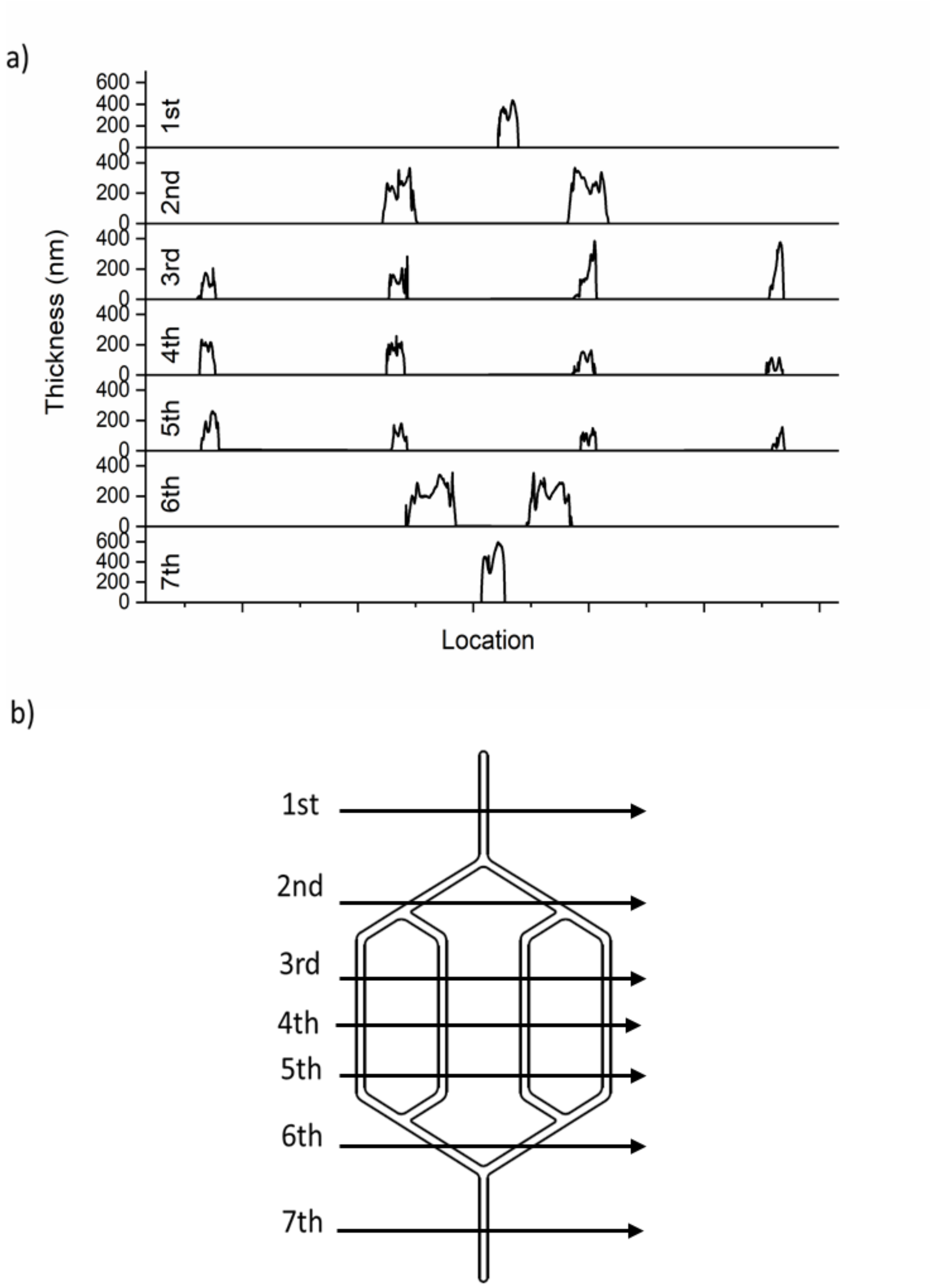

Figure 24: (a) Thickness of the film measured by profiler, (b) the scanning order and direction

On the other hand, the change of the film thickness is not very significant along the flow direction, which can be observed from the 3rd, 4th and 5th line, where the flow rates are identical. The thickness of the film is even increased at the outlet part when comparing the thickness measurement between 1st and 7th scan lines. As discussed before, the concentration of the precursor is reducing along the flowing direction. The increased thin film thickness is caused by the uneven distribution of the temperature along the substrate. The temperature distribution of the solution was shown on Figure 25 (b), where the temperature at the inlet is much lower than the outlet, since the solution from Zone-2 has a lower temperature and as it continues to flow through the channel, the heat transfer between the substrate surface and the fluid flow will reach an energy balance and the solution will be gradually heated up. The higher temperature will increase the reaction on the surface, resulting in a thicker film at the outlet.

In all, the major factors that can influence the film growth are the transport of the reactants and the reaction temperature. These findings will enable the uniformly growth of the film by designing the channels with specific width and controlling the flow rate, so that the flow rate in each channel is identical and the increased temperature can offset the effect of the reduced concentration in the fluid.

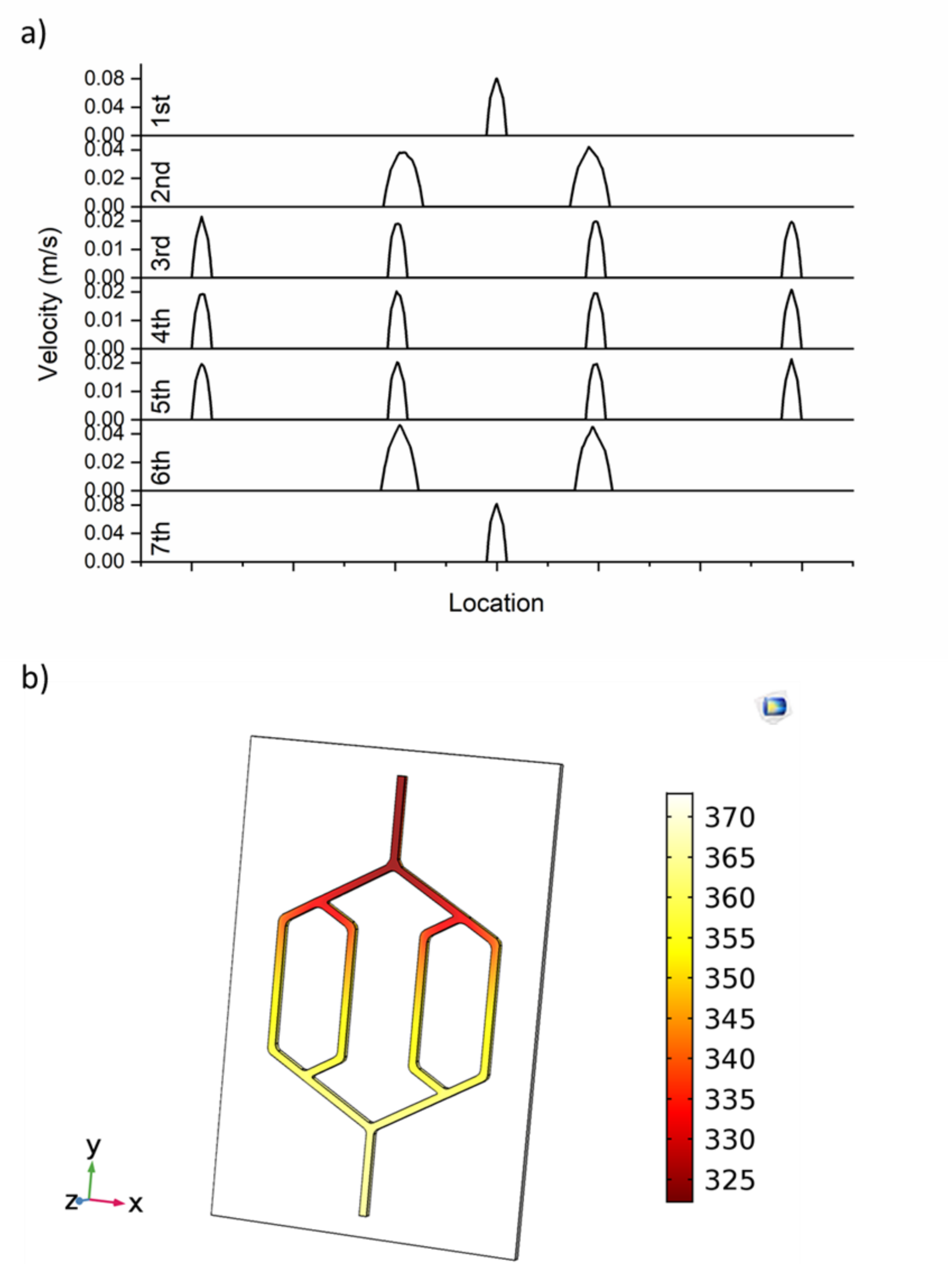

Figure 25: a) COMSOL simulation for the velocity of the fluid in the channels, b) the temperature distribution of the pattern

3.5 SEM result

Figure 26 has shown the SEM result for the symmetry pattern with different line width. The morphologies of the ZnO thin film deposited by this method is similar with line pattern in Chapter 2, with a close-packed nanorods on the silicon. This is due to the same chemical and reaction used to deposit ZnO thin film. Also, the thickness of the films measured by SEM show the same trend as the profiler, namely, thin film deposited on narrow channels such as (d) and (e) have thinner film than the others.

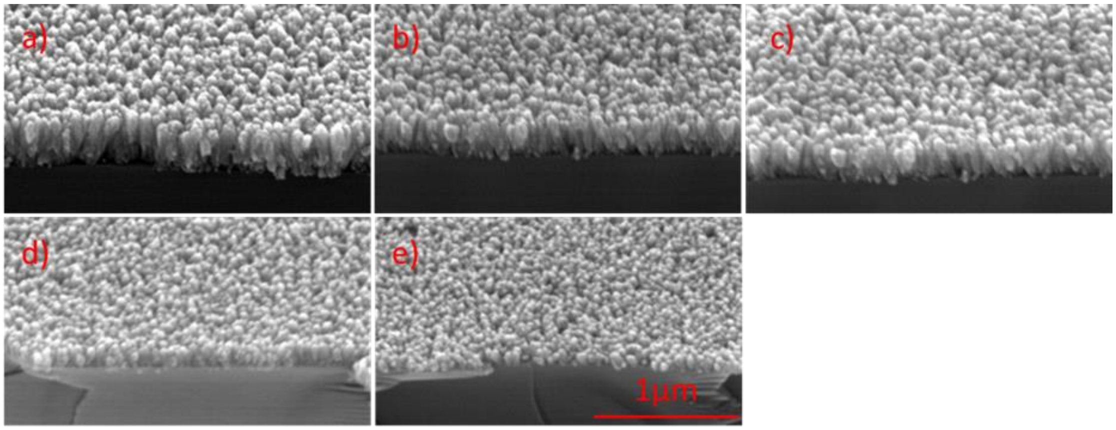

Figure 26: SEM result for the ZnO symmetry pattern with different channel width, where Figure a) to e) reparents each channel with decreased width

3.6 Conclusion of the deposition of patterned ZnO film

In this chapter, we demonstrated a novel, scalable process to fabricate ZnO nanostructures with multiscale 3D geometric shapes. The method uses a continuous flow microreactor to control and generate a reactive chemical flux that was transporting to a patterned microfluidic channel. In particular, the precursor solutions were firstly mixed and heated in a microreactor to control solution temperature and to generate reactive species. The reacting solution was then delivered to the substrate surface guided by a patterned PDMS channel with different designs, including the spiral pattern, the parallel pattern and the split-and-recombine pattern. ZnO nanostructures with multiscale 3D geometric shapes were formed guided by the patterned channel. It was found that geometry is controlled by the channel geometry, flow rate, and substrate temperature. The stylus profiler measures film thickness, and the result shows that the unique characteristics of each pattern type. With the aid of the Comsol simulation, the parameters that control the growth are studied: in the spiral pattern, the consumption of the reactant can result in a thinner film as the solution flows through the channel. In the parallel-design pattern, the film thickness is determined by the flow rate of the solution in each channel in parallel. With the channel narrowed and the flow rate reduced, a thinner ZnO nanostructured film is obtained. In the split-and-recombine design pattern, the film growth rate is halved as the channel split and doubled as the channels re-combined. The temperature profile within the channel is another critical parameter of controlling the growth of ZnO nanostructures in all dimensions. This scalable process, aided with new understandings, will provide a unique capability to fabricate metal oxide nanostructures of controlled multiscale 3D geometric shapes.

CHAPTER 3 PATTERNED ZNO THIN FILM PART II. APPLICATION OF THE PATTERNED ZNO NANOSTRUCTURE THIN FILM

3.7 Introduction of the photocatalyst

Wastewater containing organic dyes from paper, textile or other industries has received considerable attention. Due to its good stability in the nature water system, those organic dyes can lead to some critical environmental problems. For example, more than 10,000 different types of dyes and pigments are used in textile industry.[26] Several attempts have been applied to treat the wastewater and reduce the amount of the organic dyes, including chemical coagulation, physical adsorption and chemical oxidation using ozone, or H_2O_2.[87] However, the coagulated or adsorbed dyes are only transferred from one phase to another and can still act as pollution source, while the chemical oxidation will consume additional energy and generate toxic oxidants.

3.7.1 Photocatalysis mechanisms

Photocatalytic process has provided an alternative solution to remove the organic dyes from the wastewater, where the organic dyes can be eliminated by employing a semiconductor surface such as TiO_2 or ZnO under UV irradiation.[88] ZnO, as an compound semiconductor with a direct band gap of 3.37eV has been widely studied due to its good photocatalytic performance and ease to fabricate.[89–91] Photocatalytic method offers a replacement for treating the organic dyes, with a lower cost of energy, high efficiency in destruction of the organic dyes and less byproduct waste. The semiconductor used in photocatalyst process can generate highly reactive radicals to oxidize the organic dyes in the solution.[30,92,93] In a typical photocatalyst process, the photo-induced electron-hole pairs are formed on the photocatalyst material surface by promoting the valence band electrons to the conduction band under irradiation with sufficient energy, leaving holes in valence band (Eq. (2.3)).[94] Those electrons in the conduction band ($e^-_{(CB)}$) and holes in the valence band ($h^+_{(VB)}$) either undergo recombination and release heat (Eq. (2.4)) or further react with the chemicals, such as O_2 or OH^-. The holes in the valence band can react with the OH^- to for the hydroxyl group radicals (Eq. (2.5)). The holes in the valence can also convert the organic dyes to intermediate compounds directly, those intermediates are highly reactive, which permit a further oxidation process (Eq. (2.6)). In the conduction band, the electrons react with oxygen (O_2) to form the superoxide radicals (Eq. (2.7)). The superoxide radicals are protonated by the H^+ from the ionization of water, and further generate hydrogen peroxide and the hydroxyl radicals (Eq. (2.8)(2.9)(2.10)). The hydroxyl radicals generated from the photocatalyst surface are strong oxidants and are the primary cause for the mineralization of the organic dyes (Eq. (2.11)).

$$\mathrm{ZnO} + hv \rightarrow \mathrm{ZnO}\left(\left(\mathrm{e}^-\right) + \left(\mathrm{h}^+\right)\right) \tag{2.3}$$

$$\mathrm{e}^- + \mathrm{h}^+ \rightarrow heat \tag{2.4}$$

$$\mathrm{h}^+ + \mathrm{OH}^- \rightarrow \cdot\,\mathrm{OH} \tag{2.5}$$

$$\mathrm{h}^+ + dyes \rightarrow oxidation\ product \tag{2.6}$$

$$\mathrm{e}^- + \mathrm{O}_2 \rightarrow \cdot\,\mathrm{O}_2^- \tag{2.7}$$

$$\cdot\,\mathrm{O}_2^- + \mathrm{H}^+ \rightarrow \cdot\,\mathrm{OOH} \tag{2.8}$$

$$\cdot\,\mathrm{OOH} + \cdot\,\mathrm{OOH} \rightarrow \mathrm{H_2O_2} + \mathrm{O_2} \tag{2.9}$$

$$\mathrm{H_2O_2} + \cdot\,\mathrm{O_2^-} \rightarrow \cdot\,\mathrm{OH} + \mathrm{OH^-} + \mathrm{O_2} \tag{2.10}$$

$$\mathit{dyes} + \cdot\,\mathrm{OH} \rightarrow \mathit{degradation\ products} \tag{2.11}$$

3.7.2 Improvement of the ZnO photocatalytic performance

Several factors can limit the application of the photocatalytic process, for example, the charge carrier recombination can limit the number of electron-hole pairs, which will reduce the efficiency of the degradation. Also, the separation of the charge is limited by the energy of the incident light. To improve the performance of the photocatalyst, dopants or composite system are employed to the ZnO semiconductor.

As mentioned before, the efficiency of the photocatalyst is governed by the photo-induced electron-hole pairs. Doping with appropriate materials into the ZnO crystal structure can narrow the band gap and inhibit the recombination of the photo-induced electrons and holes, leading to an enhancement of the photocatalytic performance under the visible light region. ZnO has three different crystal structures: hexagonal wurtzite, cubic zincblende and rocksalt. The hexagonal wurtzite is the most thermodynamically stable structure under room temperature, where each Zn^{2+} ion is surrounded by four O^{2-} anion at the corners of a tetrahedron, and vice versa.[95] Doping with metal can substitute of Zn^{2+} ions with tetrahedral O coordination in ZnO lattice, resulting in a *n*-type doping, and doping with nonmetals can cause the vacancies of oxygen, resulting in *p*-type doping.[96]

The photocatalytic process for the dye degradation will only proceed when the incident light has a great energy than the band gap of the ZnO materials. In this way, only UV light with a wavelength less than 387 nm can be applied for the photocatalytic process. However, doping with metal ions can narrow the band gap of the ZnO, resulting in a shift of the absorption edge to the visible range. Currently, many metal ions doping have been studied, including copper, cadmium, tin, cobalt, aluminum, and iron.[97–102] Mohan *et al.* found that doping with copper can cause the surface defects, which can serve as favorable trap sites of the electrons or holes to reduce the their recombination and enhance the performance.[103] Ba-Abbad *et al.* incorporated iron ions (Fe^{3+}) into ZnO via sol-gel technique and the results indicated longer wavelength absorption in the visible light range and a red shift of the band gap.[104] In addition, Karunakaran *et al.* studied the performance of the cadmium doped ZnO and concluded that the doping will not change much of the band gap structure but reduce the grain size the ZnO structure and destroy the microstructure.[105] In this way, the photocatalytic performance can be still enhanced.

In the nonmetal doped ZnO, the oxygen atoms are substituted by nonmetals, which will shift the valence band energy of ZnO upward and narrow the band gap of the ZnO. Among those nonmetals, carbon (C), nitrogen (N), and sulfer (S) are intensely studied.[96,106] Yu *et al.* incorporated N into the ZnO crystals to form the N 2p states in band gap, which allows the improvement of the visible light absorption and enhancement of the photocatalytic activity.[106] The incorporated N atoms can both exist in the interstitial sites or interstitial sites of the ZnO lattice, but in both cases, the doped

N can improve the visible light absorption and photocatalytic activity.[107] C doped ZnO also shows an enhanced visible light absorption up to 700 nm.[108]

Coupling ZnO with other materials, such as Ag, Bi_2O_3, ZnS, MoS_2 and TiO_2 to form a composite system can also achieve an improvement of the photocatalytic activity.[109–112] In composite system, the ZnO is directly contacted with other material. The coupled materials have two different energy level, and upon irradiation, the photo induced electrons can be transferred from ZnO to the other materials, due to the difference in the conduction band, which allows the separation of the photo induced electron-hole pair and inhibits the recombination of the electron-hole pairs.[30] Ag is a promising metal to couple with ZnO to form the composite photocatalyst and has been studied extensively. The coupled Ag material mainly play two roles: one is to reduce the hole-electron recombination due to the Schottky barrier at the metal-semiconductor interface.[113] The other role of the Ag is to enhance the visible light absorption of the composite system induced by the surface plasmonic absorption from Ag.[114] It has been reported that the absorption of the composite system is higher than pure ZnO at visible range due the surface plasmonic effect.[115,116]

3.7.3 Parameters that can influence the ZnO photocatalyst

The rate of the ZnO photocatalytic performance can be influenced by many parameters, including the pH of solution, the concentration of the dyes, the shape and the load of the photocatalyst, and the light source wavelength and intensity.

pH

In the photocatalytic process, the pH is playing in an important role. Sobana et al. has studied the AR18 degradation by using ZnO photocatalyst, and its performance under different pH was compared.[117] Their results have shown that increasing pH from 3 to 11 will result in an increase of the degradation rate, which is caused by the increased formation of the hydroxyl radicals. The pH of the solution can also influence the surface charge for both of the ZnO photocatalyst and the organic dyes, where the surface is positively charge below the points of zero charge (PZC) and negatively charged above PZC. Bechambi *et al.* studied the degradation of the bisphenol A, and the optimum degradation pH is at 8, where the organic dyes and photocatalyst surface has the opposite charge, which will enhance the adsorption of the dyes on the ZnO and degradation of the dyes.[118] Both dyes and ZnO will be negatively charged by further increasing the pH above 9, resulting in a repulse between dyes and ZnO.

Concentration of the dyes

The initial concentration of the organic dyes is another parameter that influences the photodegradation. By comparing the degradation rate under different initial concentration, the photo degradation rate is reduced when increasing the concentration.[110,119] The possible reason is that the more dyes will be absorbed on the ZnO surface and less radicals can be generated. In addition, higher concentration of the dyes may also prevent the photons from reaching the ZnO surface, thus less hole-electron pairs will be generated.

Morphologies of the ZnO

The morphology of the ZnO plays a key role in the photodegradation of the organic dyes. ZnO can be synthesized with different morphologies, including nanorods, nanoprisms, flowerlike structures and nanoplates.[120,121] Those ZnO with different structures will have different sizes and shapes, which can lead to different surface area of the ZnO photocatalyst. The high surface to volume can greatly affect the photodegradation performance. Zhao *et al.* compared different ZnO nanostructures, and concluded that the ZnO with the larges surface area favored the mass transportation of the radicals and dyes and exhibited the highest photocatalyst efficiency.[122] In addition, the surface of the ZnO nanostructures can also influence the efficiency. Jang et al. has compared the ZnO nanostructure with different faces, and found that the ZnO nanoplates with a high population of polar ZnO (0001) faces achieved the highest photocatalytic efficiency.[123] Studies have also shown that the smaller size and higher crystallinity can also exhibit higher photocatalyst efficiency.[124]

3.7.4 Immobilized ZnO

To apply the ZnO for the photocatalyst, generally two method are used, the suspension system and the continuous flow system. In the suspension system, the ZnO particles are mixed with the dyes in solution under stirring and light irradiation, and the photocatalyst process occurred homogeneously in the solution.[125] In the continuous flow system, the ZnO is immobilized on a substrate surface and the fluid flow containing the dye flow through the surface. Mass transfer of the dyes and radicals can occur between the ZnO surface and the fluid to complete the degradation. Comparing the suspension system, the continuous flow system has several advantages over the suspension system, including s high surface-to-volume ratio, short diffusion distances, and rapid heat dissipation and mass transfer.[126,127] Another advantage of the continuous flow system is that it doesn't require additional process to separate and recover the photocatalyst, which ease the degradation process. Studies have shown higher efficiency of the continuous flow system than the suspension system. For example, Han et al. has grown ZnO on a glass substrate, which was further integrated into a microfluidic device and has shown a much higher photodegradation efficiency than the conventional method using dispersed ZnO NWs.[128]

3.8 Experimental

In this study, patterned ZnO thin film was coated on the quartz substrate surface by using a combination of the microreactor assisted solution deposition method to grow the ZnO thin film and the PDMS channels to create the pattern. The detailed process is same as in part I. The 3x1 inch quartz glass is used as the substrate, as the UV light can directly go through the quartz glass side to reach the ZnO film. To fit the quartz glass area, a different pattern with W shape was coated on the quartz glass. The photocatalysis experiment was conducted by flowing the methylene blue (MB) through the same shape of the PDMS channel and the coated ZnO thin film. The results of the cyclic photodegradation of the MB using the continuous flow system was systematically studied to demonstrate the kinetics and performance.

To fabric the microfluidic device for the photodegradation, the exact same PDMS pattern used to grow ZnO was covered onto the ZnO film on the quartz substrate to guide the dye flow. In this way, the dye solution can only flow through the coated part. To run the photocatalytic test, 0.03mM of the methylene blue solution in a reservoir was pumped into the microfluidic device by using a peristaltic pump (Ismatec, ISM404B), and the solution leaving the device was collected in the same reservoir, leading to a closed loop of the dye solution and continuous degradation of the dye. The device was irradiated from the quartz side by a 10W of the UV light source (UVP UVS-18 ASSEMBLY) at 245nm throughout the flow of the methylene blue. The methylene blue concentration was estimated by measuring the UV-VIS absorption of the solution taken from the reservoir by the JASCO V-670 spectrophotometer every 30min. After the measurement, the solution was immediately poured back to the reservoir to maintain the total amount of the solution. The degradation rate was estimated by peak intensity change of the absorption spectra at around 664nm. Different parameters were controlled in the experiment to estimate the kinetics of the degradation process, including the running time, flow rate, initial concentration and the total amount of the MB in the reservoir. Figure 27 has shown schematic illustration of the setup for the photodegradation test.

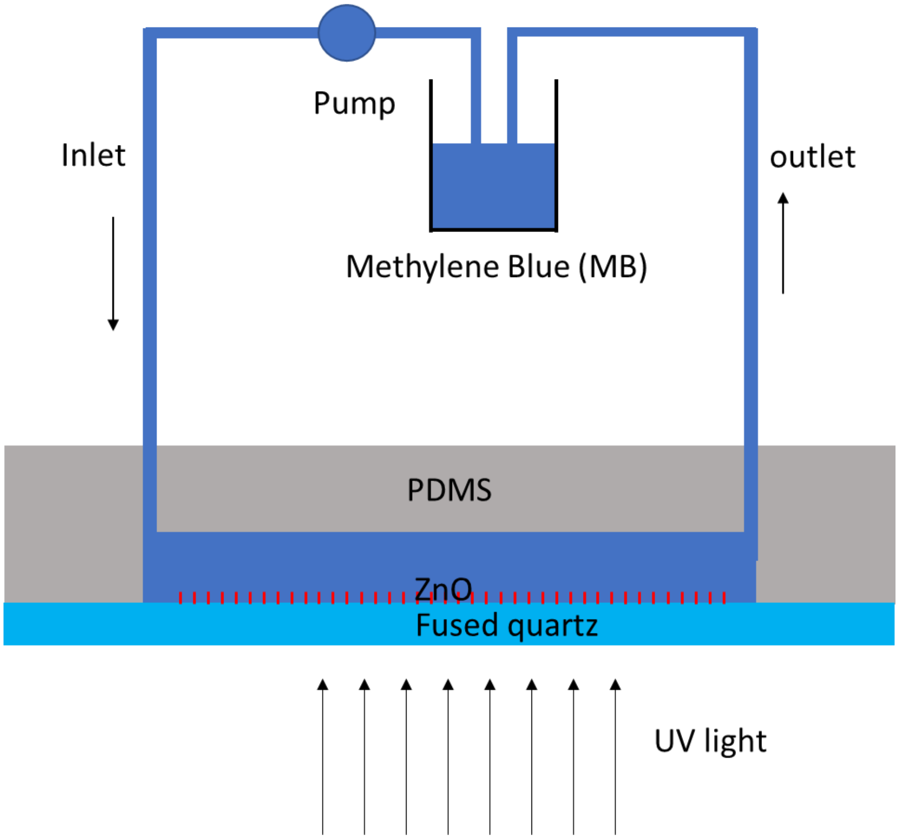

Figure 27 Schematic illustration of the setup for the photocatalysis device for photodegrade the MB

3.9 Characterization of the ZnO film on the quartz glass

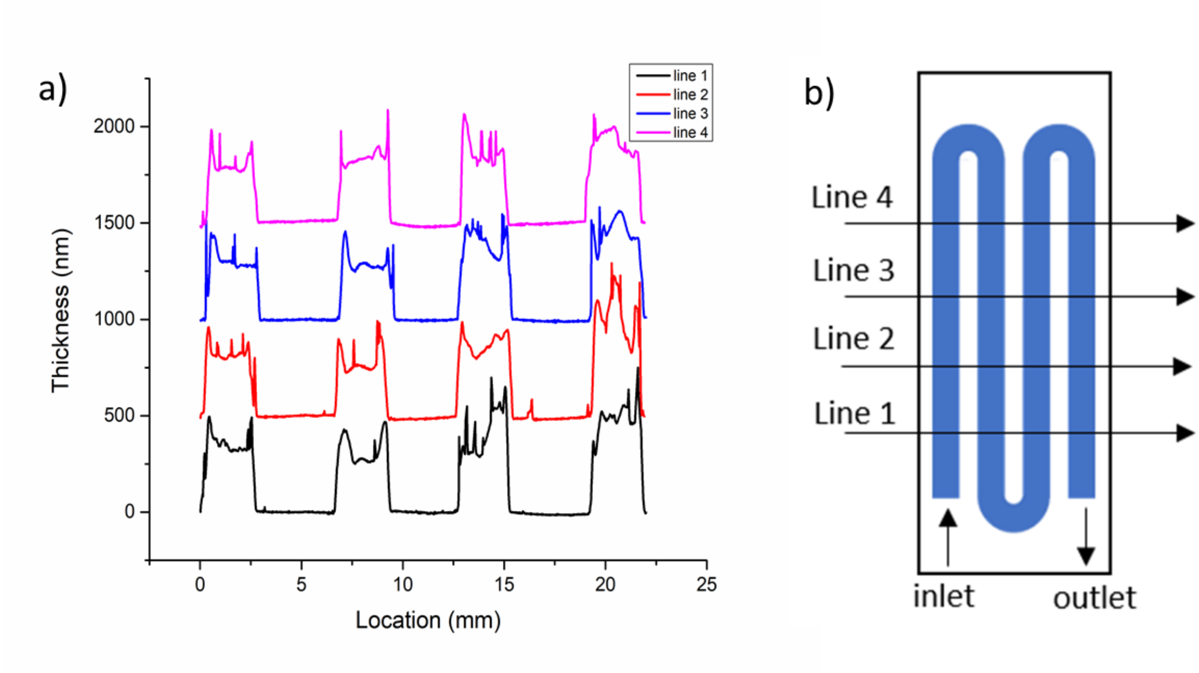

Figure 28 The thickness of the film measured by using profiler: a) the thickness of the film, b) the profiler measurement order and the flow direction for deposition of the ZnO film

Figure 28 shows the thickness of the ZnO film coated on the quartz substrate. The thickness of the film is estimated by the stylus profiler, at multiple spots from line 1 to line 4. From the stylus result, the thickness of the film is between 400 to 500nm. The ZnO film deposited on quartz also shows that the film is thinner in center of the channel, but thicker close to the wall. In addition, it shows that the film at different location have similar thickness, which is due to the fast transport of the solution and the relatively low temperature difference between the substrate and the fluid.

3.10 Characterization of the photocatalytic performance of the device

3.10.1 The photocatalytic degradation of the MB with the time

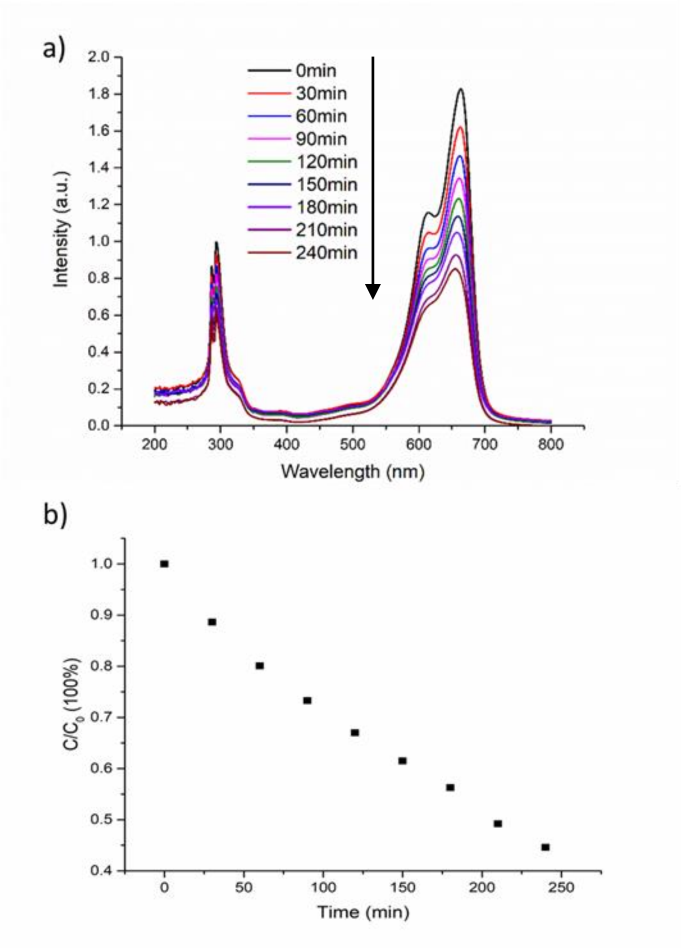

Figure 29 UV-VIS absorption spectra of the MB solution from the reservoir measured in an interval of 30min: a) the change of the absorption spectra, b) the change of the MB concentration in the solution

To estimate the performance of the microfluidic device in photodegradation, 10ml of the 0.03mM of MB was prepared in the reservoir. The cycle of the solution through the device was driven by the peristaltic pump in a fixed flow rate at 1.92mL/min. The MB solution was under photodegradation for 240min. The solution in the reservoir was measured by UV-VIS every 30min to observe the change of the intensity. It can be clearly seen that the MB was continuously degraded as the intensity was dropping with the time, as shown in Figure 29 (a). It shows that it takes 3h to degrade half of the concentration of MB in the solution. The decomposition rate is slow comparing to the literature.[128] Despite of the different setup of the decomposition system, the main reason for the low photodegradation efficiency is due to the relatively high density of the ZnO nanostructure, which can lead to the low surface area for the reaction to occur.

3.10.2 Kinetics study

In the photocatalysis device, the reaction rate can be regarded as the pseudo-first-order reaction with respect to the MB concentration, and the degradation rate is:

$$r = -\frac{dC_{t,c}}{dt} = k_{obs}C_{t,c} \qquad Eq(10)$$

Where k_{obs} is the observed rate constant, and the $C_{t,c}$ is the concentration of the MB.

The observed rate constant is a result of competitive adsorption by intermediates,[129] which can be written as follows:

$$k_{obs} = \frac{k_{L-H}K_{ads}}{1 + K_{ads}C_{0,MB}} \qquad Eq(11)$$

Where the k_{L-H} is the reaction rate constant, K_{ads} is the adsorption coefficient of MB on the ZnO surface, $C_{0,MB}$ is the initial concentration of the MB.

The microfluidic device can be modeled as a plug flow reactor, by assuming the fluid is well mixed in the radial and angular direction. The mass balance equation for the plug flow reactor at the steady state can be expressed as follow:

$$\frac{dC_{MB}}{dV_D} = \frac{r}{Q} \qquad Eq(12)$$

By substitute Eq (10) into Eq (12) we get:

$$\frac{dC_{MB}}{dV_D} = \frac{k_{obs}C_{MB}}{Q} \qquad Eq\ (13)$$

Solving Eq (13) will obtain:

$$ln\frac{C_{MB,outlet}}{C_{MB,inlet}} = -\frac{V_D k_{obs}}{Q} = -\frac{Sk_{obs}}{Q}l = -k'_{obs}l \qquad Eq(14)$$

And

$$k'_{obs} = \frac{Sk_{obs}}{Q} \qquad Eq\ (15)$$

In Eq (14), the $C_{MB,outlet}$ and $C_{MB,inlet}$ is the MB leaving and entering the photocatalysis device, V_D is the volume of the channel, S is the cross section area of the channel, which is 0.3cm^2; and *l* is the channel length, which is fixed at 15cm. k'_{obs} is the observed reaction rate constant as a function of length and flow rate. To estimate the observed rate constant, the 10ml of MB is supplied to the photocatalysis device, and the solution leaving the device was collected without cycling. Figure 30(a) has shown the absorption intensity of the MB before and after flow through the device at different flow rate. It clearly shows that under higher flow rate, the photodegradation efficiency is reduced. By comparing the change of the absorption intensity of the MB entering and leaving the device, the k'_{obs} can be estimated. In Figure 30(b), it shows a linear relation between the k'_{obs} and the v^{-1}, which is in good agreement with the Equation (14).

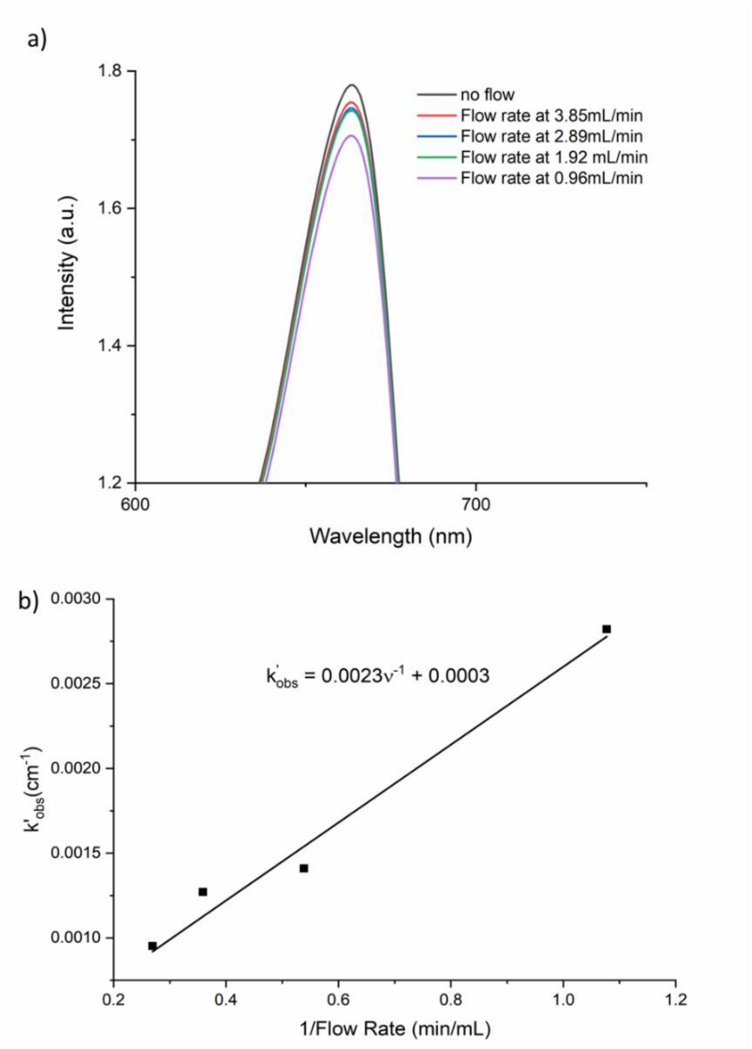

Figure 30 a) the absorption intensity of the MB after photodegradation; b) relation between k'_{obs} and the flow rate

The cyclic performance of the photocatalysis device under different total amount of the MB and different flow rate is also estimated. The test is running for 30min, with a cycle flow of the MB solution. Figure 31(a) has shown the change of the MB concentration under different total amount of the MB. In this case, the flow rate is fixed at 1.92mL/min. With the increase of the total amount of the MB, the conversion percentage is decreased since more MB need to be decomposed.

In Figure 31(b), it has shown the performance of the photocatalysis device under different flow rates, but the total amount of the MB is fixed. In contrast to the result from Figure 30, the increased flow rate will also increase the photodegradation performance. This is mainly due to cycle of the MB solution. Since the solution leaving the device will flow back again to the device, a fast flow rate can result in more chance to flow through the ZnO film.

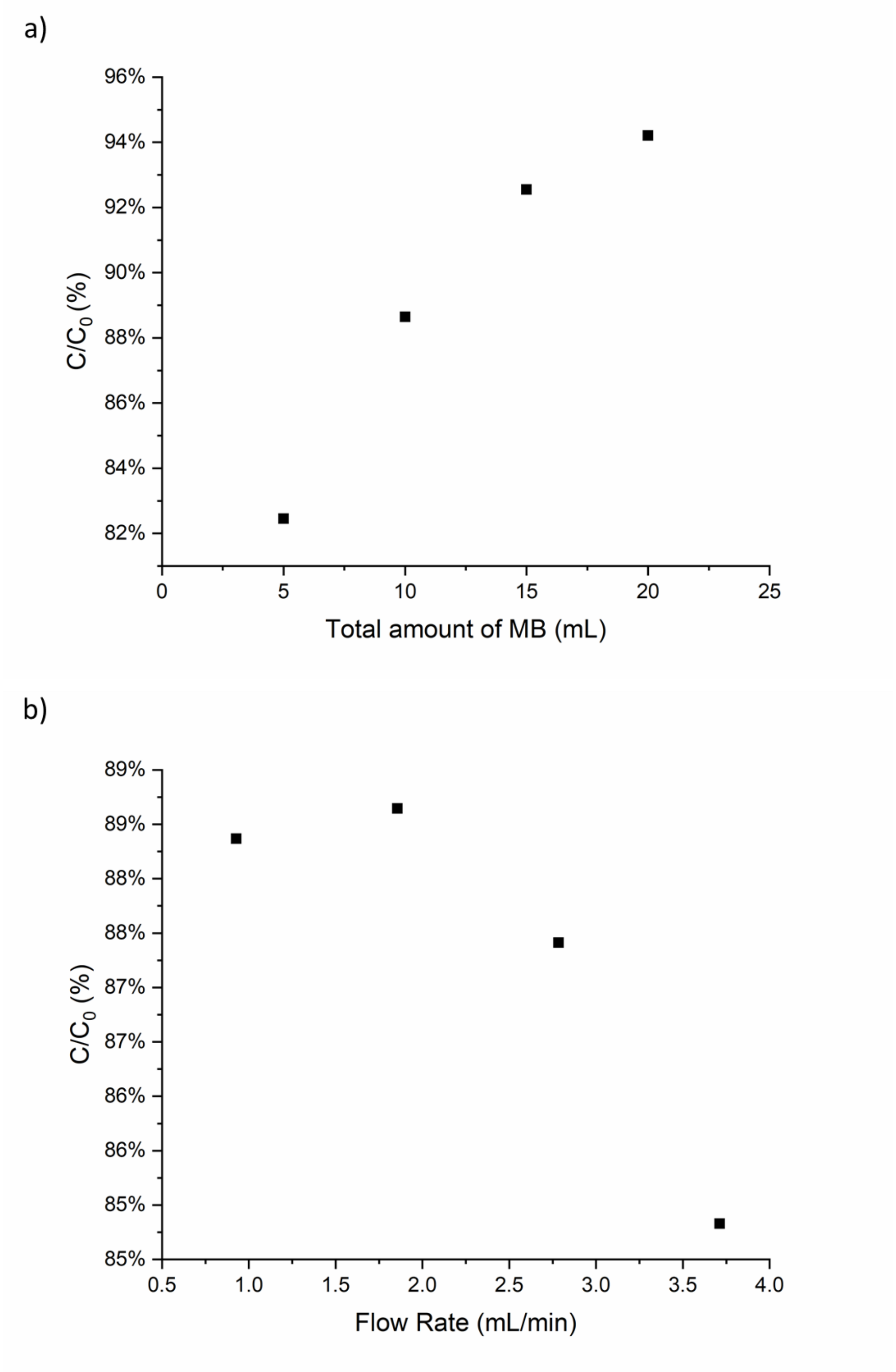

Figure 31 a) Photocatalytic efficiency under different total amount of the MB; b) under different flow rate

3. 11 Summary of the patterned ZnO photocatalytic performance

In this chapter, the utility of patterned nanostructured ZnO films is demonstrated via a photocatalytic flow reactor by flowing the Methylene Blue (MB) solution through the PDMS microchannel coated with ZnO nanostructured films. The UV-Vis absorption spectrophotometer determines the photodegradation of the MB. The photodegradation kinetics is estimated by assuming a first-order reaction analyzed as a plug flow reactor, and an observed reaction rate constant at 0.0023min^{-1} is obtained. The performance of the photocatalytic device under different flow rates and the different amount of the MB solution is also studied.

CHAPTER 4 PART I. CUO THIN FILM FABRICATED BY MICROREACTOR-ASSISTED NANOMATERIAL SYNTHESIS AND THE PRINTING PROCESS

4.1 Introduction

By combing the microreactor and the PDMS channels as mentioned in previous chapters, different materials from ZnO can also be deposited onto a substrate. In this chapter, the process to deposit cupric oxide (CuO) and copper hydroxide nitrate ($Cu_2(OH)_3NO_3$) using the combination of the MAND&PDMS channel is invesitaged. It shows that the process is capable of fabricating different materials by simply control the deposition condition, which makes it a useful tool for different thin film deposition. In addition, by controlling the process parameters, such as the reactants concentration or reaction temperature, CuO thin film with different morphologies or composition can be fabricate. Our process can also provide some insights of the growth mechanisms for the film, owing to its ability to control the composition and reaction degree of the precursor solution.

Cupric oxide (CuO) is an earth abundant metal oxide material that has wide application, due to its low cost, high stability and non-toxicity. CuO is an intrinsic p-type material with a band gap of 1.5eV. Many studies have been focused on the sensing properties of the CuO for different gas, including H_2S[130–132], H_2[133], CO[134] and ethanol.[135] The CuO often directly contacts a n-type material such as ZnO or SnO_2 to form a p-n junction to enhance the sensing ability. The sensing property of the CuO is based on the negatively charged oxygen absorbed on its surface. When in contact of the reducing gas, such as the H_2S or CO, the negatively charged oxygen will react and lead to the decrease of the hole density and the CuO conductivity.[136]

CuO can also work as the anode material for the lithium ion batteries due to tis high theoretical capacity, high safety, and low cost.[137] One drawback of the CuO that restrict its application is its large variation during lithium ions insertion/extraction process.[138] To overcome this drawback, CuO with different morphologies and composite structures are designed. For example, carbon nanotubes or graphene and CuO composite are fabricated to enhance the electronic conductivity and long term stability.[137,139] Different CuO morphologies, including microspheres, flower-like structures and thorn like structures have been made to improve the battery performance.[140]

In addition, CuO can also be used in condensation enhancement[141], where a hydrophobic CuO surface is fabricated on a substrate surface. During the condensation heat transfer process, as the vapor condensed to liquid in the form of droplets that has a high mobility and can be removed easily by gravity. The high mobility of the droplet formed on the CuO surface will enhance the heat transfer efficiency during the condensation process.

Other applications of the CuO, including the p-type thin film transistor[142], photovoltaic and photocatalytic application[143,144], and antibacterial activity have also been reported.

Due to its wide applications in different area, several methods have been developed to fabricate CuO thin film with diverse sizes and morphologies, including the electrochemical method[145], chemical vapor deposition method[146], heat treatment method[147], spray pyrolysis[148], and the hydrothermal method[149]. Among those methods, hydrothermal method has attracted a lot of attention due to its easy procedure, low cost, and its capability to create different nanostructure.

In a typical solution process for CuO, the precursor solution containing both the copper salt and alkaline hydroxide will be added into a beaker. By varying the concentration of the alkaline species, different nanostructures of CuO can be achieved.[150] Liu et al. has demonstrate the process to synthesize the aligned CuO by a seed mediated hydrothermal method.[151] In the hydrothermal method, the Cu^{2+} from the dissolved copper salt will firstly react with hydroxide ions OH^- from the alkaline hydroxide to form the $Cu(OH)_2$, which is usually regarded as the building block for the CuO.[152] Then the $Cu(OH)_2$ will further decompose to form the CuO under different conditions. The overall reaction procedures are shown below:

$$\mathrm{OH^-} + \mathrm{Cu^{2+}} \rightarrow \mathrm{Cu(OH)_2} \rightarrow \mathrm{CuO} + \mathrm{H_2O}$$

Different OH^- from the alkaline hydroxide has also be used to make the CuO, namely the hexamethylenetetramine (HMTA). The HMTA will be decomposed upon heating and generate the formaldehyde (HCHO) and ammonia ($\mathrm{NH_3}$). The ammonia will further react with water (11) to form the $\mathrm{OH^-}$ and the ammonium ions ($\mathrm{NH_4^+}$). The hydroxide ions can react with the $\mathrm{Cu^{2+}}$ to form the $Cu(OH)_2$. The reaction of the decomposition of the HMTA in a heated water is:

$$\mathrm{(CH_2)_6N_4} + 6\mathrm{H_2O} \rightarrow 6\mathrm{HCHO} + 4\mathrm{NH_3}$$

$$\mathrm{NH_3} + \mathrm{H_2O} \rightarrow \mathrm{NH_4^+} + \mathrm{OH^-}$$

Studies have been focused on fabricating different CuO structures by controlling the growth parameters, including the temperature, reactants, concentrations, and the surfactants. For example, Fterich et al.[153] has prepared the nanoparticles of CuO under different HMTA concentration and has shown that the sample with low concertation of HMTA has a high crystallite size and a low strain. Xu et al.[154] has synthesized different structure of the CuO by changing the pH and the reactants concentration. Surfactant, such as CTAB is also added to the solution to achieve a flower-like nanostructures, and during the growth process, the $\mathrm{Cu(OH)_4^{2-}}$ is considered as the building block for the CuO, since it will form $\mathrm{CTA^+ - Cu(OH)_4^{2-}}$ ion pairs during the hydrothermal process.

In our MAND&PDMS process, same reactants as the hydrothermal method, copper nitrate and HMTA are used to form the CuO film. The chemical reactions by our process is same as the hydrothermal method, but the major difference is on the reactor type. As a continuous stirred process, the concentration of the reactants keeps changing throughout the process, while in our MAND&PDMS process, the nature of a continuous flow will maintain a constant concentration as long as the residence time is fixed. By using our process, it is possible to separate the building blocks formed under different growth condition, so that the growth of the CuO film can be more accurately controlled. Also, the growth mechanism of the CuO film can be better understand since the building block type and its concentration is fixed throughout the process.

4.2 Experimental

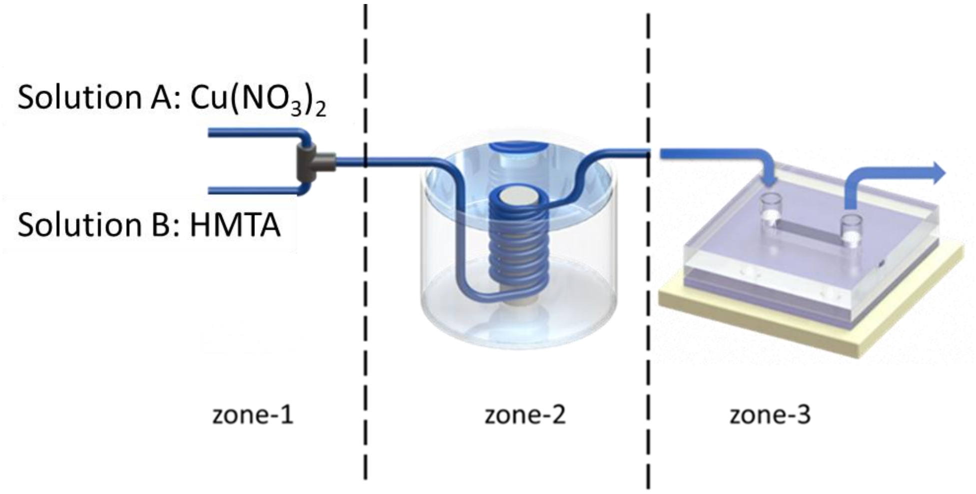

Figure 32 Schematic illustration of the deposition process of $CuO/Cu_2(OH)_3NO_3$

The patterned CuO thin film was deposited onto the silicon wafer substrate using the same method as the patterned ZnO film deposition, as shown in Figure 32. The silicon wafer was cleaned by rinsing with acetone, methanol, and DI water and then immersed into 1M of NaOH for 5min to turn the surface to hydrophilic. After rinsed by DI water, and dried by nitrogen gas, a seed layer of copper oxide was deposited onto the substrates by spin coating the copper iodide (CuI, Alfa Aesar) in acetonitrile (Fisher Scietific) followed by annealing at 250℃ in the air for 1h. The CuO seed layer is to provide nucleation sites for the growth of the film.

To grow the CuO nanorods, 0.01M aqueous cupric nitrate ($Cu(NO_3)_2{\cdot}2.5H_2O$, J. T. Baker) and 0.02M hexamethylenetetramine (HMTA, $(CH_2)_6N_4$, Alfa Aesar) solutions were mixed and flew through a 1 meter helical structured tubing, similar as the setup to grow ZnO nanorods. This will result in a ratio between copper and HMTA (Cu/HMTA) equals to 1: 2. The helical tubing was immersed into a water bath to heat up the mixed solution. The precursor solution was then supplied to the silicon substrate through a PDMS channel for the growth of the CuO. The substrate was heated by using a heating pad to control the growth temperature and with the building blocks formed in the tubing will further react on the substrate surface to form the CuO film.

In this study, the system is also divided to 3 different zone, same as the ZnO deposition process. The growth conditions controlled in this process are the ratio between Cu and HMTA in zone-1, the bath temperature in zone-2 and the growth temperature of the film in zone-3. The film growth under different conditions shows a different morphologies and composition. Thus, it shows the capability of the microreactor-assisted nanomaterial synthesis and the printing process to deposit different films with tunable properties.

4.3 Result and discussion

4.3.1 CuO thin film fabricated with Cu/HMTA ratio at 1:2

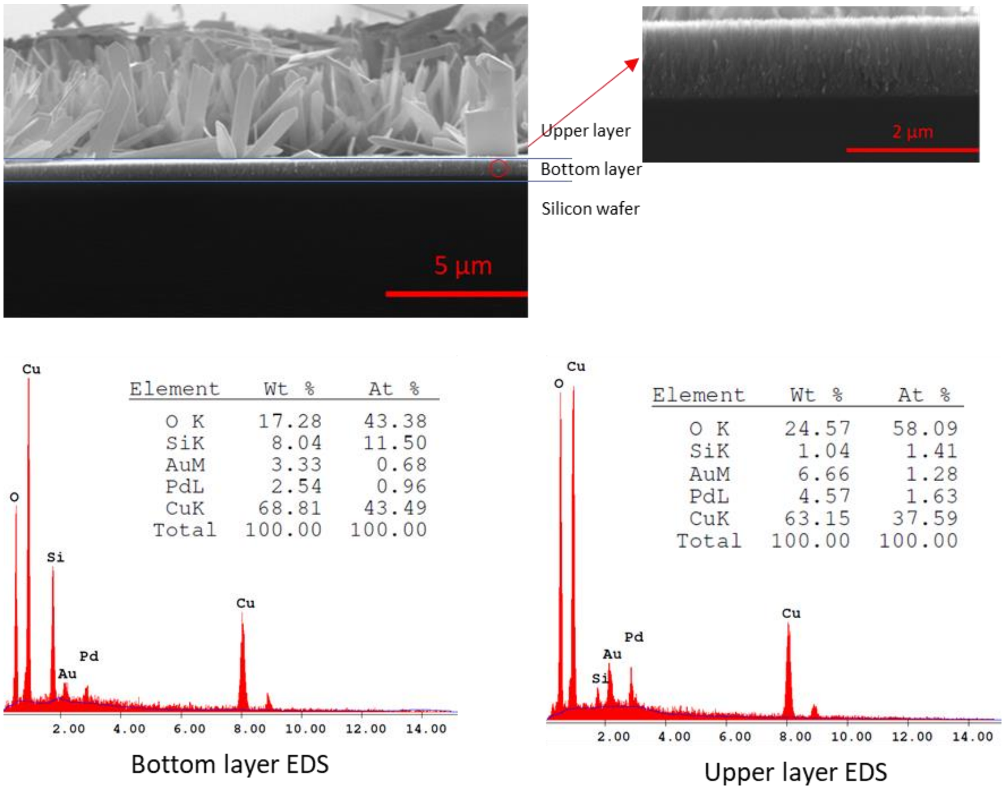

Element	Wt %	At %
O K	17.28	43.38
SiK	8.04	11.50
AuM	3.33	0.68
PdL	2.54	0.96
CuK	68.81	43.49
Total	100.00	100.00

Bottom layer EDS

Element	Wt %	At %
O K	24.57	58.09
SiK	1.04	1.41
AuM	6.66	1.28
PdL	4.57	1.63
CuK	63.15	37.59
Total	100.00	100.00

Upper layer EDS

Figure 33 SEM image of the CuO film grown by MAND&PDMS channel and the EDS result for the films

Figure 33 has shown the CuO film grown by using 0.02M HMTA and 0.01M aqueous cupric nitrate solution for 10min. The bath temperature in zone-2 is maintained at 70℃ while the substrate temperature in zone-3 is at 80℃. It can be clear observed that two layers are formed: a bottom layer consisting a dense thin film made of CuO, and an upper layer consisting of larger nanoplates made of $Cu_2(OH)_3NO_3$. The picture on the right has shown an enlarged view of the bottom layer. The CuO film is about 1.12μm in thickness and has the copper to oxygen ratio about 1 to 1, as indicated by the EDS result from the bottom layer in Figure 33. The upper layer consists larger plates with a length of 5μm, standing loosely to each other. The ratio between copper and oxygen for this upper layer is about 2 to 3, as indicated by the EDS result. In addition, the film on the bottom layer is much denser than the upper layer. Both morphology and composition difference between upper and bottom layer have implied a different growth mechanism for the two layers.

4.3.2 CuO thin film fabricated at different bath temperature

To further study the growth mechanism of the film deposited by our method, different ratios of the copper nitrate and the HMTA, and different bath temperatures was applied.

The film was deposited on the silicon wafer substrate with different bath temperature in zone-2 at 80℃, and 90℃. The substrate temperature was kept same at 80℃ throughout the growth. From the Figure 34, it can be found that as the bath temperature increased to 80˚C and 90˚C, the upper layer of the $Cu_2(OH)_3NO_3$ is disappeared. At 90˚C, only the dense CuO layer is left. Also, the thickness of the dense film is reducing as the bath temperature increasing. As illustrated in Figure 33, the film deposited at 80˚C has the thickness of 710nm, and at 90˚C has the thickness about 650nm.

The reason for the change of the thickness of the film and the film structure is due to the change of the decomposition of the HMTA. The HMTA is gradually decomposed in the tubing. As the temperature increased, the decomposition rate of the HMTA is also increased, which will lead to an increased concentration of the OH^-. The OH^- will react with Cu^{2+} to form $Cu(OH)_2$. According to our experiment result, when under lower temperature, less OH^- are generated, and no sufficient OH^- are provided to convert all the Cu^{2+} to $Cu(OH)_2$, instead the $Cu_2(OH)_3NO_3$ are produced . When under higher temperature, more OH^- are generated, and the $Cu(OH)_2$ is the major reactants, which will lead to the formation of the thinner but denser CuO film. Eventually, it's the two reactions competing to grow on the substrate surface, resulting in different morphologies and composition.

On the other hand, as the solution temperature increasing when flowing through the tubing, the homogeneous reaction will also be increased in zone-2, resulting in a consumption of the reactants in the solution. Thus, less reactants will be supplied to the substrate surface and the film, resulting in a thinner CuO film

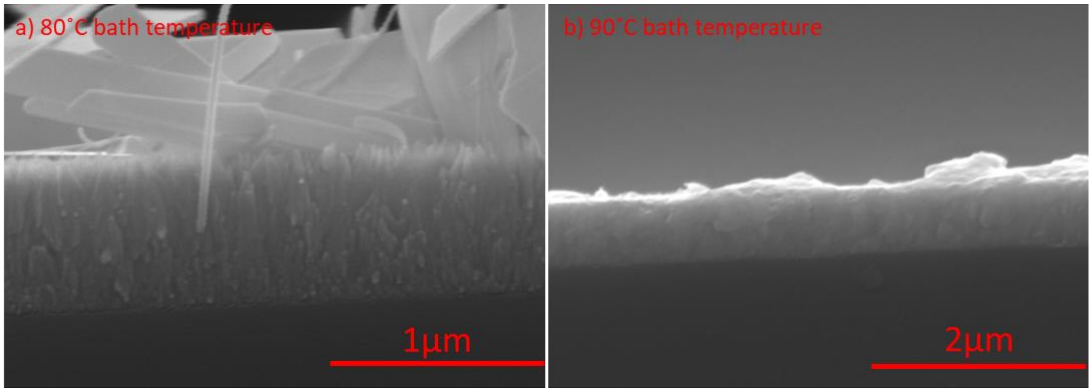

Figure 34 CuO deposited with bath temperature at: (a) 80˚C and (b) 90˚C

4.3.3 CuO thin film fabricated at Cu/HMTA ratio at 1.5: 1 and 1: 6

The film is also deposited with different copper nitrate and HMTA ratio, as controlled in zone-1. The bath temperature and the substrate temperature are both set to 80˚C. The molarity ratio between copper nitrate and the HMTA is controlled to be 1.5 to 1 with a relatively higher concentration of copper, and to 1 to 6 with a higher concentration of the HMTA. Figure 35 has shown the SEM result of the deposited film with different ratio between copper and HMTA. It has shown in Figure 35(a) that with a higher concentration of HMTA, the larger plates are disappeared, with only the CuO film left similar as the result with higher bath temperature. The EDS result in Figure 35(c) shows the ratio between copper and oxygen in the film is close to 1:1, indicating the formation of the CuO film. On the other hand, the CuO film is gone when the copper concentration is higher than the HMTA, only the $Cu_2(OH)_3NO_3$ plates are fabricated on the substrate, with a copper to oxygen ratio at 1.8:1, as shown in Figure 34(b) This again can be explained by the OH^- concentration. With a higher ratio between copper and HMTA, the concentration of OH^- is lower so that not sufficient of $Cu(OH)_2$ can be formed, while with a higher ratio between HMTA and copper, the OH^- concentration is increased, and $Cu(OH)_2$ is the dominate reactant and CuO film is deposited.

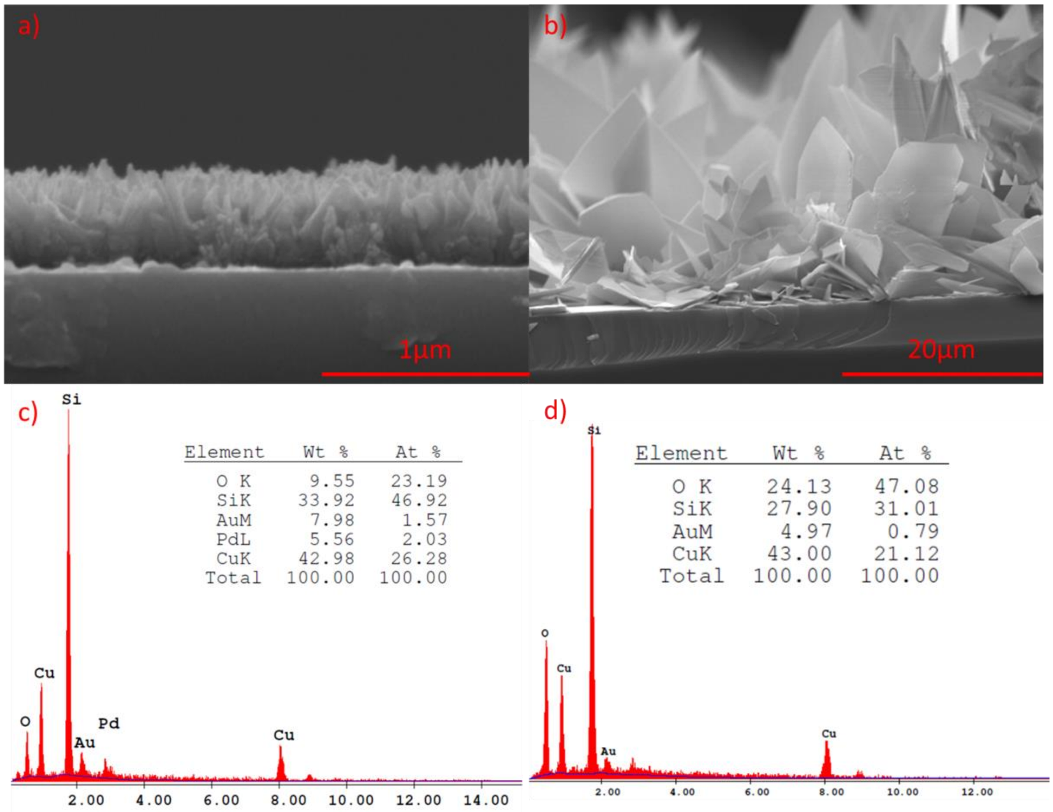

c)

Element	Wt %	At %
O K	9.55	23.19
SiK	33.92	46.92
AuM	7.98	1.57
PdL	5.56	2.03
CuK	42.98	26.28
Total	100.00	100.00

d)

Element	Wt %	At %
O K	24.13	47.08
SiK	27.90	31.01
AuM	4.97	0.79
CuK	43.00	21.12
Total	100.00	100.00

Figure 35 SEM image of the CuO film deposited with Cu/HMTA ratio at: a) 1:6 and b)1.5:1, and the corresponding EDS result:c),d).

In addition, the morphology of the film is also different. For the CuO film deposited with Cu/HMTA ratio at 1:6, the film is not as dense as the CuO film with the ratio at 1:2. For the $Cu_2(OH)_3NO_3$ plates film, a higher concentration of the copper will form rectangular plates, while the plates formed in Cu/HMTA ratio at 2:1 ratio is more like a nanorod structure with a higher aspect ratio.

A schematic illustration of the growth mechanism under different growth condition is shown on Figure 36. It is essential to control the amount of the OH^- in the solution to deposit different types of the film on the substrate. A higher concentration of OH^- can lead to the formation of the CuO thin film, and lower concentration of OH^- can lead to the formation of the $Cu_2(OH)_3NO_3$ plates. One advantage of the combination of the micro-reactor system and the PDMS channel is that it can generate the precursor solution constantly with fixed concentration, which allows the study of the growth conditions of different materials. Another advantage is that the growth condition can be controlled through the system, which provides a useful tool for fabricating various thin films.

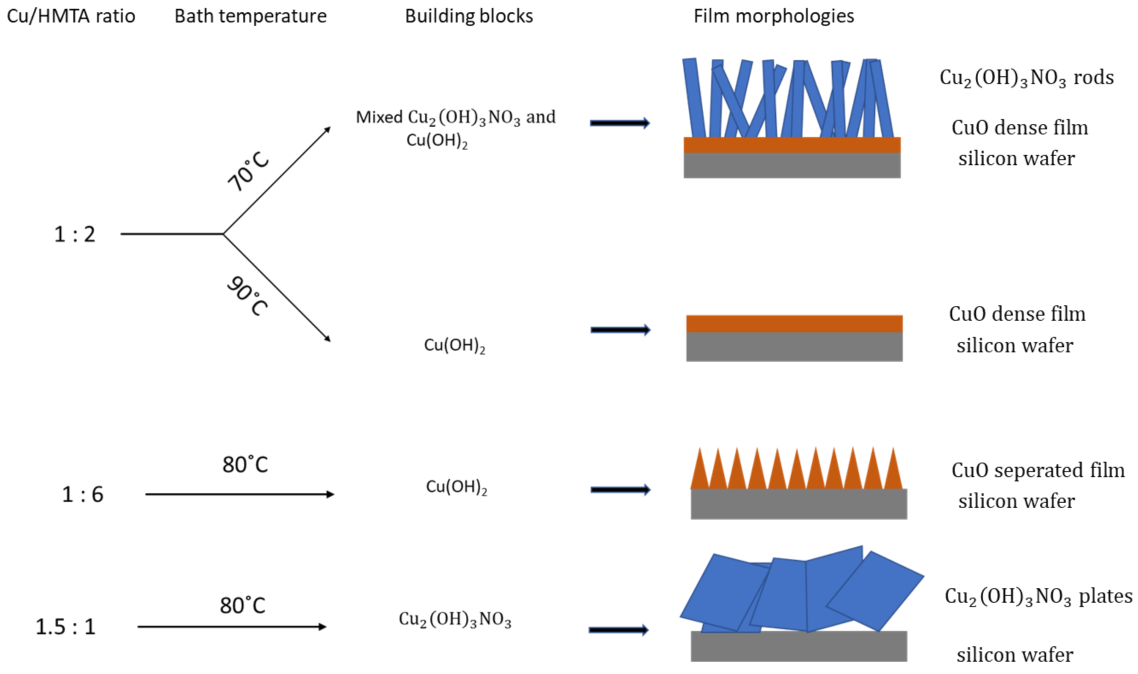

Figure 36 Schematic illustration of the growth of different film morphologies under different deposition condition

4.3.4 Conversion of the $Cu_2(OH)_3NO_3$ to CuO

The $Cu_2(OH)_3NO_3$ formed at the Cu/HMTA ratio of 1.5 to 1 is heated in air under 450˚C for 30min. As shown in Figure 37 (a), the color has changed from blue to dark brown, indicating a CuO film has formed. The Figure 37(b) has shown the SEM image of the converted film and its EDS result. It is clearly can be seen that the smooth $Cu_2(OH)_3NO_3$ plates are decomposed and replaced by nanoparticles. The EDS result shown the ratio between copper and oxygen is about 1.48 to 1. The lack of the oxygen atoms is probably due to Cu_2O formed between 200˚C and 300˚C.[155]

The film was analyzed by using XRD to identify the change of the crystal phase. As shown in Figure 38, it has shown a strong peak at 12.8˚ and 25.7˚ for the sample prepared with Cu/HMTA ratio at 1.5:1, which indicates the formation of the $Cu_2(OH)_3NO_3$ crystal. After annealing, the peaks are gone, indicating the decomposition of the $Cu_2(OH)_3NO_3$, as discussed above. In addition, it also shows the $Cu_2(OH)_3NO_3$ peak for the film prepared at Cu/HMTA ratio at 1:2 and bath temperature 80˚C. The weak of the $Cu_2(OH)_3NO_3$ is expected, since it only partially formed the $Cu_2(OH)_3NO_3$ layer.

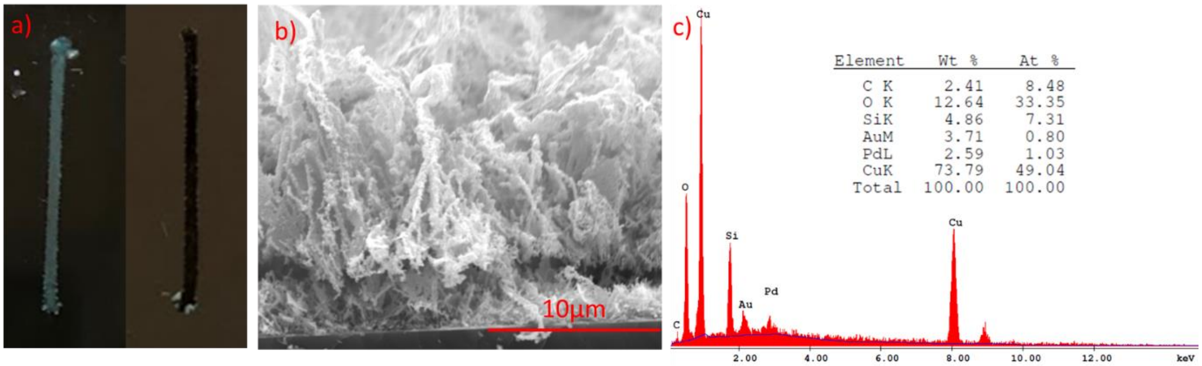

Element	Wt %	At %
C K	2.41	8.48
O K	12.64	33.35
SiK	4.86	7.31
AuM	3.71	0.80
PdL	2.59	1.03
CuK	73.79	49.04
Total	100.00	100.00

Figure 37 a) Optical image of the $Cu_2(OH)_3NO_3$ before and after annealing; b) SEM image and c) EDS result of the annealed $Cu_2(OH)_3NO_3$

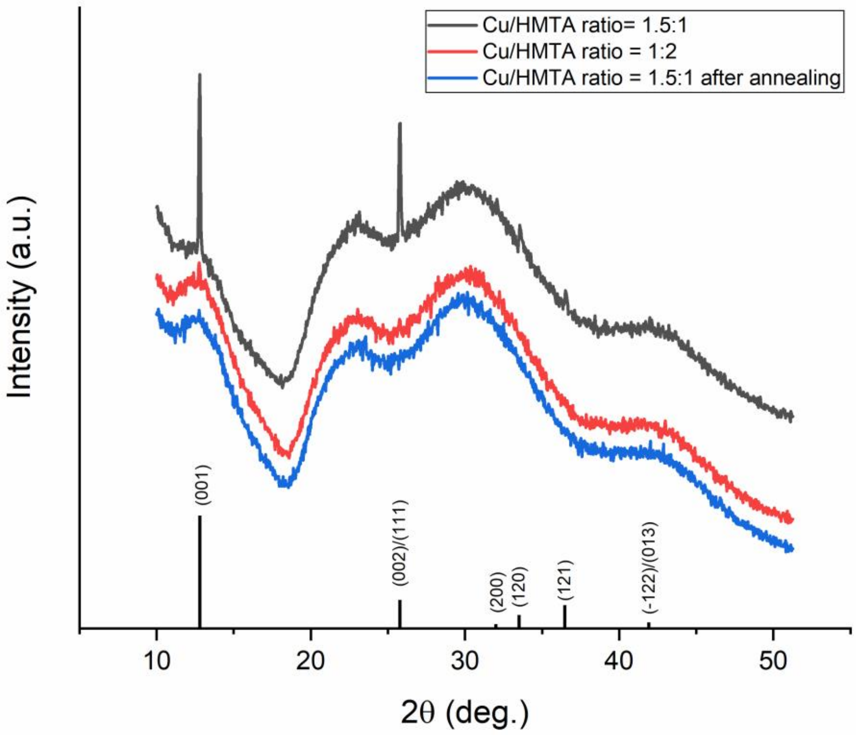

Figure 38 XRD patterns of the CuO and $Cu_2(OH)_3NO_3$

4.3.5 Conversion of the hydrophilic surface of CuO to hydrophobic

From figure 39 (a) it can be found that the as-deposited CuO film is super-hydrophilic, with a contact angle of 16.7˚. The CuO film is fabricated at Cu/HMTA ratio at 1:6, and at 80˚C for both bath temperature and substrate temperature. However, it is reported that the surface will gradually turn to hydrophobic due to the decomposition of CuO to Cu_2O.[156] And our result has shown similar trend after exposing the CuO surface to air for 2 weeks, as the contact angle has increased to 67.7˚, as shown in Figure 39(c). Besides, the uncoated surface that directly contacted with PDMS during the deposition process has a contact angle about 122.2° in Figure 39(b), which is probably due to the residual PDMS left on the substrate surface. In this way, a hybrid surface with different wetting properties has been fabricated by using the microreactor-assisted nanomaterial synthesis and the printing process.

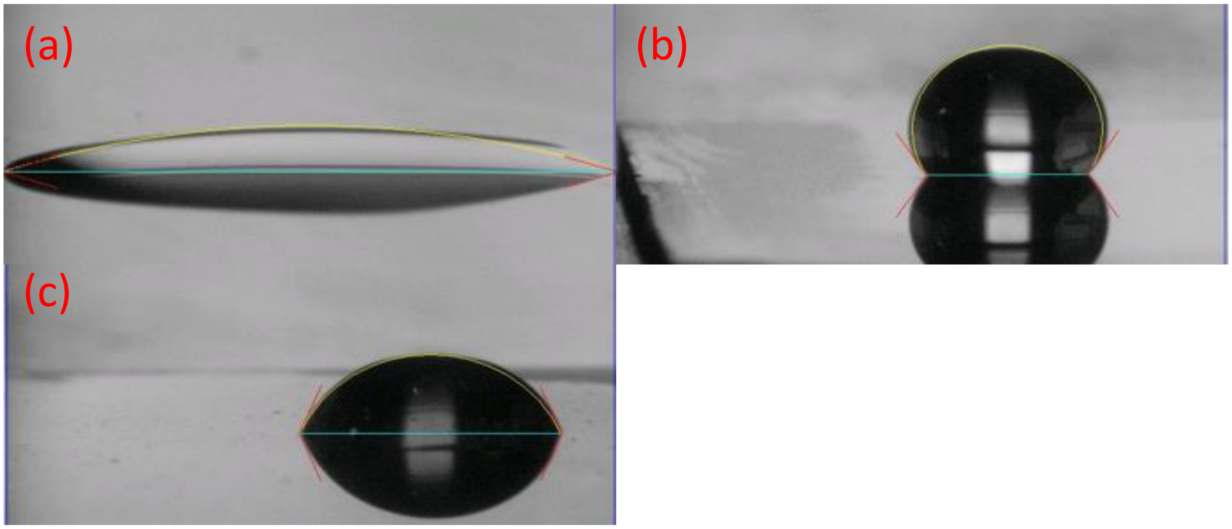

Figure 39 Contact angle for the (a) as-deposited CuO film by CBD method, (b) the uncoated substrate contacted with PDMS during deposition, (c) the CuO after 2 weeks in air.

4.4 Conclusion

In this study, the microreactor-assisted nanomaterial synthesis and printing process was used to deposit patterned CuO and $Cu_2(OH)_3NO_3$ nanostructures on surface, including dense nanocrystalline CuO film, CuO nanorods, $Cu_2(OH)_3NO_3$ nanorods, and $Cu_2(OH)_3NO_3$ nanoplates using the same reactants, $Cu(NO_3)_2$ and HMTA. The key process parameter that controls the formation of different products is the concentration of the OH^- in the solution, which can be controlled by the ratio of the reactants and the temperature of the microreactor. High concentration of OH^- leads to the formation of Cu(OH)2, which is then converted to CuO on the heated substrate surface. In contrast, low concentration of OH^- leads to the formation of $Cu_2(OH)_3NO_3$. These results show the applicablity of the microreactor-assisted nanomaterial synthesis and printing process to deposit metal oxide nanostructures with controlled structure and composition.

CHAPTER 4 PART II. ZNO/CUO DIODE FABRICATED BY USING THE MICROREACTOR-ASSISTED NANOMATERIAL SYNTHESIS AND THE PRINTING PROCESS

4.5 Introduction

In recent years, CuO/ZnO based-heterojunction has received growing attention in different fields, due to their stability, cost-effectiveness and unique properties of dimensionality-dependent. Coupling n-type ZnO and p-type CuO together to form p-n heterojunction is an effective approach to promote the charge separation and limit the charge recombination, and junction has been used in a variety of applications, including light detection[157,158], photocatalysis[159,160], gas sensing[132,161], solar cells[162,163], field emission.[164] Herein, we demonstrate the process to fabricate the ZnO/CuO heterojunction using the microreactor-assisted nanomaterial synthesis and the printing process. In this study, two different layers of thin film with CuO at the bottom and ZnO on the top can be fabricated successively, which enables more complicated thin film deposition. And these composite thin films can be potentially used in more fields than a single layer of the film.

4.6 Experimental details to fabricate ZnO/CuO

To fabricate the ZnO/CuO diode, a total thickness of 50nm of chromium (Cr) and gold (Au) was deposited by thermal evaporation method onto a glass substrate, as the electrical conductor. The CuO film was deposited onto the gold film following the same process as mentioned in Chapter 4, part I. The pattern used to fabricate the CuO film is a W shaped pattern, with width of 3mm for each line, and length of 37.5mm. To guarantee a pure CuO film, ratio between copper and HMTA is controlled at 3:1, with bath temperature at 80˚C and substrate temperature at 100˚C. After the growth of the CuO film, ZnO film was deposited onto the CuO thin film by following the same process described in Chapter 2. All the ZnO film were deposited under same condition, and a line pattern is used, with width of 1mm and length of 19mm. The ZnO has a smaller area than the CuO, so that no contact between ZnO and Au will occur. The overall process to fabricate the ZnO/CuO/Au diode is illustrated in Figure 40 with each ZnO/CuO line assigned with a number.

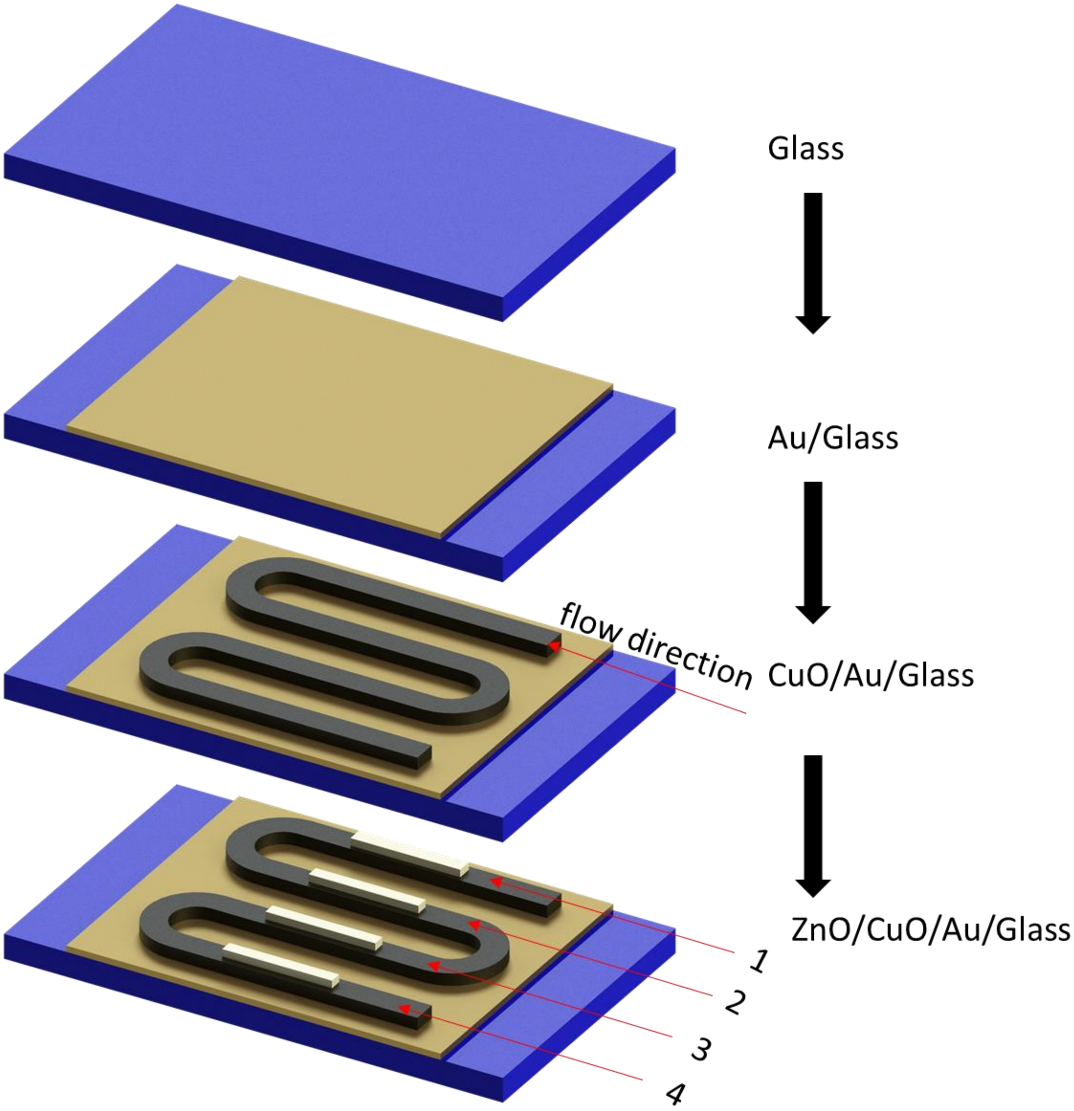

Figure 40 Process to fabricate ZnO/CuO/Au diode

4.7 Characterizations of the ZnO/CuO heterojunction

4.7.1 UV VIS

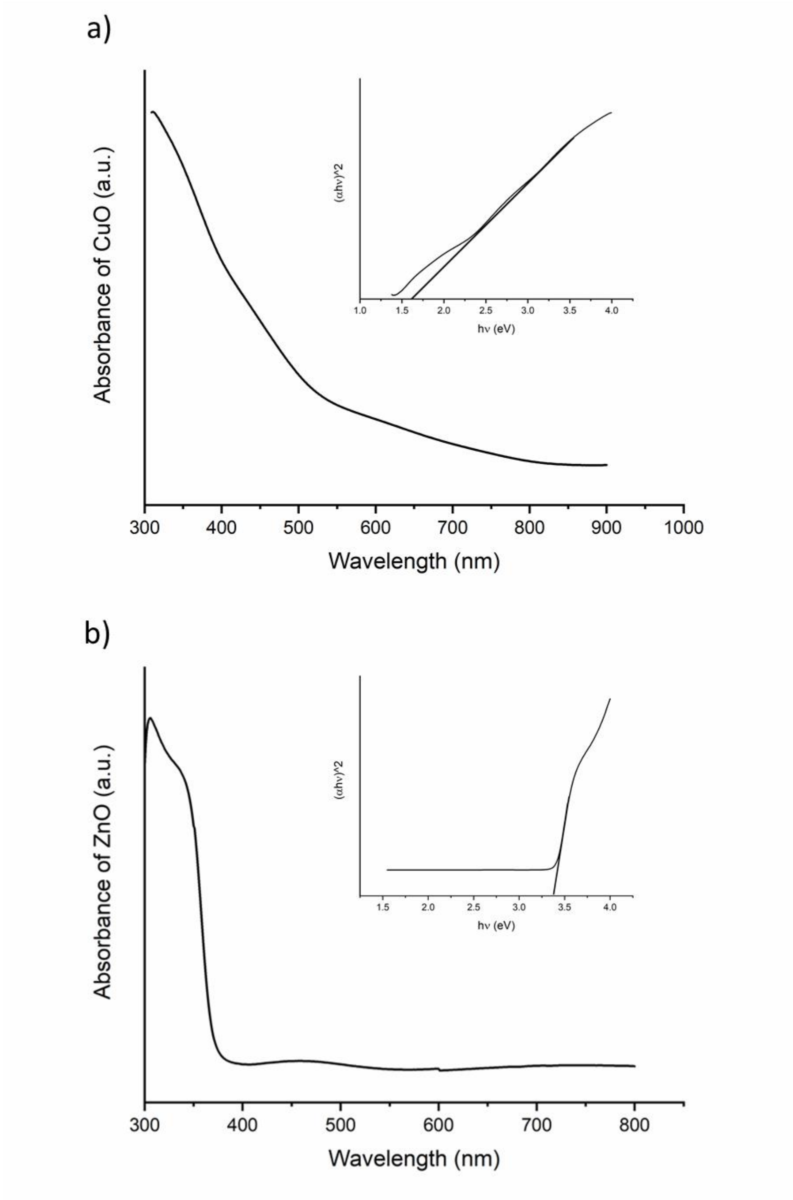

Figure 41 UV-VIS spectrum of a) as-deposit CuO film and b) ZnO film on glass. Inserted images are the calculated bandgap

Figure 40 shows the UV-VIS spectrum of the ZnO and CuO film coated on glass substrate. CuO is a p-type material with an indirect band gap of 1.2eV.[165] The UV-vis spectrum of the CuO shows a blue-shift and a wider band gap at 1.65eV, due to a quantum confinement effect.[38] The ZnO fabricated in this experiment has band gap of 3.4eV, which is similar as the film deposited in chapter 2.

4.7.2 SEM

Figure 42(a) shows the cross-sectional SEM of the ZnO/CuO/Au diode in the center of line 4, as marked in Figure 39. It has shown that the ZnO film is about 316nm, and CuO film is about 229nm in thickness. Both CuO layer and ZnO layer are relatively dense and have the same morphology as the individually deposited film. Also, the CuO film and the ZnO film are directly contacted. Figure 42 (b) shows an elemental mapping of copper and zinc. In chapter 3, it shows that the ZnO film has a low photocatalyst efficiency due to the dense packed ZnO nanostructure. However, the dense film can be an advantage in diode fabrication process. The dense packed of the film is important to avoid direct contact between probe and CuO, which can lead to the failure of the measurement of the electrical properties.

Also, the larger plates of the $Cu_2(OH)_3NO_3$ is not observed in SEM. Only a dense CuO film is observed on substrate. The lack of the $Cu_2(OH)_3NO_3$ is due to the high concentration of the HMTA that can provide sufficient OH^- for the formation of the CuO.

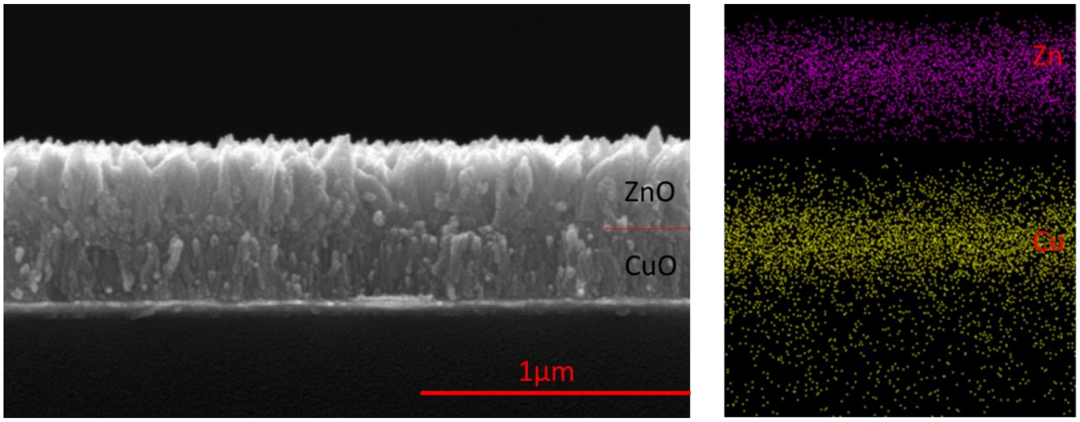

Figure 42 (a) Cross-sectional SEM image of ZnO/CuO/Au, and (b)elemental mapping of Cu and Zn

4.7.3 Stylus profiler

Figure 43 shows the thickness of CuO film and ZnO/CuO film measured by stylus profiler. The scan starts from line 1 to line 4, through the center of the lines. The thickness of the CuO film remains same after the growth of ZnO film. The ZnO film shows the same thickness for all the 4 lines, since the deposition conditions are identical. All the ZnO film have been deposited inside the CuO line without directly touching to the Au surface. From line 1 to line 4, the CuO film shows a slight increase of the thickness, which probably due to the increased temperature of the solution in the PDMS channel, the increased temperature will accelerate the reaction rate on the substrate surface, and also promote more OH^- formed in the solution to react with Cu^{2+}.

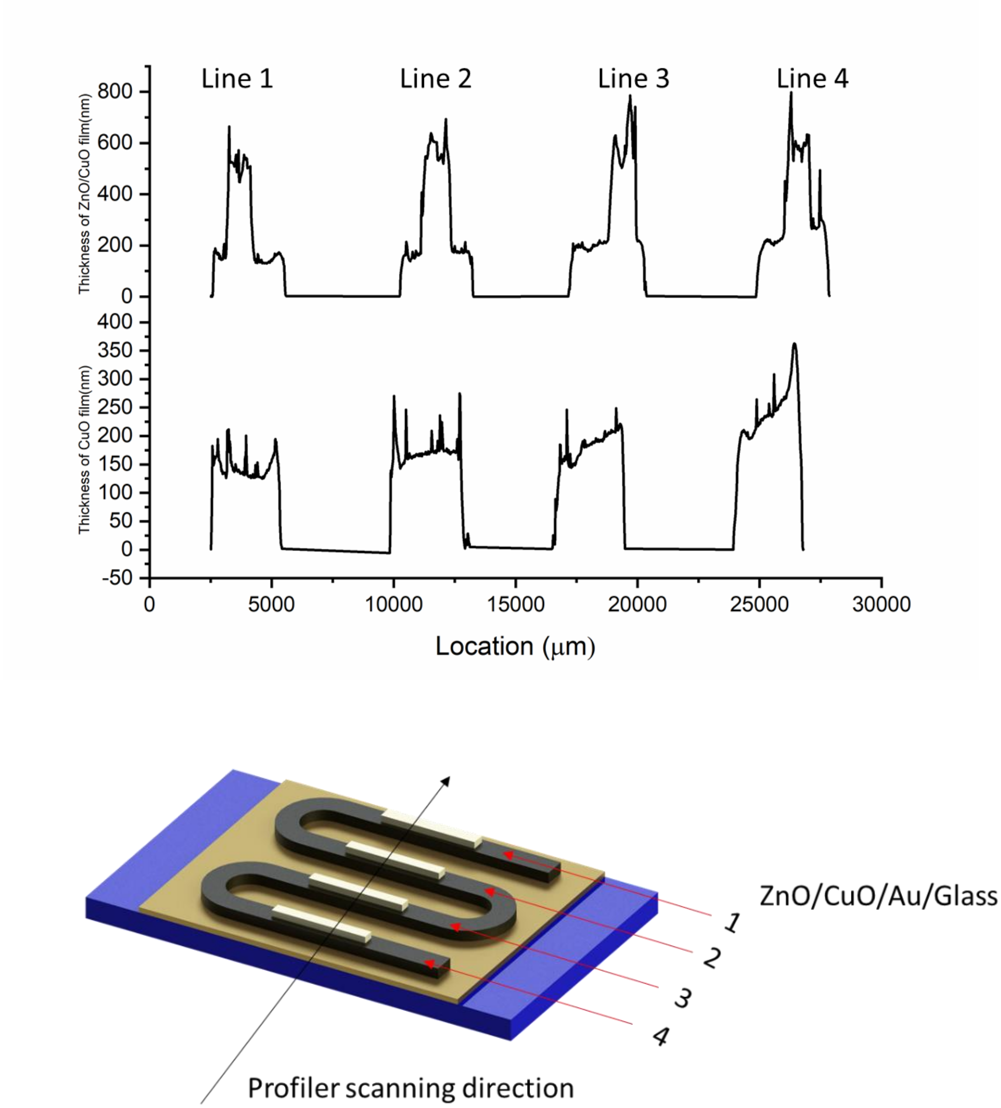

Figure 43 Thickness of CuO and ZnO/CuO measured by stylus profiler

4.7.4 Current-voltage characteristic of the ZnO/CuO diode

The current-voltage characteristics of the ZnO/CuO heterojunction diode on each line was studied at room temperature. The result is presented in Figure 44(a) in linear scale. The I-V result shows a similar trend for all the four diodes, which is probably due to the similar structure and thickness of the CuO and ZnO film. The rectifying behavior of I-V is presented at Figure 44 (b), by comparing the current at forward bias at 3V and reverse bias at -3V. Also, at higher forward bias, the current varies linearly with the voltage, suggesting bulk resistance controlled diode behavior.[166] The estimated the turn-on voltage is about 2V.

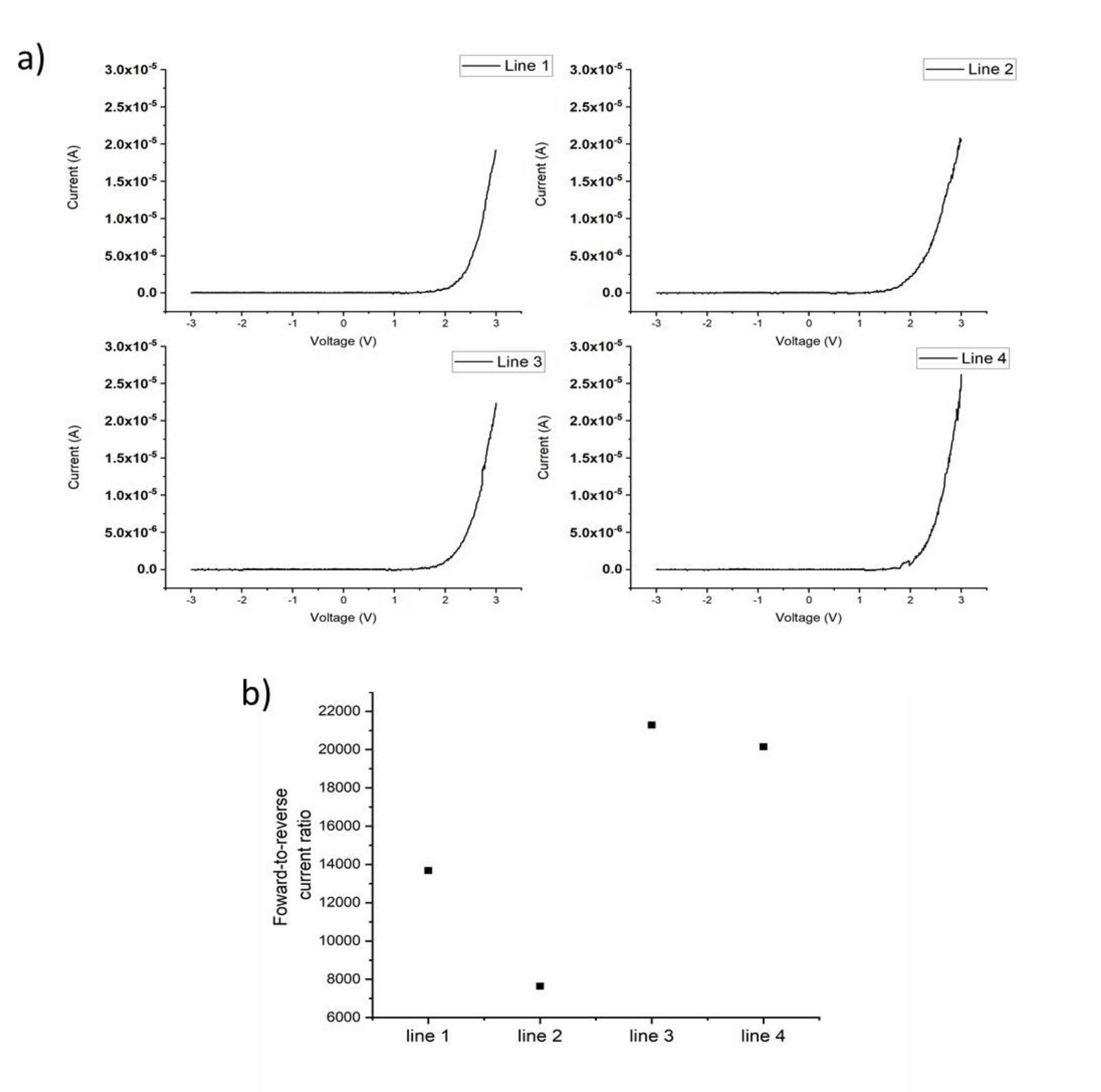

Figure 44 a) Forward and reverse bias I-V characteristics of ZnO/CuO heterojunction on each line, b) the rectifying behavior

4.8 Summary

In this study, heterojunction ZnO/CuO bi-layer film was successfully fabricated using the microreactor-assisted nanomaterial synthesis and printing process. The bilayer film was built by depositing a patterned nanocrystalline CuO film on a gold-coated glass surface using the microreactor-assisted nanomaterial synthesis and printing process, followed by the deposition of ZnO nanostructured film with a smaller-size pattern using the same process. The heterojunction ZnO/CuO bi-layer film shows rectifying behavior with a turn-on voltage of 2V; it allows currents to flow when forward biased and passes only low leakage currents with reverse bias; the p-n diode has a rectification ratio around 10^4, which is comparable to the values among the best solution-processed p-n junction diodes. The results of this study demonstrate the capability of our microreactor-assisted nanomaterial synthesis and printing process to fabricate structured thin films for functional devices.

CHAPTER 5: CONCLUSION AND FUTURE WORK

This dissertation has demonstrated a thin film deposition method by using the combination of microreactor-assisted nanomaterial deposition and the PDMS patterned microfluidic channel. The microreactor system is capable of generating various precursor solution with designated composition and concentration, which serve as the building blocks for the thin film growth. As the precursor solution supplied to the PDMS channel covering on the substrate, a thin film will be deposited on the substrate surface. The whole system is divided into 3 zones: a mixing zone, a homogeneous zone and a deposition zone. By controlling the growth parameters in different zones, the kinetics and mechanisms of the film growth can be studied.

In this study, ZnO and CuO thin film are successfully deposited onto different substrates by using the microreactor-assisted nanomaterial synthesis and the printing process, and it has been proven to be an efficient method to deposit nanostructured thin film. To better understand the ZnO thin film growth kinetics and to better control the thin film growth process, temperature of the microreactor, temperature of the substrate, residence time and the flow rate are controlled. A higher flow rate, lower residence time and higher temperature can lead to a faster growth of the film. The ZnO thin film thickness are measured by using scanning electron microscope (SEM) and stylus profiler. With the measured thickness data under different growth conditions and simulated result from COMSOL, the growth kinetics of the ZnO is estimated.

To demonstrate the printing capability of the microreactor-assisted nanomaterial synthesis and the printing process, the PDMS channels with different shapes are designed and applied to the deposition of ZnO thin film, and different patterns, including spiral patterns, parallel patterns and symmetry patterns, are successfully printed. Thickness measurement and the COMSOL simulation are used to give an insight of the properties of deposited thin film. It is found that the flow rate and the growth temperature are two major factors that influence the thickness of the film. And by controlling the flow rate, it is possible to fabricate the patterned thin film with uniform thickness.

CuO and $Cu_2(OH)_3NO_3$ film can also be obtained by using the same microreactor-assisted nanomaterial synthesis and the printing process. Different nanostructures and materials can be obtained by controlling the temperature and reactants composition in the microreactor. Owing to its capability of controlling the reaction conditions, the microreactor can generate the precursor solution with controlled ratio between Cu and HMTA, which eventually lead to the different growth path for the CuO and $Cu_2(OH)_3NO_3$. SEM and X-ray diffraction (XRD) are used to characterize the film deposited under different condition, and it is found that the concentration of the OH^- is the key to control the result.

The applications of the ZnO and CuO thin film deposited by this process are also studied. The patterned ZnO thin film is used as a photocatalyst for degradation of methylene blue (MB). The photocatalyst performance under different flow rate, total amount of the MB and the degradation time is studied to obtain the kinetics of the photocatalyst. In addition, the ZnO/CuO composite film is also fabricated by using microreactor-assisted nanomaterial synthesis and the printing process and exhibits the p-n junction property. The study shows that our process is capable of fabricating complicated films with different functions.

In conclusion, the microreactor-assisted nanomaterial synthesis and the printing process is developed, which can provide:

1) A fast, efficient scalable way to deposit nanostructured thin film with different film patterns.
2) A separation of the homogeneous and heterogeneous reaction to give an insight into the growth kinetics and mechanisms of the thin film.
3) A tool to fabricate thin film with different applications.

Two major area of future work is listed below:

1) To investigate the detailed reaction kinetics and mechanism inside the microreactor to fully understand the deposition process.
2) To investigate more applicable materials and the applications of patterned nanomaterials thin film.

BIBLIOGRAPHY

(1) Vyas, S.; Tiwary, R.; Shubham, K.; Chakrabarti, P. Study the Target Effect on the Structural, Surface and Optical Properties of TiO2 Thin Film Fabricated by RF Sputtering Method. *Superlattices and Microstructures* **2015**, *80*, 215–221. https://doi.org/10.1016/j.spmi.2014.10.029.

(2) Mahdi, M. A.; Hassan, J. J.; Kasim, S. J.; Ng, S. S.; Hassan, Z. Optical Properties of CdS Micro/Nanocrystalline Structures Prepared via a Thermal Evaporation Method. *Materials Science in Semiconductor Processing* **2014**, *26*, 87–92. https://doi.org/10.1016/j.mssp.2014.04.015.

(3) Rawlings, J. B.; Ekerdt, J. G. *Chemical Reactor Analysis and Design Fundamentals*, 1st ed.; Nob Hill Publishing.

(4) Strano, V.; Urso, R. G.; Scuderi, M.; Iwu, K. O.; Simone, F.; Ciliberto, E.; Spinella, C.; Mirabella, S. Double Role of HMTA in ZnO Nanorods Grown by Chemical Bath Deposition. *The Journal of Physical Chemistry C* **2014**, *118* (48), 28189–28195. https://doi.org/10.1021/jp507496a.

(5) Hodes, G. *Chemical Solution Deposition Of Semiconductor Films*; CRC Press, 2002.

(6) Zhou, Z.; Deng, Y. Kinetics Study of ZnO Nanorod Growth in Solution. *The Journal of Physical Chemistry C* **2009**, *113* (46), 19853–19858. https://doi.org/10.1021/jp907418z.

(7) Vas-Umnuay, P.; Chang, C. Growth Kinetics of Copper Sulfide Thin Films by Chemical Bath Deposition. *ECS Journal of Solid State Science and Technology* **2013**, *2* (4), P120–P129. https://doi.org/10.1149/2.008304jss.

(8) Moualkia, H.; Hariech, S.; Aida, M. S.; Attaf, N.; Laifa, E. L. Growth and Physical Properties of CdS Thin Films Prepared by Chemical Bath Deposition. *Journal of Physics D: Applied Physics* **2009**, *42* (13), 135404. https://doi.org/10.1088/0022-3727/42/13/135404.

(9) Hodes, G. Semiconductor and Ceramic Nanoparticle Films Deposited by Chemical Bath Deposition. *Physical Chemistry Chemical Physics* **2007**, *9* (18), 2181. https://doi.org/10.1039/b616684a.

(10) Borys, N. J.; Lupton, J. M. Surface-Enhanced Light Emission from Single Hot Spots in Tollens Reaction Silver Nanoparticle Films: Linear versus Nonlinear Optical Excitation. *The Journal of Physical Chemistry C* **2011**, *115* (28), 13645–13659. https://doi.org/10.1021/jp203866g.

(11) Zhang, P.; Wyman, I.; Hu, J.; Lin, S.; Zhong, Z.; Tu, Y.; Huang, Z.; Wei, Y. Silver Nanowires: Synthesis Technologies, Growth Mechanism and Multifunctional Applications. *Materials Science and Engineering: B* **2017**, *223*, 1–23. https://doi.org/10.1016/j.mseb.2017.05.002.

(12) Gao, Y.; Jiang, P.; Song, L.; Liu, L.; Yan, X.; Zhou, Z.; Liu, D.; Wang, J.; Yuan, H.; Zhang, Z.; et al. Growth Mechanism of Silver Nanowires Synthesized by Polyvinylpyrrolidone-Assisted Polyol Reduction. *Journal of Physics D:*

Applied Physics **2005**, *38* (7), 1061–1067. https://doi.org/10.1088/0022-3727/38/7/015.

(13) Chou, K.-S.; Hsu, C.-Y.; Liu, B.-T. Salt-Mediated Polyol Synthesis of Silver Nanowires in a Continuous-Flow Tubular Reactor. *RSC Advances* **2015**, *5* (38), 29872–29877. https://doi.org/10.1039/C5RA00320B.

(14) McPeak, K. M.; Baxter, J. B. ZnO Nanowires Grown by Chemical Bath Deposition in a Continuous Flow Microreactor. *Crystal Growth & Design* **2009**, *9* (10), 4538–4545. https://doi.org/10.1021/cg900551f.

(15) Choi, C.-H.; Allan-Cole, E.; Chang, C. Room Temperature Fabrication and Patterning of Highly Conductive Silver Features Using in Situ Reactive Inks by Microreactor-Assisted Printing. *Journal of Materials Chemistry C* **2015**, *3* (28), 7262–7266. https://doi.org/10.1039/C5TC00947B.

(16) Ramprasad, S.; Su, Y.-W.; Chang, C.-H.; Paul, B. K.; Palo, D. R. Continuous Microreactor-Assisted Solution Deposition for Scalable Production of CdS Films. *ECS Journal of Solid State Science and Technology* **2013**, *2* (9), P333–P337. https://doi.org/10.1149/2.003309jss.

(17) Vas-Umnuay, P.; Kim, K.-J.; Kim, D.-H.; Chang, C.-H. Conformal Growth of Copper Sulfide Thin Films on Highly Textured Surface via Microreactor-Assisted Solution Deposition. *CrystEngComm* **2015**, *17* (14), 2827–2836. https://doi.org/10.1039/C4CE02374A.

(18) Su, Y.-W.; Paul, B. K.; Chang, C. Investigation of CdS Nanoparticles Formation and Deposition by the Continuous Flow Microreactor. *Applied Surface Science* **2019**, *472*, 158–164. https://doi.org/10.1016/j.apsusc.2018.02.157.

(19) He, Y.; Kim, K.-J.; Chang, C.-H. Continuous, Size and Shape-Control Synthesis of Hollow Silica Nanoparticles Enabled by a Microreactor-Assisted Rapid Mixing Process. *Nanotechnology* **2017**, *28* (23), 235602. https://doi.org/10.1088/1361-6528/aa6fa7.

(20) Huang, Y. Directed Assembly of One-Dimensional Nanostructures into Functional Networks. *Science* **2001**, *291* (5504), 630–633. https://doi.org/10.1126/science.291.5504.630.

(21) Yi, G.-C.; Wang, C.; Park, W. I. ZnO Nanorods: Synthesis, Characterization and Applications. *Semiconductor Science and Technology* **2005**, *20* (4), S22–S34. https://doi.org/10.1088/0268-1242/20/4/003.

(22) Wang, Z. L. Zinc Oxide Nanostructures: Growth, Properties and Applications. *Journal of Physics: Condensed Matter* **2004**, *16* (25), R829–R858. https://doi.org/10.1088/0953-8984/16/25/R01.

(23) Zhang, Y.; Yu, K.; Jiang, D.; Zhu, Z.; Geng, H.; Luo, L. Zinc Oxide Nanorod and Nanowire for Humidity Sensor. *Applied Surface Science* **2005**, *242* (1–2), 212–217. https://doi.org/10.1016/j.apsusc.2004.08.013.

(24) Xu, F.; Yuan, Z.-Y.; Du, G.-H.; Halasa, M.; Su, B.-L. High-Yield Synthesis of Single-Crystalline ZnO Hexagonal Nanoplates and Accounts of Their Optical and Photocatalytic Properties. *Applied Physics A* **2006**, *86* (2), 181–185. https://doi.org/10.1007/s00339-006-3745-3.

(25) Shi, R.; Yang, P.; Dong, X.; Ma, Q.; Zhang, A. Growth of Flower-like ZnO on ZnO Nanorod Arrays Created on Zinc Substrate through Low-Temperature Hydrothermal Synthesis. *Applied Surface Science* **2013**, *264*, 162–170. https://doi.org/10.1016/j.apsusc.2012.09.164.

(26) Seelig, E. W.; Tang, B.; Yamilov, A.; Cao, H.; Chang, R. P. H. Self-Assembled 3D Photonic Crystals from ZnO Colloidal Spheres. *Materials Chemistry and Physics* **2003**, *80* (1), 257–263. https://doi.org/10.1016/S0254-0584(02)00492-3.

(27) Bi, D.; Boschloo, G.; Schwarzmüller, S.; Yang, L.; Johansson, E. M. J.; Hagfeldt, A. Efficient and Stable CH3NH3PbI3-Sensitized ZnO Nanorod Array Solid-State Solar Cells. *Nanoscale* **2013**, *5* (23), 11686. https://doi.org/10.1039/c3nr01542d.

(28) Galoppini, E.; Rochford, J.; Chen, H.; Saraf, G.; Lu, Y.; Hagfeldt, A.; Boschloo, G. Fast Electron Transport in Metal Organic Vapor Deposition Grown Dye-Sensitized ZnO Nanorod Solar Cells. *The Journal of Physical Chemistry B* **2006**, *110* (33), 16159–16161. https://doi.org/10.1021/jp062865q.

(29) Saravanan, R.; Gracia, F.; Stephen, A. Basic Principles, Mechanism, and Challenges of Photocatalysis. In *Nanocomposites for Visible Light-induced Photocatalysis*; Khan, M. M., Pradhan, D., Sohn, Y., Eds.; Springer International Publishing: Cham, 2017; pp 19–40. https://doi.org/10.1007/978-3-319-62446-4_2.

(30) Lee, K. M.; Lai, C. W.; Ngai, K. S.; Juan, J. C. Recent Developments of Zinc Oxide Based Photocatalyst in Water Treatment Technology: A Review. *Water Research* **2016**, *88*, 428–448. https://doi.org/10.1016/j.watres.2015.09.045.

(31) Wang, L.; Kang, Y.; Liu, X.; Zhang, S.; Huang, W.; Wang, S. ZnO Nanorod Gas Sensor for Ethanol Detection. *Sensors and Actuators B: Chemical* **2012**, *162* (1), 237–243. https://doi.org/10.1016/j.snb.2011.12.073.

(32) Bhatia, S.; Verma, N.; Bedi, R. K. Ethanol Gas Sensor Based upon ZnO Nanoparticles Prepared by Different Techniques. *Results in Physics* **2017**, *7*, 801–806. https://doi.org/10.1016/j.rinp.2017.02.008.

(33) Jeong, M.-C.; Oh, B.-Y.; Ham, M.-H.; Lee, S.-W.; Myoung, J.-M. ZnO-Nanowire-Inserted GaN/ZnO Heterojunction Light-Emitting Diodes. *Small* **2007**, *3* (4), 568–572. https://doi.org/10.1002/smll.200600479.

(34) Wang, Z. L.; Song, J. Piezoelectric Nanogenerators Based on Zinc Oxide Nanowire Arrays. *Science* **2006**, *312* (5771), 242–246.

(35) Liu, B.; Zeng, H. C. Hydrothermal Synthesis of ZnO Nanorods in the Diameter Regime of 50 Nm. *Journal of the American Chemical Society* **2003**, *125* (15), 4430–4431. https://doi.org/10.1021/ja0299452.

(36) Kim, K.-S.; Kim, H. W. Synthesis of ZnO Nanorod on Bare Si Substrate Using Metal Organic Chemical Vapor Deposition. *Physica B: Condensed Matter* **2003**, *328* (3–4), 368–371. https://doi.org/10.1016/S0921-4526(02)01954-3.

(37) Tynell, T.; Karppinen, M. Atomic Layer Deposition of ZnO: A Review. *Semiconductor Science and Technology* **2014**, *29* (4), 043001. https://doi.org/10.1088/0268-1242/29/4/043001.

(38) Han, S.-Y.; Paul, B. K.; Chang, C. Nanostructured ZnO as Biomimetic Anti-Reflective Coatings on Textured Silicon Using a Continuous Solution Process. *Journal of Materials Chemistry* **2012**, *22* (43), 22906. https://doi.org/10.1039/c2jm33462c.

(39) Choi, C.-H.; Levin, J. B.; Chang, C. Continuous Formation of a Seed Layer and Vertical ZnO Nanowire Arrays Enabled by Tailored Reaction Kinetics in a Microreactor. *CrystEngComm* **2016**, *18* (44), 8645–8652. https://doi.org/10.1039/C6CE01822J.

(40) Wang, T.; Jiao, Z.; Chen, T.; Li, Y.; Ren, W.; Lin, S.; Lu, G.; Ye, J.; Bi, Y. Vertically Aligned ZnO Nanowire Arrays Tip-Grafted with Silver Nanoparticles for Photoelectrochemical Applications. *Nanoscale* **2013**, *5* (16), 7552. https://doi.org/10.1039/c3nr01459b.

(41) Amin, G.; Asif, M. H.; Zainelabdin, A.; Zaman, S.; Nur, O.; Willander, M. Influence of PH, Precursor Concentration, Growth Time, and Temperature on the Morphology of ZnO Nanostructures Grown by the Hydrothermal Method. *Journal of Nanomaterials* **2011**, *2011*, 1–9. https://doi.org/10.1155/2011/269692.

(42) Chang, C.-J.; Hung, S.-T.; Lin, C.-K.; Chen, C.-Y.; Kuo, E.-H. Selective Growth of ZnO Nanorods for Gas Sensors Using Ink-Jet Printing and Hydrothermal Processes. *Thin Solid Films* **2010**, *519* (5), 1693–1698. https://doi.org/10.1016/j.tsf.2010.08.153.

(43) Lim, H.-J.; Lee, D. Y.; Oh, Y.-J. Gas Sensing Properties of ZnO Thin Films Prepared by Microcontact Printing. *Sensors and Actuators A: Physical* **2006**, *125* (2), 405–410. https://doi.org/10.1016/j.sna.2005.08.031.

(44) Ma, T.; Wang, Y.; Tang, R.; Yu, H.; Jiang, H. Pre-Patterned ZnO Nanoribbons on Soft Substrates for Stretchable Energy Harvesting Applications. *Journal of Applied Physics* **2013**, *113* (20), 204503. https://doi.org/10.1063/1.4807320.

(45) Kang, H. W.; Yeo, J.; Hwang, J. O.; Hong, S.; Lee, P.; Han, S. Y.; Lee, J. H.; Rho, Y. S.; Kim, S. O.; Ko, S. H.; et al. Simple ZnO Nanowires Patterned Growth by Microcontact Printing for High Performance Field Emission Device. *The Journal of Physical Chemistry C* **2011**, *115* (23), 11435–11441. https://doi.org/10.1021/jp2019044.

(46) Boercker, J. E.; Schmidt, J. B.; Aydil, E. S. Transport Limited Growth of Zinc Oxide Nanowires. *Crystal Growth & Design* **2009**, *9* (6), 2783–2789. https://doi.org/10.1021/cg900021u.

(47) Viswanatha, R.; Santra, P. K.; Dasgupta, C.; Sarma, D. D. Growth Mechanism of Nanocrystals in Solution: ZnO, a Case Study. *Physical Review Letters* **2007**, *98* (25). https://doi.org/10.1103/PhysRevLett.98.255501.

(48) Choi, C.-H.; Chang, C. Aqueous Synthesis of Tailored ZnO Nanocrystals, Nanocrystal Assemblies, and Nanostructured Films by Physical Means Enabled by a Continuous Flow Microreactor. *Crystal Growth & Design* **2014**, *14* (9), 4759–4767. https://doi.org/10.1021/cg500911w.

(49) Ramprasad, S.; Su, Y.-W.; Chang, C.; Paul, B. K.; Palo, D. R. Cadmium Sulfide Thin Film Deposition: A Parametric Study Using Microreactor-Assisted

Chemical Solution Deposition. *Solar Energy Materials and Solar Cells* **2012**, *96*, 77–85. https://doi.org/10.1016/j.solmat.2011.09.015.

(50) Chang, C.-H.; Paul, B. K.; Remcho, V. T.; Atre, S.; Hutchison, J. E. Synthesis and Post-Processing of Nanomaterials Using Microreaction Technology. *Journal of Nanoparticle Research* **2008**, *10* (6), 965–980. https://doi.org/10.1007/s11051-007-9355-y.

(51) Han, S.-Y.; Chang, Y.-J.; Lee, D.-H.; Ryu, S.-O.; Lee, T.-J.; Chang, C.-H. Chemical Nanoparticle Deposition of Transparent ZnO Thin Films. *Electrochemical and Solid-State Letters* **2007**, *10* (1), K1. https://doi.org/10.1149/1.2372228.

(52) Qin, D.; Xia, Y.; Whitesides, G. M. Soft Lithography for Micro- and Nanoscale Patterning. *Nature Protocols* **2010**, *5* (3), 491–502. https://doi.org/10.1038/nprot.2009.234.

(53) Zhang, C. High-Quality Oriented ZnO Films Grown by Sol–Gel Process Assisted with ZnO Seed Layer. *Journal of Physics and Chemistry of Solids* **2010**, *71* (3), 364–369. https://doi.org/10.1016/j.jpcs.2010.01.001.

(54) Ji, L.-W.; Peng, S.-M.; Wu, J.-S.; Shih, W.-S.; Wu, C.-Z.; Tang, I.-T. Effect of Seed Layer on the Growth of Well-Aligned ZnO Nanowires. *Journal of Physics and Chemistry of Solids* **2009**, *70* (10), 1359–1362. https://doi.org/10.1016/j.jpcs.2009.07.029.

(55) Guillemin, S.; Consonni, V.; Appert, E.; Puyoo, E.; Rapenne, L.; Roussel, H. Critical Nucleation Effects on the Structural Relationship Between ZnO Seed Layer and Nanowires. *The Journal of Physical Chemistry C* **2012**, *116* (47), 25106–25111. https://doi.org/10.1021/jp308643w.

(56) Bowen, B. D.; Levine, S.; Epstein, N. Fine Particle Deposition in Laminar Flow through Parallel-Plate and Cylindrical Channels. *Journal of colloid and Interface science* **1976**, *54* (3), 375–390.

(57) Gervais, T.; Jensen, K. F. Mass Transport and Surface Reactions in Microfluidic Systems. *Chemical Engineering Science* **2006**, *61* (4), 1102–1121. https://doi.org/10.1016/j.ces.2005.06.024.

(58) Azam, A.; Babkair, S. Low-Temperature Growth of Well-Aligned Zinc Oxide Nanorod Arrays on Silicon Substrate and Their Photocatalytic Application. *International Journal of Nanomedicine* **2014**, 2109. https://doi.org/10.2147/IJN.S60839.

(59) Uekawa, N.; Yamashita, R.; Jun Wu, Y.; Kakegawa, K. Effect of Alkali Metal Hydroxide on Formation Processes of Zinc Oxide Crystallites from Aqueous Solutions Containing Zn(OH)42? Ions. *Physical Chemistry Chemical Physics* **2004**, *6* (2), 442. https://doi.org/10.1039/b310306d.

(60) Guo, M.; Diao, P.; Cai, S. Hydrothermal Growth of Well-Aligned ZnO Nanorod Arrays: Dependence of Morphology and Alignment Ordering upon Preparing Conditions. *Journal of Solid State Chemistry* **2005**, *178* (6), 1864–1873. https://doi.org/10.1016/j.jssc.2005.03.031.

(61) Ma, S.; Li, R.; Lv, C.; Xu, W.; Gou, X. Facile Synthesis of ZnO Nanorod Arrays and Hierarchical Nanostructures for Photocatalysis and Gas Sensor

Applications. *Journal of Hazardous Materials* **2011**, *192* (2), 730–740. https://doi.org/10.1016/j.jhazmat.2011.05.082.
(62) Shamhari, N. M.; Wee, B. S.; Chin, S. F.; Kok, K. Y. Synthesis and Characterization of Zinc Oxide Nanoparticles with Small Particle Size Distribution. *Acta Chimica Slovenica* **2018**, *65* (3), 578–585. https://doi.org/10.17344/acsi.2018.4213.
(63) Farhat, O. F.; Halim, M. M.; Abdullah, M. J.; Ali, M. K. M.; Allam, N. K. Morphological and Structural Characterization of Single-Crystal ZnO Nanorod Arrays on Flexible and Non-Flexible Substrates. *Beilstein Journal of Nanotechnology* **2015**, *6*, 720–725. https://doi.org/10.3762/bjnano.6.73.
(64) Duraisamy, N.; Muhammad, N. M.; Kim, H.-C.; Jo, J.-D.; Choi, K.-H. Fabrication of TiO2 Thin Film Memristor Device Using Electrohydrodynamic Inkjet Printing. *Thin Solid Films* **2012**, *520* (15), 5070–5074. https://doi.org/10.1016/j.tsf.2012.03.003.
(65) Kim, H.; Park, J.-H.; Suh, M.; Real Ahn, J.; Ju, S. Horizontally Aligned ZnO Nanowire Transistors Using Patterned Graphene Thin Films. *Applied Physics Letters* **2012**, *100* (6), 063112. https://doi.org/10.1063/1.3684614.
(66) Chen, P.-C.; Wan, L.-S.; Ke, B.-B.; Xu, Z.-K. Honeycomb-Patterned Film Segregated with Phenylboronic Acid for Glucose Sensing. *Langmuir* **2011**, *27* (20), 12597–12605. https://doi.org/10.1021/la201911f.
(67) Lin, P.; Yan, F. Organic Thin-Film Transistors for Chemical and Biological Sensing. *Advanced Materials* **2012**, *24* (1), 34–51. https://doi.org/10.1002/adma.201103334.
(68) Madaria, A. R.; Kumar, A.; Ishikawa, F. N.; Zhou, C. Uniform, Highly Conductive, and Patterned Transparent Films of a Percolating Silver Nanowire Network on Rigid and Flexible Substrates Using a Dry Transfer Technique. *Nano Research* **2010**, *3* (8), 564–573. https://doi.org/10.1007/s12274-010-0017-5.
(69) Kim, S.-R.; Triambulo, R. E.; Kim, J.-H.; Park, J.; Jeong, U.; Park, J.-W. Application of Patterned Ag-Nanowire Networks to Transparent Thin-Film Heaters and Electrodes for Organic Light-Emitting Diodes. *Japanese Journal of Applied Physics* **2016**, *55* (6S3), 06JB03. https://doi.org/10.7567/JJAP.55.06JB03.
(70) Lim, S.; Son, D.; Kim, J.; Lee, Y. B.; Song, J.-K.; Choi, S.; Lee, D. J.; Kim, J. H.; Lee, M.; Hyeon, T.; et al. Transparent and Stretchable Interactive Human Machine Interface Based on Patterned Graphene Heterostructures. *Advanced Functional Materials* **2015**, *25* (3), 375–383. https://doi.org/10.1002/adfm.201402987.
(71) Lee, J.; Kim, S.; Lee, J.; Yang, D.; Park, B. C.; Ryu, S.; Park, I. A Stretchable Strain Sensor Based on a Metal Nanoparticle Thin Film for Human Motion Detection. *Nanoscale* **2014**, *6* (20), 11932–11939. https://doi.org/10.1039/C4NR03295K.
(72) Park, S.-J.; Kim, J.; Chu, M.; Khine, M. Highly Flexible Wrinkled Carbon Nanotube Thin Film Strain Sensor to Monitor Human Movement. *Advanced*

Materials Technologies **2016**, *1* (5), 1600053. https://doi.org/10.1002/admt.201600053.

(73) Mahapatra, P. S.; Ghosh, A.; Ganguly, R.; Megaridis, C. M. Key Design and Operating Parameters for Enhancing Dropwise Condensation through Wettability Patterning. *International Journal of Heat and Mass Transfer* **2016**, *92*, 877–883. https://doi.org/10.1016/j.ijheatmasstransfer.2015.08.106.

(74) Takamatsu, S.; Lonjaret, T.; Ismailova, E.; Masuda, A.; Itoh, T.; Malliaras, G. G. Wearable Keyboard Using Conducting Polymer Electrodes on Textiles. *Advanced Materials* **2016**, *28* (22), 4485–4488. https://doi.org/10.1002/adma.201504249.

(75) Seung, W.; Gupta, M. K.; Lee, K. Y.; Shin, K.-S.; Lee, J.-H.; Kim, T. Y.; Kim, S.; Lin, J.; Kim, J. H.; Kim, S.-W. Nanopatterned Textile-Based Wearable Triboelectric Nanogenerator. *ACS Nano* **2015**, *9* (4), 3501–3509. https://doi.org/10.1021/nn507221f.

(76) Saito, A.; Miyamura, Y.; Nakajima, M.; Ishikawa, Y.; Sogo, K.; Kuwahara, Y.; Hirai, Y. Reproduction of the Morpho Blue by Nanocasting Lithography. *Journal of Vacuum Science & Technology B: Microelectronics and Nanometer Structures* **2006**, *24* (6), 3248. https://doi.org/10.1116/1.2395950.

(77) Wilson, M. E.; Kota, N.; Kim, Y.; Wang, Y.; Stolz, D. B.; LeDuc, P. R.; Ozdoganlar, O. B. Fabrication of Circular Microfluidic Channels by Combining Mechanical Micromilling and Soft Lithography. *Lab on a Chip* **2011**, *11* (8), 1550. https://doi.org/10.1039/c0lc00561d.

(78) Dai, S.; Wang, Y.; Zhang, D.; Han, X.; Shi, Q.; Wang, S.; Du, Z. Fabrication of Surface-Patterned ZnO Thin Films Using Sol–Gel Methods and Nanoimprint Lithography. *Journal of Sol-Gel Science and Technology* **2011**, *60* (1), 17–22. https://doi.org/10.1007/s10971-011-2545-1.

(79) Cao, L.; Yang, S.; Gao, W.; Liu, Z.; Gong, Y.; Ma, L.; Shi, G.; Lei, S.; Zhang, Y.; Zhang, S.; et al. Direct Laser-Patterned Micro-Supercapacitors from Paintable MoS_2 Films. *Small* **2013**, *9* (17), 2905–2910. https://doi.org/10.1002/smll.201203164.

(80) Laurenti, M.; Verna, A.; Fontana, M.; Quaglio, M.; Porro, S. Selective Growth of ZnO Nanowires on Substrates Patterned by Photolithography and Inkjet Printing. *Applied Physics A* **2014**, *117* (2), 901–907. https://doi.org/10.1007/s00339-014-8453-9.

(81) Park, C. W.; Moon, Y. G.; Seong, H.; Jung, S. W.; Oh, J.-Y.; Na, B. S.; Park, N.-M.; Lee, S. S.; Im, S. G.; Koo, J. B. Photolithography-Based Patterning of Liquid Metal Interconnects for Monolithically Integrated Stretchable Circuits. *ACS Applied Materials & Interfaces* **2016**, *8* (24), 15459–15465. https://doi.org/10.1021/acsami.6b01896.

(82) Sumaru, K.; Takagi, T.; Morishita, K.; Satoh, T.; Kanamori, T. Fabrication of Pocket-like Hydrogel Microstructures through Photolithography. *Soft Matter* **2018**, *14* (28), 5710–5714. https://doi.org/10.1039/C8SM00865E.

(83) Watanabe, K.; Hoshino, T.; Kanda, K.; Haruyama, Y.; Matsui, S. Brilliant Blue Observation from a *Morpho* -Butterfly-Scale Quasi-Structure. *Japanese*

Journal of Applied Physics **2005**, *44* (1), L48–L50. https://doi.org/10.1143/JJAP.44.L48.

(84) Zyla, G.; Kovalev, A.; Grafen, M.; Gurevich, E. L.; Esen, C.; Ostendorf, A.; Gorb, S. Generation of Bioinspired Structural Colors via Two-Photon Polymerization. *Scientific Reports* **2017**, *7* (1). https://doi.org/10.1038/s41598-017-17914-w.

(85) Hong, S.; Yeo, J.; Manorotkul, W.; Kang, H. W.; Lee, J.; Han, S.; Rho, Y.; Suh, Y. D.; Sung, H. J.; Ko, S. H. Digital Selective Growth of a ZnO Nanowire Array by Large Scale Laser Decomposition of Zinc Acetate. *Nanoscale* **2013**, *5* (9), 3698. https://doi.org/10.1039/c3nr34346d.

(86) Ouerfelli, J.; Regragui, M.; Morsli, M.; Djeteli, G.; Jondo, K.; Amory, C.; Tchangbedji, G.; Napo, K.; Bernède, J. C. Properties of ZnO Thin Films Deposited by Chemical Bath Deposition and Post Annealed. *Journal of Physics D: Applied Physics* **2006**, *39* (9), 1954–1959. https://doi.org/10.1088/0022-3727/39/9/035.

(87) Lee, B.-H.; Song, W.-C.; Manna, B.; Yang, H.-J.; Kim, J.-H.; Kim, Y.-S. Removal of Color from Wastewater Using Various Ozonation Techniques. In *2007 International Forum on Strategic Technology*; IEEE: Mongolia, 2007; pp 120–124. https://doi.org/10.1109/IFOST.2007.4798536.

(88) Jiang, Y.; Sun, Y.; Liu, H.; Zhu, F.; Yin, H. Solar Photocatalytic Decolorization of C.I. Basic Blue 41 in an Aqueous Suspension of TiO2–ZnO. *Dyes and Pigments* **2008**, *78* (1), 77–83. https://doi.org/10.1016/j.dyepig.2007.10.009.

(89) Wang, L.; Zheng, Y.; Li, X.; Dong, W.; Tang, W.; Chen, B.; Li, C.; Li, X.; Zhang, T.; Xu, W. Nanostructured Porous ZnO Film with Enhanced Photocatalytic Activity. *Thin Solid Films* **2011**, *519* (16), 5673–5678. https://doi.org/10.1016/j.tsf.2011.02.070.

(90) Kim, K.-J.; Kreider, P. B.; Choi, C.; Chang, C.-H.; Ahn, H.-G. Visible-Light-Sensitive Na-Doped p-Type Flower-like ZnO Photocatalysts Synthesized via a Continuous Flow Microreactor. *RSC Advances* **2013**, *3* (31), 12702. https://doi.org/10.1039/c3ra41866a.

(91) Raza, W.; Faisal, S. M.; Owais, M.; Bahnemann, D.; Muneer, M. Facile Fabrication of Highly Efficient Modified ZnO Photocatalyst with Enhanced Photocatalytic, Antibacterial and Anticancer Activity. *RSC Advances* **2016**, *6* (82), 78335–78350. https://doi.org/10.1039/C6RA06774C.

(92) Daneshvar, N.; Salari, D.; Khataee, A. R. Photocatalytic Degradation of Azo Dye Acid Red 14 in Water on ZnO as an Alternative Catalyst to TiO2. *Journal of Photochemistry and Photobiology A: Chemistry* **2004**, *162* (2–3), 317–322. https://doi.org/10.1016/S1010-6030(03)00378-2.

(93) Samadi, M.; Zirak, M.; Naseri, A.; Khorashadizade, E.; Moshfegh, A. Z. Recent Progress on Doped ZnO Nanostructures for Visible-Light Photocatalysis. *Thin Solid Films* **2016**, *605*, 2–19. https://doi.org/10.1016/j.tsf.2015.12.064.

(94) Chakrabarti, S.; Dutta, B. Photocatalytic Degradation of Model Textile Dyes in Wastewater Using ZnO as Semiconductor Catalyst. *Journal of Hazardous*

Materials **2004**, *112* (3), 269–278. https://doi.org/10.1016/j.jhazmat.2004.05.013.

(95) Özgür, Ü.; Alivov, Ya. I.; Liu, C.; Teke, A.; Reshchikov, M. A.; Doğan, S.; Avrutin, V.; Cho, S.-J.; Morkoç, H. A Comprehensive Review of ZnO Materials and Devices. *Journal of Applied Physics* **2005**, *98* (4), 041301. https://doi.org/10.1063/1.1992666.

(96) Yu, W.; Zhang, J.; Peng, T. New Insight into the Enhanced Photocatalytic Activity of N-, C- and S-Doped ZnO Photocatalysts. *Applied Catalysis B: Environmental* **2016**, *181*, 220–227. https://doi.org/10.1016/j.apcatb.2015.07.031.

(97) Zhang, D.; Zeng, F. Visible Light-Activated Cadmium-Doped ZnO Nanostructured Photocatalyst for the Treatment of Methylene Blue Dye. *Journal of Materials Science* **2012**, *47* (5), 2155–2161. https://doi.org/10.1007/s10853-011-6016-4.

(98) Wu, C.; Shen, L.; Yu, H.; Zhang, Y.-C.; Huang, Q. Solvothermal Synthesis of Cu-Doped ZnO Nanowires with Visible Light-Driven Photocatalytic Activity. *Materials Letters* **2012**, *74*, 236–238. https://doi.org/10.1016/j.matlet.2012.01.125.

(99) Sun, J.-H.; Dong, S.-Y.; Feng, J.-L.; Yin, X.-J.; Zhao, X.-C. Enhanced Sunlight Photocatalytic Performance of Sn-Doped ZnO for Methylene Blue Degradation. *Journal of Molecular Catalysis A: Chemical* **2011**, *335* (1–2), 145–150. https://doi.org/10.1016/j.molcata.2010.11.026.

(100) Cun, W.; Jincai, Z.; Xinming, W.; Bixian, M.; Guoying, S.; Ping’an, P.; Jiamo, F. Preparation, Characterization and Photocatalytic Activity of Nano-Sized ZnO/SnO2 Coupled Photocatalysts. *Applied Catalysis B: Environmental* **2002**, *39* (3), 269–279. https://doi.org/10.1016/S0926-3373(02)00115-7.

(101) Ahmad, M.; Ahmed, E.; Zhang, Y.; Khalid, N. R.; Xu, J.; Ullah, M.; Hong, Z. Preparation of Highly Efficient Al-Doped ZnO Photocatalyst by Combustion Synthesis. *Current Applied Physics* **2013**, *13* (4), 697–704. https://doi.org/10.1016/j.cap.2012.11.008.

(102) Saleh, R.; Djaja, N. F. UV Light Photocatalytic Degradation of Organic Dyes with Fe-Doped ZnO Nanoparticles. *Superlattices and Microstructures* **2014**, *74*, 217–233. https://doi.org/10.1016/j.spmi.2014.06.013.

(103) Mohan, R.; Krishnamoorthy, K.; Kim, S.-J. Enhanced Photocatalytic Activity of Cu-Doped ZnO Nanorods. *Solid State Communications* **2012**, *152* (5), 375–380. https://doi.org/10.1016/j.ssc.2011.12.008.

(104) Ba-Abbad, M. M.; Kadhum, A. A. H.; Mohamad, A. B.; Takriff, M. S.; Sopian, K. Visible Light Photocatalytic Activity of Fe3+-Doped ZnO Nanoparticle Prepared via Sol–Gel Technique. *Chemosphere* **2013**, *91* (11), 1604–1611. https://doi.org/10.1016/j.chemosphere.2012.12.055.

(105) Karunakaran, C.; Vijayabalan, A.; Manikandan, G. Photocatalytic and Bactericidal Activities of Hydrothermally Synthesized Nanocrystalline Cd-Doped ZnO. *Superlattices and Microstructures* **2012**, *51* (3), 443–453. https://doi.org/10.1016/j.spmi.2012.01.008.

(106) Chen, L.-C.; Tu, Y.-J.; Wang, Y.-S.; Kan, R.-S.; Huang, C.-M. Characterization and Photoreactivity of N-, S-, and C-Doped ZnO under UV and Visible Light Illumination. *Journal of Photochemistry and Photobiology A: Chemistry* **2008**, *199* (2–3), 170–178. https://doi.org/10.1016/j.jphotochem.2008.05.022.

(107) Sudrajat, H.; Hartuti, S. Easily Separable N-Doped ZnO Microspheres with High Photocatalytic Activity under Visible Light. *Materials Research Bulletin* **2018**, *102*, 319–323. https://doi.org/10.1016/j.materresbull.2018.02.048.

(108) Zhou, X.; Li, Y.; Peng, T.; Xie, W.; Zhao, X. Synthesis, Characterization and Its Visible-Light-Induced Photocatalytic Property of Carbon Doped ZnO. *Materials Letters* **2009**, *63* (20), 1747–1749. https://doi.org/10.1016/j.matlet.2009.05.018.

(109) Balachandran, S.; Swaminathan, M. Facile Fabrication of Heterostructured Bi $_2$ O $_3$ –ZnO Photocatalyst and Its Enhanced Photocatalytic Activity. *The Journal of Physical Chemistry C* **2012**, *116* (50), 26306–26312. https://doi.org/10.1021/jp306874z.

(110) Vaiano, V.; Matarangolo, M.; Murcia, J. J.; Rojas, H.; Navío, J. A.; Hidalgo, M. C. Enhanced Photocatalytic Removal of Phenol from Aqueous Solutions Using ZnO Modified with Ag. *Applied Catalysis B: Environmental* **2018**, *225*, 197–206. https://doi.org/10.1016/j.apcatb.2017.11.075.

(111) Hong, E.; Kim, J. H. Oxide Content Optimized ZnS–ZnO Heterostructures via Facile Thermal Treatment Process for Enhanced Photocatalytic Hydrogen Production. *International Journal of Hydrogen Energy* **2014**, *39* (19), 9985–9993. https://doi.org/10.1016/j.ijhydene.2014.04.137.

(112) Yuan, Y.-J.; Wang, F.; Hu, B.; Lu, H.-W.; Yu, Z.-T.; Zou, Z.-G. Significant Enhancement in Photocatalytic Hydrogen Evolution from Water Using a MoS $_2$ Nanosheet-Coated ZnO Heterostructure Photocatalyst. *Dalton Transactions* **2015**, *44* (24), 10997–11003. https://doi.org/10.1039/C5DT00906E.

(113) Ren, C.; Yang, B.; Wu, M.; Xu, J.; Fu, Z.; lv, Y.; Guo, T.; Zhao, Y.; Zhu, C. Synthesis of Ag/ZnO Nanorods Array with Enhanced Photocatalytic Performance. *Journal of Hazardous Materials* **2010**, *182* (1–3), 123–129. https://doi.org/10.1016/j.jhazmat.2010.05.141.

(114) Liu, H.; Hu, Y.; Zhang, Z.; Liu, X.; Jia, H.; Xu, B. Synthesis of Spherical Ag/ZnO Heterostructural Composites with Excellent Photocatalytic Activity under Visible Light and UV Irradiation. *Applied Surface Science* **2015**, *355*, 644–652. https://doi.org/10.1016/j.apsusc.2015.07.012.

(115) Saoud, K.; Alsoubaihi, R.; Bensalah, N.; Bora, T.; Bertino, M.; Dutta, J. Synthesis of Supported Silver Nano-Spheres on Zinc Oxide Nanorods for Visible Light Photocatalytic Applications. *Materials Research Bulletin* **2015**, *63*, 134–140. https://doi.org/10.1016/j.materresbull.2014.12.001.

(116) R., R.; K.S., S.; K.G., G. ZnO:Ag Nanorods as Efficient Photocatalysts: Sunlight Driven Photocatalytic Degradation of Sulforhodamine B. *Applied Surface Science* **2018**, *427*, 863–875. https://doi.org/10.1016/j.apsusc.2017.09.050.

(117) Sobana, N.; Swaminathan, M. The Effect of Operational Parameters on the Photocatalytic Degradation of Acid Red 18 by ZnO. *Separation and*

Purification Technology **2007**, *56* (1), 101–107. https://doi.org/10.1016/j.seppur.2007.01.032.

(118) Bechambi, O.; Sayadi, S.; Najjar, W. Photocatalytic Degradation of Bisphenol A in the Presence of C-Doped ZnO: Effect of Operational Parameters and Photodegradation Mechanism. *Journal of Industrial and Engineering Chemistry* **2015**, *32*, 201–210. https://doi.org/10.1016/j.jiec.2015.08.017.

(119) Modirshahla, N.; Hassani, A.; Behnajady, M. A.; Rahbarfam, R. Effect of Operational Parameters on Decolorization of Acid Yellow 23 from Wastewater by UV Irradiation Using ZnO and ZnO/SnO2 Photocatalysts. *Desalination* **2011**, *271* (1–3), 187–192. https://doi.org/10.1016/j.desal.2010.12.027.

(120) Vernardou, D.; Kenanakis, G.; Couris, S.; Koudoumas, E.; Kymakis, E.; Katsarakis, N. PH Effect on the Morphology of ZnO Nanostructures Grown with Aqueous Chemical Growth. *Thin Solid Films* **2007**, *515* (24), 8764–8767. https://doi.org/10.1016/j.tsf.2007.03.108.

(121) Venu Gopal, V. R.; Kamila, S. Effect of Temperature on the Morphology of ZnO Nanoparticles: A Comparative Study. *Applied Nanoscience* **2017**, *7* (3–4), 75–82. https://doi.org/10.1007/s13204-017-0553-3.

(122) Zhao, X.; Li, M.; Lou, X. Sol–Gel Assisted Hydrothermal Synthesis of ZnO Microstructures: Morphology Control and Photocatalytic Activity. *Advanced Powder Technology* **2014**, *25* (1), 372–378. https://doi.org/10.1016/j.apt.2013.06.004.

(123) Jang, E. S.; Won, J.-H.; Hwang, S.-J.; Choy, J.-H. Fine Tuning of the Face Orientation of ZnO Crystals to Optimize Their Photocatalytic Activity. *Advanced Materials* **2006**, *18* (24), 3309–3312. https://doi.org/10.1002/adma.200601455.

(124) Becker, J.; Raghupathi, K. R.; St. Pierre, J.; Zhao, D.; Koodali, R. T. Tuning of the Crystallite and Particle Sizes of ZnO Nanocrystalline Materials in Solvothermal Synthesis and Their Photocatalytic Activity for Dye Degradation. *The Journal of Physical Chemistry C* **2011**, *115* (28), 13844–13850. https://doi.org/10.1021/jp2038653.

(125) Zhang, X.; Wang, Y.; Hou, F.; Li, H.; Yang, Y.; Zhang, X.; Yang, Y.; Wang, Y. Effects of Ag Loading on Structural and Photocatalytic Properties of Flower-like ZnO Microspheres. *Applied Surface Science* **2017**, *391*, 476–483. https://doi.org/10.1016/j.apsusc.2016.06.109.

(126) He, Z.; Li, Y.; Zhang, Q.; Wang, H. Capillary Microchannel-Based Microreactors with Highly Durable ZnO/TiO2 Nanorod Arrays for Rapid, High Efficiency and Continuous-Flow Photocatalysis. *Applied Catalysis B: Environmental* **2010**, *93* (3–4), 376–382. https://doi.org/10.1016/j.apcatb.2009.10.011.

(127) Zhang, Q.; Zhang, Q.; Wang, H.; Li, Y. A High Efficiency Microreactor with Pt/ZnO Nanorod Arrays on the Inner Wall for Photodegradation of Phenol. *Journal of Hazardous Materials* **2013**, *254–255*, 318–324. https://doi.org/10.1016/j.jhazmat.2013.04.012.

(128) Han, Z.; Li, J.; He, W.; Li, S.; Li, Z.; Chu, J.; Chen, Y. A Microfluidic Device with Integrated ZnO Nanowires for Photodegradation Studies of Methylene

Blue under Different Conditions. *Microelectronic Engineering* **2013**, *111*, 199–203. https://doi.org/10.1016/j.mee.2013.03.154.

(129) Behnajady, M. A.; Modirshahla, N.; Daneshvar, N.; Rabbani, M. Photocatalytic Degradation of an Azo Dye in a Tubular Continuous-Flow Photoreactor with Immobilized TiO2 on Glass Plates. *Chemical Engineering Journal* **2007**, *127* (1–3), 167–176. https://doi.org/10.1016/j.cej.2006.09.013.

(130) Ramgir, N. S.; Ganapathi, S. K.; Kaur, M.; Datta, N.; Muthe, K. P.; Aswal, D. K.; Gupta, S. K.; Yakhmi, J. V. Sub-Ppm H2S Sensing at Room Temperature Using CuO Thin Films. *Sensors and Actuators B: Chemical* **2010**, *151* (1), 90–96. https://doi.org/10.1016/j.snb.2010.09.043.

(131) Tamaki, J.; Shimanoe, K.; Yamada, Y.; Yamamoto, Y.; Miura, N.; Yamazoe, N. Dilute Hydrogen Sulfide Sensing Properties of CuO–SnO2 Thin Film Prepared by Low-Pressure Evaporation Method. *Sensors and Actuators B: Chemical* **1998**, *49* (1–2), 121–125. https://doi.org/10.1016/S0925-4005(98)00144-0.

(132) Mridha, S.; Basak, D. Investigation of a P-CuO/n-ZnO Thin Film Heterojunction for H $_2$ Gas-Sensor Applications. *Semiconductor Science and Technology* **2006**, *21* (7), 928–932. https://doi.org/10.1088/0268-1242/21/7/017.

(133) Hoa, N. D.; An, S. Y.; Dung, N. Q.; Van Quy, N.; Kim, D. Synthesis of P-Type Semiconducting Cupric Oxide Thin Films and Their Application to Hydrogen Detection. *Sensors and Actuators B: Chemical* **2010**, *146* (1), 239–244. https://doi.org/10.1016/j.snb.2010.02.045.

(134) Aslani, A.; Oroojpour, V. CO Gas Sensing of CuO Nanostructures, Synthesized by an Assisted Solvothermal Wet Chemical Route. *Physica B: Condensed Matter* **2011**, *406* (2), 144–149. https://doi.org/10.1016/j.physb.2010.09.038.

(135) Parmar, M.; Bhatia, R.; Prasad, V.; Rajanna, K. Ethanol Sensing Using CuO/MWNT Thin Film. *Sensors and Actuators B: Chemical* **2011**, *158* (1), 229–234. https://doi.org/10.1016/j.snb.2011.06.010.

(136) Liao, L.; Zhang, Z.; Yan, B.; Zheng, Z.; Bao, Q. L.; Wu, T.; Li, C. M.; Shen, Z. X.; Zhang, J. X.; Gong, H.; et al. Multifunctional CuO Nanowire Devices: P-Type Field Effect Transistors and CO Gas Sensors. *Nanotechnology* **2009**, *20* (8), 085203. https://doi.org/10.1088/0957-4484/20/8/085203.

(137) Wang, B.; Wu, X.-L.; Shu, C.-Y.; Guo, Y.-G.; Wang, C.-R. Synthesis of CuO/Graphene Nanocomposite as a High-Performance Anode Material for Lithium-Ion Batteries. *Journal of Materials Chemistry* **2010**, *20* (47), 10661. https://doi.org/10.1039/c0jm01941k.

(138) Gao, S.; Yang, S.; Shu, J.; Zhang, S.; Li, Z.; Jiang, K. Green Fabrication of Hierarchical CuO Hollow Micro/Nanostructures and Enhanced Performance as Electrode Materials for Lithium-Ion Batteries. *The Journal of Physical Chemistry C* **2008**, *112* (49), 19324–19328. https://doi.org/10.1021/jp808545r.

(139) Ko, S.; Lee, J.-I.; Yang, H. S.; Park, S.; Jeong, U. Mesoporous CuO Particles Threaded with CNTs for High-Performance Lithium-Ion Battery Anodes. *Advanced Materials* **2012**, *24* (32), 4451–4456. https://doi.org/10.1002/adma.201201821.

(140) Zhang, Q.; Zhang, K.; Xu, D.; Yang, G.; Huang, H.; Nie, F.; Liu, C.; Yang, S. CuO Nanostructures: Synthesis, Characterization, Growth Mechanisms, Fundamental Properties, and Applications. *Progress in Materials Science* **2014**, *60*, 208–337. https://doi.org/10.1016/j.pmatsci.2013.09.003.

(141) Enright, R.; Miljkovic, N.; Al-Obeidi, A.; Thompson, C. V.; Wang, E. N. Condensation on Superhydrophobic Surfaces: The Role of Local Energy Barriers and Structure Length Scale. *Langmuir* **2012**, *28* (40), 14424–14432. https://doi.org/10.1021/la302599n.

(142) Sanal, K. C.; Vikas, L. S.; Jayaraj, M. K. Room Temperature Deposited Transparent P-Channel CuO Thin Film Transistors. *Applied Surface Science* **2014**, *297*, 153–157. https://doi.org/10.1016/j.apsusc.2014.01.109.

(143) Dolai, S.; Dey, R.; Das, S.; Hussain, S.; Bhar, R.; Pal, A. K. Cupric Oxide (CuO) Thin Films Prepared by Reactive d.c. Magnetron Sputtering Technique for Photovoltaic Application. *Journal of Alloys and Compounds* **2017**, *724*, 456–464. https://doi.org/10.1016/j.jallcom.2017.07.061.

(144) Vaseem, M.; Umar, A.; Hahn, Y. B.; Kim, D. H.; Lee, K. S.; Jang, J. S.; Lee, J. S. Flower-Shaped CuO Nanostructures: Structural, Photocatalytic and XANES Studies. *Catalysis Communications* **2008**, *10* (1), 11–16. https://doi.org/10.1016/j.catcom.2008.07.022.

(145) Poizot, P.; Hung, C.-J.; Nikiforov, M. P.; Bohannan, E. W.; Switzer, J. A. An Electrochemical Method for CuO Thin Film Deposition from Aqueous Solution. *Electrochemical and Solid-State Letters* **2003**, *6* (2), C21. https://doi.org/10.1149/1.1535753.

(146) Medina-Valtierra, J.; Ramírez-Ortiz, J.; Arroyo-Rojas, V. M.; Ruiz, F. Cyclohexane Oxidation over Cu2O–CuO and CuO Thin Films Deposited by CVD Process on Fiberglass. *Applied Catalysis A: General* **2003**, *238* (1), 1–9. https://doi.org/10.1016/S0926-860X(02)00074-1.

(147) Jayatissa, A. H.; Guo, K.; Jayasuriya, A. C. Fabrication of Cuprous and Cupric Oxide Thin Films by Heat Treatment. *Applied Surface Science* **2009**, *255* (23), 9474–9479. https://doi.org/10.1016/j.apsusc.2009.07.072.

(148) Morales, J.; Sánchez, L.; Martín, F.; Ramos-Barrado, J. R.; Sánchez, M. Nanostructured CuO Thin Film Electrodes Prepared by Spray Pyrolysis: A Simple Method for Enhancing the Electrochemical Performance of CuO in Lithium Cells. *Electrochimica Acta* **2004**, *49* (26), 4589–4597. https://doi.org/10.1016/j.electacta.2004.05.012.

(149) Wang, Y.; Jiang, T.; Meng, D.; Wang, D.; Yu, M. Synthesis and Enhanced Photocatalytic Property of Feather-like Cd-Doped CuO Nanostructures by Hydrothermal Method. *Applied Surface Science* **2015**, *355*, 191–196. https://doi.org/10.1016/j.apsusc.2015.07.122.

(150) Singh, D. P.; Ojha, A. K.; Srivastava, O. N. Synthesis of Different Cu(OH) $_2$ and CuO (Nanowires, Rectangles, Seed-, Belt-, and Sheetlike) Nanostructures by Simple Wet Chemical Route. *The Journal of Physical Chemistry C* **2009**, *113* (9), 3409–3418. https://doi.org/10.1021/jp804832g.

(151) Liu, L.; Hong, K.; Hu, T.; Xu, M. Synthesis of Aligned Copper Oxide Nanorod Arrays by a Seed Mediated Hydrothermal Method. *Journal of Alloys and*

Compounds **2012**, *511* (1), 195–197. https://doi.org/10.1016/j.jallcom.2011.09.028.

(152) Vaseem, M.; Umar, A.; Kim, S. H.; Hahn, Y.-B. Low-Temperature Synthesis of Flower-Shaped CuO Nanostructures by Solution Process: Formation Mechanism and Structural Properties. *The Journal of Physical Chemistry C* **2008**, *112* (15), 5729–5735. https://doi.org/10.1021/jp710358j.

(153) Fterich, M.; Nasr, F. B.; Lefi, R.; Toumi, M.; Guermazi, S. Effect of Concentration of Hexamethylenetetramine in Structure, Microstructure and Optical Properties of CuO Nanoparticles Synthesized by Hydrothermal Route. *Materials Science in Semiconductor Processing* **2016**, *43*, 114–122. https://doi.org/10.1016/j.mssp.2015.11.023.

(154) Xu, M.; Wang, F.; Zhao, M.; Yang, S.; Sun, Z.; Song, X. Synthesis of Copper Oxide Nanostructures via a Composite-Hydroxide-Mediated Approach: Morphology Control and the Electrochemical Performances as Anode Material for Lithium Ion Batteries. *Physica E: Low-dimensional Systems and Nanostructures* **2011**, *44* (2), 506–510. https://doi.org/10.1016/j.physe.2011.09.030.

(155) De Los Santos Valladares, L.; Salinas, D. H.; Dominguez, A. B.; Najarro, D. A.; Khondaker, S. I.; Mitrelias, T.; Barnes, C. H. W.; Aguiar, J. A.; Majima, Y. Crystallization and Electrical Resistivity of Cu2O and CuO Obtained by Thermal Oxidation of Cu Thin Films on SiO2/Si Substrates. *Thin Solid Films* **2012**, *520* (20), 6368–6374. https://doi.org/10.1016/j.tsf.2012.06.043.

(156) Chang, F.-M.; Cheng, S.-L.; Hong, S.-J.; Sheng, Y.-J.; Tsao, H.-K. Superhydrophilicity to Superhydrophobicity Transition of CuO Nanowire Films. *Applied Physics Letters* **2010**, *96* (11), 114101. https://doi.org/10.1063/1.3360847.

(157) Noothongkaew, S.; Thumthan, O.; An, K.-S. UV-Photodetectors Based on CuO/ZnO Nanocomposites. *Materials Letters* **2018**, *233*, 318–323. https://doi.org/10.1016/j.matlet.2018.09.024.

(158) Wu, J.-K.; Chen, W.-J.; Chang, Y.; Chen, Y.; Hang, D.-R.; Liang, C.-T.; Lu, J.-Y. Fabrication and Photoresponse of ZnO Nanowires/CuO Coaxial Heterojunction. *Nanoscale Research Letters* **2013**, *8* (1), 387. https://doi.org/10.1186/1556-276X-8-387.

(159) Mardikar, S. P.; Kulkarni, S.; Adhyapak, P. V. Sunlight Driven Highly Efficient Degradation of Methylene Blue by CuO-ZnO Nanoflowers. *Journal of Environmental Chemical Engineering* **2018**. https://doi.org/10.1016/j.jece.2018.11.033.

(160) Harish, S.; Archana, J.; Sabarinathan, M.; Navaneethan, M.; Nisha, K. D.; Ponnusamy, S.; Muthamizhchelvan, C.; Ikeda, H.; Aswal, D. K.; Hayakawa, Y. Controlled Structural and Compositional Characteristic of Visible Light Active ZnO/CuO Photocatalyst for the Degradation of Organic Pollutant. *Applied Surface Science* **2017**, *418*, 103–112. https://doi.org/10.1016/j.apsusc.2016.12.082.

(161) Peshkova, T. V.; Dimitrov, D. Ts.; Nalimova, S. S.; Kononova, I. E.; Nikolaev, N. K.; Papazova, K. I.; Bozhinova, A. S.; Moshnikov, V. A.; Terukov, E. I.

Structures of Nanowires with Zn-ZnO:CuO Junctions for Detecting Ethanol Vapors. *Technical Physics* **2014**, *59* (5), 771–776. https://doi.org/10.1134/S1063784214050259.

(162) Hussain, S.; Cao, C.; Nabi, G.; Khan, W. S.; Tahir, M.; Tanveer, M.; Aslam, I. Optical and Electrical Characterization of ZnO/CuO Heterojunction Solar Cells. *Optik* **2017**, *130*, 372–377. https://doi.org/10.1016/j.ijleo.2016.10.099.

(163) Paul, S.; Sultana, J.; Karmakar, A.; Chattopadhyay, S. Effect of Prolonged Growth on the Chemical Bath Deposited ZnO Nanowires and Consequent Photovoltaic Performance of N-ZnO NWs/p-CuO Heterojunction Solar Cells. *Materials Today: Proceedings* **2017**, *4* (14), 12496–12499. https://doi.org/10.1016/j.matpr.2017.10.050.

(164) Lee, J.; Park, E.; Park, T.; Lee, J.; Sung, M.; Yi, W. Large Scale Synthesis and Enhanced Field Emission Properties from Hybrid CuO/ZnO Nanorod. *Journal of Nanoscience and Nanotechnology* **2011**, *11* (8), 7299–7302. https://doi.org/10.1166/jnn.2011.4788.

(165) Koshy, J.; George, K. C. Annealing Effects on Crystallite Size and Band Gap of CuO Nanoparticles. 8.

(166) Ghosh, A.; Show, B. B.; Ghosh, S.; Mukherjee, N.; Bhattacharya, G.; Datta, S. K.; Mondal, A. Electrochemical Synthesis of P-CuO Thin Films and Development of a p-CuO/n-ZnO Heterojunction and Its Application as a Selective Gas Sensor. *RSC Adv.* **2014**, *4* (93), 51569–51575. https://doi.org/10.1039/C4RA05360E.